PHYSIK - DEPARTMENT

2D-ACAR and Compton Scattering: Investigation of the Electronic Structure of Pd and LaB_6

Dissertation
von
Josef Helmut Ketels

November 2022

Technische Universität München

Technische Universität München
TUM School of Natural Sciences

2D-ACAR and Compton Scattering: Investigation of the Electronic Structure of Pd and LaB_6

Josef Helmut Ketels

Vollständiger Abdruck der von der TUM School of Natural Sciences der Technischen Universität München zur Erlangung eines

Doktors der Naturwissenschaften (Dr. rer. nat.)

genehmigte Dissertation.

Vorsitz: apl. Prof. Dr. Norbert Kaiser

Prüfer der Dissertation:

1. Prof. Dr. Christoph Pascal Hugenschmidt
2. apl. Prof. Dr. Martin Brandt

Diese Dissertation wurde am 07.12.2022 bei der Technischen Universität München eingereicht und durch die TUM School of Natural Sciences am 13.02.2023 angenommen.

Abstract

This thesis focuses on the investigation of the electronic structure of materials with two-dimensional angular correlation of electron positron annihilation radiation (2D-ACAR) and Compton scattering experiments. In particular, the electronic structure of palladium was investigated with both methods in order to reveal their specific features. The data obtained from both techniques was compared by the application of a new reconstruction algorithm, the so-called direct inversion method (DIM). For describing the Fermi surface (FS) the importance of positron wave function effects and positron-electron correlations in the theoretical modeling of the two-photon momentum density (TPMD) are emphasized. Furthermore, the specific strengths of the two techniques are highlighted, like the straight forward data treatment in ACAR or the well understood theoretical calculation of Compton profiles. The new DIM algorithm offers advantages over other algebraic reconstruction techniques especially in the reconstruction of Compton scattering data. For example, the application of Tikhonov-like regularization functionals allows the reconstruction of anisotropies. This simplifies the reconstruction process, as the anisotropies of the Compton profiles go much faster to zero for higher momenta than the Compton profiles themselves. Finally, modeling of the FS of the rare-earth hexaboride LaB_6 from experimental 2D-ACAR data, measured along three high symmetry directions, could excellently reproduce the features of the theoretically predicted FS obtained from first-principle calculations. Furthermore, the measurements on LaB_6 together with theoretical calculations on the same material and on CeB_6 suggest that both materials are topologically trivial but correlated systems.

Zusammenfassung

Diese Arbeit beschäftigt sich mit der Untersuchung der elektronischen Struktur von Kristallen mithilfe von zwei experimentellen Methoden. Die beiden verwendeten Techniken sind die Messung der Winkelkorrelation der Annihilationsstrahlung von Elektronen-Positronen-Paaren (ACAR) und die Messung der Comptonstreuung von Röntgenstrahlung. Im Speziellen wird die elektronische Struktur von Palladium untersucht. Dabei wird durch den Vergleich der Messergebnisse beider Experimente die Wichtigkeit von Positronen-Wellenfunktionseffekten und Positronen-Elektronen-Korrelationen in der theoretischen Modellierung der Zwei-Photonen-Impulsverteilung hervorgehoben. Die spezifischen Vorteile beider Techniken, wie z. B. die klare Datenanalyse in ACAR oder die vergleichsweise einfach theoretische Modellierung von Comptonprofilen wird klar herausgestellt. Um die Daten beider Experimenten vergleichen zu können, wird ein neuer Algorithmus zur Rekonstruktion von Elektronen-Impulsdichten in höheren Dimensionen vorgestellt. Im Vergleich zu anderen algebraischen Rekonstruktionsansätzen bietet die direkte Inversionsmethode (DIM) insbesondere bei der Anwendung auf Comptondaten Vorteile. Beispielsweise bietet die Verwendung von Tikhonovartigen Regularisierungsfunktionalen die Möglichkeit, positive und negative Dichten und damit Anisotropien zu rekonstruieren. Im Vergleich zu den Comptonprofilen selbst streben deren Anisotropien bei hohen Impulsen deutlich schneller gegen null. Außerdem wird die Fermifläche von LaB_6 aus drei experimentell gemessenen 2D-ACAR Spektren modelliert. Dabei wird eine sehr gute Übereinstimmung zwischen Eigenschaften der theoretisch berechneten Fermifläche und den experimentell gemessenen Daten erzielt. Abschließend kann aus der gemeinsamen Betrachtung von experimentellen Ergebnissen und theoretischen Dichtefunktionaltheorie (DFT) Rechnungen für LaB_6 und CeB_6 gefolgert werden, dass beide Materialien topologisch triviale, aber korrelierte Systeme sind.

Contents

Chapter 1

Introduction

"A metal [is defined] as a solid with a Fermi surface." [Mac63] this quote from A. R. Mackintosh is just one example illustrating the importance of the concept of the Fermi surface (FS) in condensed matter physics. Almost all properties of a solid are defined by its electronic structure. The experimental measurement of the electronic structure is of crucial importance, although its theoretical modeling has made huge progress during the last decades.

Angle resolved photoemission spectroscopy (ARPES) is one of the most widely used direct methods for determining the electronic structure, by measuring the angular distribution and kinetic energy of the photoelectrons emitted from the sample. In order to induce the photoelectric effect, the sample has to be illuminated with x-rays of an energy exceeding the work function of the material. Typical energies are in the range of 10 to 100 eV. In this energy range the inelastic mean-free path of the photoelectrons is short and therefore their escape depth is limited to a few angstrom. Thus, ARPES is a very surface sensitive technique and can only be used to study the bulk electronic in cases, where the surface electronic structure is similar to the bulk [Dam04].

A second, in particular in the bulk, very important approach for the measurement of the electronic structure are the quantum oscillatory techniques, e. g., exploiting the de-Haas-van-Alphen (dHvA) effect, which records the response of the material magnetization to strong magnetic excitation. Besides the required high external magnetic fields usually extremely low temperatures and crystals with very low disorder are required [Ons52].

The two experimental techniques used in this thesis, two-dimensional angular correlation of electron positron annihilation radiation (2D-ACAR) and Compton scattering, are bulk methods without putting strong limitations on the ambient conditions.

The Compton effect, first discovered by Arthur H. Compton in 1923 [Com23], describes the inelastical scattering of x-rays by electrons. By considering light as particles, this inelastical scattering process leads to a shift in the wavelength of the outgoing photons, which was deduced by applying conservation of energy and momentum in the two particle process of electron and photon. Compton's explanation of this effect was a very strong argument, that light can be described as a wave phenomenon and also by particles. Compton scattering is a scattering process in the deeply inelastic regime, in which the non-resonant scattering cross-section becomes proportional to the electron momentum density (EMD) and thus provides a powerful tool to investigate the many-body electron wave function. In metals, the FS leads to sharp changes of the electron occupancy in the EMD. Compton scattering is therefore a technique suitable to determine FSs. Furthermore it probes the bulk electronic structure, since high energy x-rays (usually $> 100\,\mathrm{keV}$) are used for the experiments, which penetrate deeply into the sample [Coo85].

Angular correlation of electron positron annihilation radiation (ACAR) is very closely related to Compton scattering. It is based on the conservation of energy and momentum in positron-electron-annihilation to measure the two-dimensional projection of the EMD. As soon as the two particles annihilate, predominately two photons with an energy of $511\,\mathrm{keV}$ are created. The positrons thermalize in the sample and therefore can be considered as stationary. If we consider such a thermalized positron annihilating with a non-moving electron the two photons would move exactly in opposite directions. Due to the electron momentum in the crystal potential, there is a deviation from anti-collinearity of the annihilation quanta. By measuring this deviation the two-photon momentum density (TPMD), which is closely connected to the EMD, can be obtained. One of the main disadvantages of ACAR is the high defect sensitivity of the positrons. For instance a vacancy in the crystal forms an attractive potential for positrons, leading to effective positron trapping, i. e. positrons trapped in defects no longer probe the undisturbed electronic structure. Therefore, only high-quality single crystals can be analysed by ACAR; Compton scattering is independent from defects present in the lattice.

In this thesis, Compton and 2D-ACAR measurements on palladium were performed in order to evaluate the influence of the positron probing effects (chapter 6). For the comparison of both experimental techniques, which deliver projections of the electronic structure in different dimensions, a new recon-

struction algorithm was developed (chapter 5). The second material studied in this work is LaB_6. In chapter 7, ACAR measurements on LaB_6 are compared to theoretical calculations on LaB_6 and CeB_6 in order to investigate the influence of the $4f$ electrons on the electronic structure of the light rare-earth hexaborides. As a foundation for the latter chapters, the chapters 2, 3 and 4 give an introduction in relevant condensed matter principles, physics with positrons and the experimental techniques, respectively.

Chapter 2

Basics of Electronic Structure in Crystals

This chapter will introduce basics of crystals which are necessary to finally explain the concept of the electronic structure in crystals. The chapter is mostly based on the text books by Ashcroft and Mermin [AM13] and Kittel [Kit96].

2.1 The Crystal Lattice

2.1.1 Real Space

Starting point for the definition of real space crystal lattices is the Bravais lattice, which is an infinitely extended periodic pattern of points. Mathematically this can be defined as the position of all points

$$\mathbf{R} = n_1\mathbf{a_1} + n_2\mathbf{a_2} + n_3\mathbf{a_3}, \tag{2.1}$$

where n_1, n_2 and n_3 are integers and $\mathbf{a_1}$, $\mathbf{a_2}$ and $\mathbf{a_3}$ are arbitrary vectors spanning the three dimensional space, the so-called lattice vectors.

The parallelepiped created by the lattice vectors is called the *unit cell*. In three dimensions, the number of Bravais lattices is limited to only fourteen. However, for a single Bravais lattice, there are many valid choices for the lattice vectors, which fill the space without overlapping unit cells. The unit cell with the smallest possible volume is called primitive cell. Even if there are several choices of primitive cells in a given crystal lattice, they all have the same volume and contain exactly one lattice point. A special type of primitive cell possessing the full symmetry of the Bravais lattice is the Wigner-Seitz cell. It is the locus

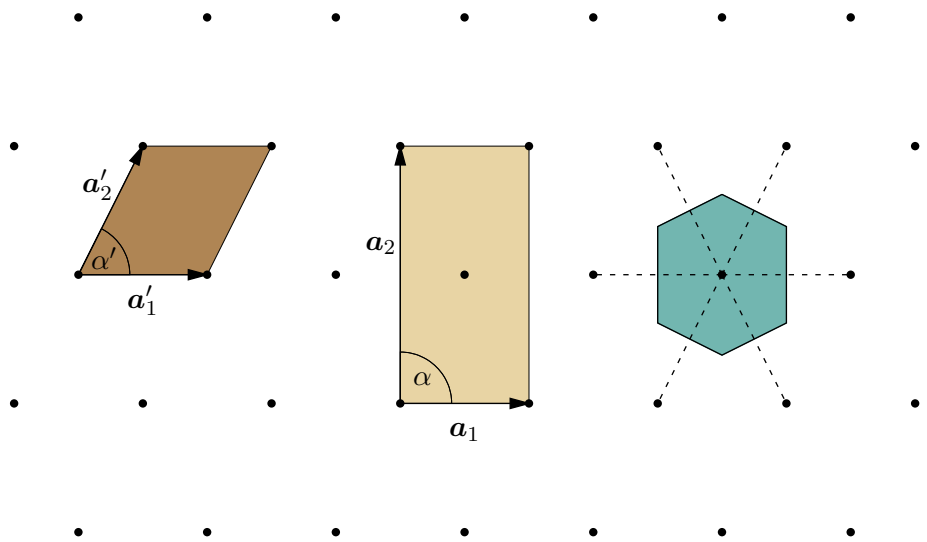

Figure 2.1 Illustration of different unit cells in a 2D lattice: Primitive cell (dark brown), typical conventional cell (light brown), Wigner-Seitz cell (blue)

of points that is closer to a given lattice point than to any other lattice point. Unit cells that are larger than the primitive cell are called conventional cells. Usually conventional cells are chosen according to the crystal symmetry and contain an integer number of lattice points. For describing a real crystal the physical unit of atoms, molecules, ions, etc. located within each primitive cell has to be defined. This unit is called basis of the crystal.

Figure 2.1 illustrates different choices for unit cells in a two dimensional (2D) lattice. The conventional cell (light brown) contains two lattice points, while the other two (primitive) cells contain only one. In blue, the Wigner-Seitz cell is shown. It is constructed by all lines (planes in three dimensional (3D)) that perpendicularly bisect the vectors from one lattice point to all neighboring lattice points. Two of the most important Bravais lattices are shown in figure 2.2. Almost forty elements crystallize in this face-centered cubic (fcc) (left) and the body-centered cubic (bcc) (right) lattice.

At this point we should keep in mind that real crystals are never perfect on a macroscopic scale, i. e. instead of being an ideal crystal as described, real crystals possess lattice defects. An important group of defects are single missing atoms and multiple missing atoms next to each other, so-called monovacancies and multivacancies, respectively. As their influence on positrons is crucial they will be further discussed in chapter 3.3.3.

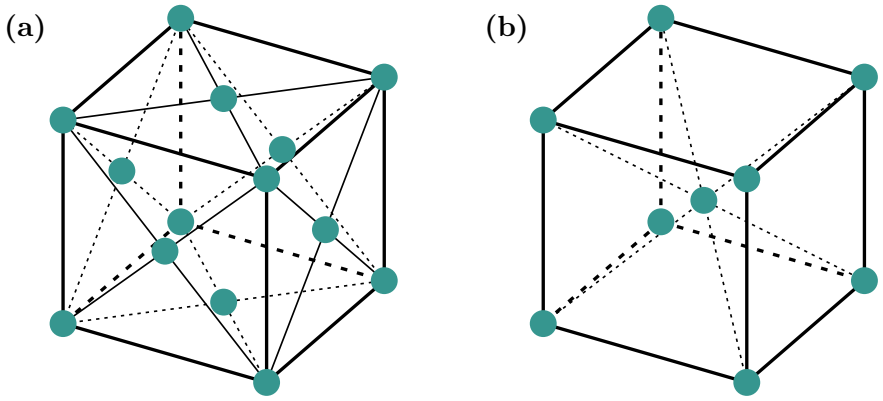

Figure 2.2 The two most important cubic Bravais lattices: (a) face-centered cubic (fcc) and (b) body-centered cubic (bcc)

2.1.2 Reciprocal Space

The reciprocal lattice is defined by the set of all wave vectors, which create plane waves with the periodicity of a given Bravais lattice. Expressed as an equation this means, that

$$e^{i\mathbf{G}\cdot\mathbf{R}} = 1 \tag{2.2}$$

must be satisfied for all reciprocal lattice vectors $\mathbf{G}$. For all sets of $\mathbf{R}$, which build a Bravais lattice in real space, the reciprocal lattice is also a Bravais lattice. The reciprocal lattice vectors, $\mathbf{b_1}$, $\mathbf{b_2}$ and $\mathbf{b_3}$, are related to the real space lattice vectors, $\mathbf{a_1}$, $\mathbf{a_2}$ and $\mathbf{a_3}$, by

$$\mathbf{b_1} = 2\pi\frac{\mathbf{a_2}\times\mathbf{a_3}}{\mathbf{a_1}\,(\mathbf{a_2}\times\mathbf{a_3})};\quad \mathbf{b_2} = 2\pi\frac{\mathbf{a_3}\times\mathbf{a_1}}{\mathbf{a_1}\,(\mathbf{a_2}\times\mathbf{a_3})};\quad \mathbf{b_3} = 2\pi\frac{\mathbf{a_1}\times\mathbf{a_2}}{\mathbf{a_1}\,(\mathbf{a_2}\times\mathbf{a_3})}. \tag{2.3}$$

Furthermore, one should note that if $\mathbf{a_1}$, $\mathbf{a_2}$, $\mathbf{a_3}$ are primitive vectors, $\mathbf{b_1}$, $\mathbf{b_2}$, $\mathbf{b_3}$ are primitive vectors of the reciprocal lattice and that the reciprocal lattice has the same rotational and translational symmetries as the real space Bravais lattice. The Wigner-Seitz cell of the reciprocal lattice is called Brillouin zone (BZ). Similarly to the real space lattice vectors $\mathbf{R}$, the reciprocal lattice vectors $\mathbf{G}$ can be written as

$$\mathbf{G} = h\mathbf{b_1} + k\mathbf{b_2} + l\mathbf{b_3}, \tag{2.4}$$

where h, k and l are integers and known as Miller indices of the real space lattice planes. Thereby, the real space lattice plane with the Miller indices (hkl) lies perpendicular to the reciprocal lattice vector $\mathbf{G}$ with identical set of

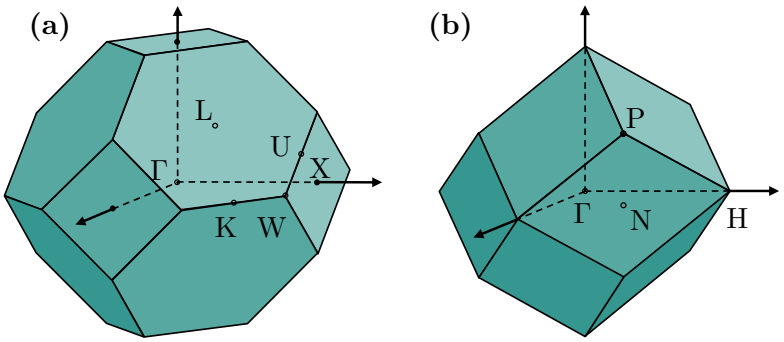

Figure 2.3 First Brillouin zone of a fcc (a) and bcc (b) lattice

integers (hkl).

The reciprocal lattice of a fcc structure is a bcc lattice and vice versa. Using the construction method, explained for the Wigner-Seitz cell in the last section, we can get the first BZs shown in figure 2.3. For both BZs various high-symmetry points are also shown in the figure.

2.2 Electrons in a Crystal

In 1897 Thomson discovered the free electron by showing that cathode rays were composed by negatively charged particles [Tho97]. Only a few years later Drude [Dru00b, Dru00a] was able to explain electronic and thermal conductivity in metals and predict the correct form of Ohm's law by treating the free electrons in a metal as a classical gas. However, since Drude approximated the velocity of the electrons wrongly by the classical Maxwell-Boltzmann-Distribution (as quantum mechanics and Pauli principle had not been formulated at that time), the model fell short in explaining all known properties of metals, e. g. the heat capacity, considerably well. It took almost another thirty years until [Som28] combined Drude's classical theory with the quantum mechanical Fermi-Dirac statistics and thus formulated the theory, today known as the free electron model.

This section starts with introducing the free electron model, which is then transferred into the periodic potential of a real crystal lattice from which the Bloch theorem and the model of nearly free electrons follows. Finally, the concept of the Fermi surface (FS) which plays a central role in condensed matter physics, is introduced.

2.2.1 Free Electrons

The starting point for the description of the free electron gas is the Schrödinger equation

$$-\frac{\hbar^2}{2m_e}\boldsymbol{\nabla}^2\psi(\mathbf{r}) = \epsilon\psi(\mathbf{r}), \tag{2.5}$$

where m_e is the electron rest mass, $\psi(\mathbf{r})$ is the electron wave-function and ϵ is the energy eigenvalue of the electron. This purely kinetic equation directly follows from two approximations, which lay the foundation of the Sommerfeld theory. Firstly, the electrons are independent, i. e. they do not interact with one another and secondly, the periodic potential of the crystal is replaced by a constant potential. By differentiation we could show that plane-waves of the form

$$\psi_{\mathbf{k}}(\mathbf{r}) = \frac{1}{\sqrt{V}}e^{i\mathbf{k}\cdot\mathbf{r}}, \tag{2.6}$$

are a solution of Eq. 2.5 which fulfill the boundary conditions

$$\begin{aligned}\psi(x+L,y,z) &= \psi(x,y,z),\\ \psi(x,y+L,z) &= \psi(x,y,z),\\ \psi(x,y,z+L) &= \psi(x,y,z).\end{aligned} \tag{2.7}$$

For simplicity the crystal is assumed to be cubic with the volume $V = L^3$. Eq. 2.6 is normalized in a way that the probability to find the electron inside the crystal is one:

$$1 = \int_V \mathrm{d}\mathbf{r}|\psi(\mathbf{r})|^2 \tag{2.8}$$

The electron wave vector $\mathbf{k}$ is an eigenvalue of the momentum operator $\mathbf{p} = -i\hbar\boldsymbol{\nabla}$ as

$$\frac{\hbar}{i}\boldsymbol{\nabla}e^{i\mathbf{k}\cdot\mathbf{r}} = \hbar\mathbf{k}e^{i\mathbf{k}\cdot\mathbf{r}}, \tag{2.9}$$

and thus it follows $\mathbf{p} = \hbar\mathbf{k}$. The energy eigenvalue $\epsilon_{\mathbf{k}}$ of the eigenstate $\psi_{\mathbf{k}}(\mathbf{r})$ is

$$\epsilon_{\mathbf{k}} = \frac{\hbar^2|\mathbf{k}|^2}{2m_e}. \tag{2.10}$$

This gives a parabolic dispersion relation of $\epsilon_{\mathbf{k}}$ in momentum space which is called energy band.

Following from the boundary conditions 2.7 and the plane-wave solution 2.6,

$$e^{ik_xL} = e^{ik_yL} = e^{ik_zL} = 1 \tag{2.11}$$

has to be fulfilled. This means that only discrete values of $\mathbf{k}$,

$$k_x = \frac{2\pi n_x}{L}, \quad k_y = \frac{2\pi n_y}{L}, \quad k_z = \frac{2\pi n_z}{L}, \tag{2.12}$$

with n_x, n_y, n_z being integers, are allowed. This limits the number of allowed orbitals per volume element $(2\pi/L)^3$ of k-space to two as for every discrete wave vector two spin quantum numbers are allowed. Thus the total number of orbitals N of energy $\leq \epsilon$ and with a magnitude of wave vector $\leq k$ is given as

$$N = 2 \cdot \frac{4\pi k^3/3}{(2\pi/L)^3} = \frac{V}{3\pi^2} k^3 = \frac{V}{3\pi^2} \left(\frac{2m_e \epsilon}{\hbar^2} \right)^{3/2}. \tag{2.13}$$

By differentiation we can finally calculate the density of states (DOS) for electrons:

$$D(\epsilon) = \frac{\mathrm{d}N}{\mathrm{d}\epsilon} = \frac{V}{2\pi^2} \left(\frac{2m_e}{\hbar^2} \right)^{3/2} \sqrt{\epsilon}. \tag{2.14}$$

2.2.2 Bloch Theorem

The free electron model is able to describe physical properties like heat capacity, thermal and electrical conductivity, magnetic susceptibility and the electrodynamics of metals well. However, it still fails to give answers to other important questions of condensed matter physics like the distinction between metals, semimetals, semiconductors and insulators or the occurrence of positive values of the Hall coefficient. In 1929 Bloch [Blo29] extended the theory of free electrons to periodic crystal potentials by still neglecting electron-electron interactions. By introducing the periodic potential $U(\mathbf{r} + \mathbf{R}) = U(\mathbf{r})$ the Schrödinger equation can be rewritten as

$$\left[-\frac{\hbar^2}{2m_e} \boldsymbol{\nabla}^2 + U(\mathbf{r}) \right] \psi(\mathbf{r}) = \epsilon \psi(\mathbf{r}). \tag{2.15}$$

According to Bloch the solutions of equation 2.15 are plane waves multiplied by a function $u_{j\mathbf{k}}(\mathbf{r}) = u_{j\mathbf{k}}(\mathbf{r} + \mathbf{R})$ possessing the periodicity of the Bravais lattice:

$$\psi_{j\mathbf{k}}(\mathbf{r}) = u_{j\mathbf{k}}(\mathbf{r}) e^{i\mathbf{k}\cdot\mathbf{r}}. \tag{2.16}$$

The index j is called band index as there are multiple eigenstates $\psi_{j\mathbf{k}}(\mathbf{r})$ for a chosen $\mathbf{k}$ and thus multiple energy eigenvalues $\epsilon_{j\mathbf{k}}$. By considering the $\mathbf{k}$ space as continuous, we can also write the eigenvalues $\epsilon_{j\mathbf{k}}$ as energy functions

$\epsilon_j(\mathbf{k})$ which are called bands. The multiplicity of the bands becomes obvious by applying the momentum operator to $\psi_{j\mathbf{k}}(\mathbf{r})$,

$$\frac{\hbar}{i}\boldsymbol{\nabla}\psi_{j\mathbf{k}}(\mathbf{r}) = \frac{\hbar}{i}\boldsymbol{\nabla}\left(u_{j\mathbf{k}}(\mathbf{r})e^{i\mathbf{k}\cdot\mathbf{r}}\right) = \hbar\mathbf{k}\psi_{j\mathbf{k}} + e^{i\mathbf{k}\cdot\mathbf{r}}\frac{\hbar}{i}\boldsymbol{\nabla}u_{j\mathbf{k}}(\mathbf{r}), \tag{2.17}$$

which shows that $\psi_{j\mathbf{k}}(\mathbf{r})$ is in general no momentum eigenstate. However, the so-called crystal momentum $\hbar\mathbf{k}$, which is only defined in the first BZ is the natural generalization of $\mathbf{p}$ in a periodic potential. Hence, the crystal momentum $\mathbf{k}$ can be seen as a quantum number reflecting the translation symmetry of the periodic potential, as the momentum $\mathbf{p}$ is the quantum number reflecting the continuous translation symmetry of free space. As an electron moving in a periodic potential experiences a force equal to the gradient of that potential, the electron momentum $\mathbf{p} = \hbar(\mathbf{k} + \mathbf{G})$ is not conserved. However, the crystal momentum $\mathbf{k}$ is conserved to within $\hbar\mathbf{G}$.

2.2.3 Fermi Surface

For all electronic states existing in any given band of a metal, the Fermi-Dirac distribution determines the ones that will be occupied, as electrons are fermions and, therefore, obey the Pauli exclusion principle. The probability that the state $\epsilon_j(\mathbf{k})$ is occupied at temperature T is given by

$$f\left[\epsilon_j\left(\mathbf{k}\right)\right] = \frac{1}{\exp\left(\frac{\epsilon_j(\mathbf{k})-\epsilon_F}{k_BT}\right)+1}, \tag{2.18}$$

where ϵ_F is the Fermi energy and k_B is the Boltzmann constant. If the temperature is reduced to absolute zero, Eq. 2.18 is a step function and all parts of the band $\epsilon_j(\mathbf{k})$ with $\epsilon_j(\mathbf{k}) < \epsilon_F$ will be occupied, and the fraction for which $\epsilon_j(\mathbf{k}) > \epsilon_F$ will be unoccupied. For non-zero temperatures the step function softens and some electrons can overspill from states below ϵ_F into states above ϵ_F. However, ϵ_F is still a meaningful quantity in separating occupied and unoccupied states as typical values of ϵ_F in metals ($\approx 5\,\mathrm{eV}$) are orders of magnitude larger than the thermal energy in the order of k_BT (e. g. $\approx 25\,\mathrm{meV}$ at room temperature).

Since $\mathbf{k}$ is a vector in three-dimensional space and for every $\mathbf{k}$ several bands $\epsilon_j(\mathbf{k})$ exist, the complete pictorial representation of the band structure of a crystal would require a four-dimensional space. One possibility to overcome

this problem is to draw constant energy surfaces, with $\epsilon_j(\mathbf{k}) = \epsilon$, for the various band indices j and for various constant energies ϵ. One special constant energy surface, defined by

$$\epsilon_j(\mathbf{k}) = \epsilon_F \tag{2.19}$$

is the so-called Fermi surface, which marks the boundary between the occupied and unoccupied states of the band j. As mentioned above this is only rigorously true at absolute zero temperature, however, since $k_B T \ll \epsilon_F$ in practice, this is still a very good approximation for higher temperatures. For free electrons, the FS is spherical, however, in a real three-dimensional crystal there may be several bands that cross ϵ_F and, therefore, create multiple FS sheets.

The importance of the precise shape and topology of the FS originates from the fact, that only electrons close to the FS can respond to dynamic perturbations, and thus lead to phenomena like magnetism or superconductivity [CW73].

2.3 Electronic Structure Calculations and Electron Momentum Density

In 1964 Hohenberg and Kohn developed the so-called density functional theory (DFT), which postulates that all properties of a non-degenerate ground state of an electron system are completely given by its electron density $n(\mathbf{r})$ [HK64]. One year later Kohn and Sham extended these basic principles, which leads to what is nowadays often refered to as Hohenberg-Kohn-Sham (HKS)-theory [KS65]. Even if it was originally used to describe inhomogeneous electron gases, it later became the standard method to theoretically calculate band structures of crystalline materials [KV83].

This section will introduce the basic principles of DFT and how it connects to the electron momentum density (EMD), which plays an important role in the experimental techniques used in this work. However, the introduction of this theoretical framework will be kept brief and limited to DFT, as the theoretical calculations presented in this work have not been performed by the author himself.

Hohenberg and Kohn showed that for any external potential $V_{ext}(\mathbf{r})$ a func-

tional of the electron density $F[n(\mathbf{r})]$ exists, so that

$$E = \int V_{\text{ext}}(\mathbf{r}) n(\mathbf{r})\, \mathrm{d}\mathbf{r} + F[n(\mathbf{r})] \tag{2.20}$$

has its minimum at the correct ground state energy E associated with $V_{ext}(\mathbf{r})$. Based on this [KS65] developed a system of self consistent one-particle functions of the form

$$\left(-\frac{1}{2}\Delta + V_{\text{eff}}(\mathbf{r})\right) \psi_j(\mathbf{r}) = \epsilon_j \psi_j(\mathbf{r}) \tag{2.21}$$

to describe the electronic ground state. Here, the effective potential can be written as a sum of the electrostatic potential of all electric charges and the exchange-correlation-potential $V_{xc}[n(\mathbf{r})]$

$$V_{\text{eff}}(\mathbf{r}) = V_{\text{ext}}(\mathbf{r}) + \int \mathrm{d}V_{\text{eff}}(\mathbf{r}') \frac{n(\mathbf{r}')}{|\mathbf{r} - \mathbf{r}'|} + V_{\text{xc}}[n(\mathbf{r})], \tag{2.22}$$

with

$$n(\mathbf{r}) = \sum_j |\psi_j(\mathbf{r})|^2. \tag{2.23}$$

According to section 2.2.2 we already know, that in the case of crystal lattices, the solution for the system of equations 2.21 is given by Bloch waves

$$\psi_{j\mathbf{k}}(\mathbf{r}) = u_{j,\mathbf{k}}(\mathbf{r}) e^{i\mathbf{k}\cdot\mathbf{r}}. \tag{2.24}$$

Due to the periodicity of the crystal lattice and thus $u_{j,\mathbf{k}}$, this equation can be expanded into a Fourier series

$$\psi_{j\mathbf{k}}(\mathbf{r}) = \sum_{\mathbf{G}} A_{j,\mathbf{G}}(\mathbf{k}) e^{i(\mathbf{G}\mathbf{k})\cdot\mathbf{r}}. \tag{2.25}$$

Similar to the real space electron density in equation 2.23, in the single particle model of the HKS-theory, the EMD $\rho(\mathbf{p})$ can be written as the sum of the squared momentum space wave functions $\chi_{j\mathbf{k}}(\mathbf{p})$

$$\rho(\mathbf{p}) = \sum_{\mathbf{k},j} n_{\mathbf{k},j} \left|\chi_{j\mathbf{k}}(\mathbf{p})\right|^2 = \sum_{\boldsymbol{k},j} n_{\boldsymbol{k},j} \left| \int \psi_{\boldsymbol{k},j}\left(\boldsymbol{r}\right) \mathrm{e}^{-i\boldsymbol{p}\cdot\boldsymbol{r}} \mathrm{d}\boldsymbol{r} \right|^2, \tag{2.26}$$

where the momentum space wave function is the Fourier transform of the real space wave function and $n_{\boldsymbol{k},j} = 0$ and $n_{\boldsymbol{k},j} = 1$ for completely unoccupied and fully occupied states, respectively. By applying equation 2.25 to equation 2.26

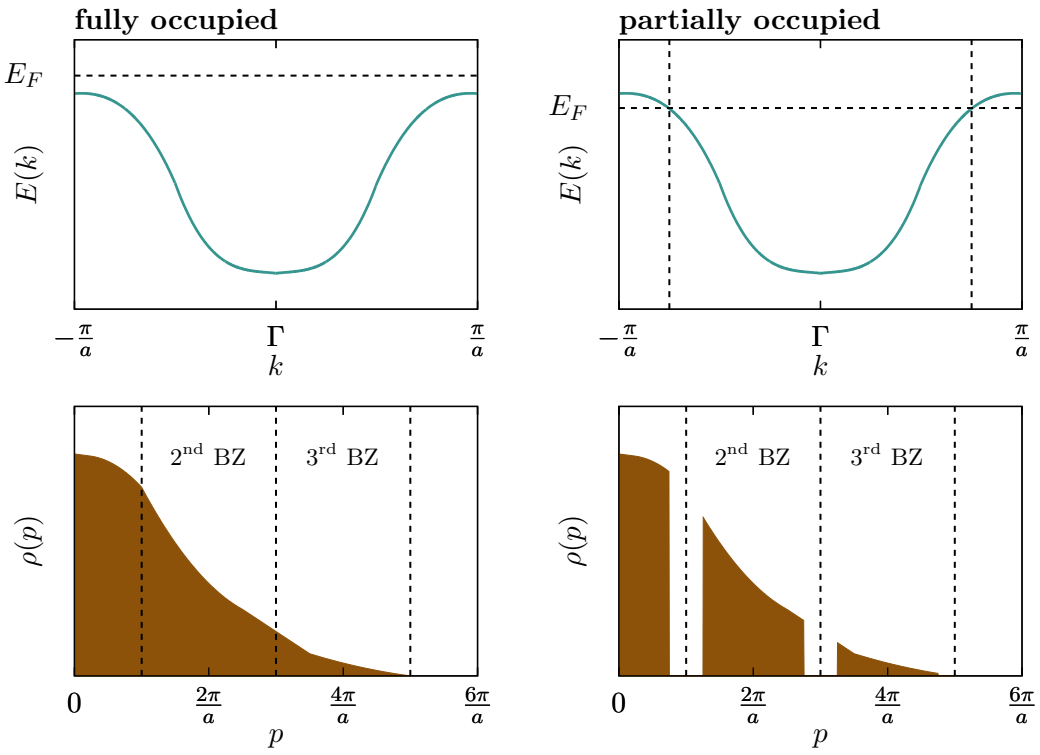

Figure 2.4 Band structure (top left) and EMD (bottom left) of a one-dimensional insulator and the band structure (top right) and EMD (bottom right) of a one-dimensional metal (bottom right). In the case of the metal, the band is only partially filled (band crosses the Fermi energy), which leads to discontinuities in the EMD. The total EMD of a real crystal is always a sum of contributions from multiple fully occupied states and eventually a few partially unoccupied states.

we get

$$\rho(\mathbf{p}) = \sum_{\mathbf{k},j} n_{\mathbf{k},j} \sum_{\mathbf{G}} \left| A_{j,\mathbf{G}}(\mathbf{k}) \right|^2 \delta(\mathbf{p} - \mathbf{k} - \mathbf{G}). \tag{2.27}$$

Originating from the δ-function in the previous equation, the Fourier coefficients $A_{j,\mathbf{G}}(\mathbf{k})$ of one electronic state are distributed over the whole momentum space. As shown in figure 2.4, $\rho(\mathbf{p})$ is continuous for completely filled states (left side), while it shows sharp breaks in case a band crosses the Fermi level (right side). In both cases, however, it is distributed over the whole momentum space and decreases with higher momenta. Furthermore, $\rho(\mathbf{p})$ exhibits the crystal point symmetries, but does not have the translational symmetry of the reciprocal lattice. However, as shown in section 2.16 in a periodic lattice, the translational symmetry can be recovered by transitioning to the crystal momentum $\mathbf{k}$-space.

This can be achieved by applying the Lock-Crisp-West (LCW)-theorem,

developed and first applied by [LCW73] to 2D-ACAR data, which 'folds' the **p**-space distribution back into the first BZ. According to the LCW-theorem the **k**-space occupation $\rho_{\mathrm{LCW}}(\mathbf{k})$ can be calculated by a summation of the EMD over the reciprocal lattice vectors

$$\rho_{\mathrm{LCW}}(\mathbf{k}) = \sum_{\mathbf{G}'} \rho\left(\mathbf{p}+\mathbf{G}'\right) = \sum_{\mathbf{G}'} \sum_{\mathbf{k},j} n_{\mathbf{k},j} \sum_{\mathbf{G}} \left| A_{j,\mathbf{G}}(\mathbf{k}) \right|^2 \delta(\mathbf{p}-\mathbf{k}-\mathbf{G}+\mathbf{G}'). \tag{2.28}$$

In contrast to equation 2.27, here the δ-function produces the same **p**-space density at each reciprocal lattice point assuming summation over all (infinitely number) reciprocal lattice points.

While filled bands become flat by applying the LCW-theorem the FS-breaks should coincide and therefore become more distinct. Therefore, LCW-backfolding is a common method to recover FS information from the EMD.

Chapter 3

Condensed Matter Physics with Positrons

In 1928 P. Dirac derived from solutions of the relativistic description of the Schrödinger equation that electrons can have negative and positive charge without directly proposing the existence of a new particle [Dir28]. In a follow-up article in 1931 Dirac predicted the not yet observed "anti-electron" as a new particle having the same mass but opposite charge as the electron [Dir31]. He also stated that it is difficult to observe them in nature due to their rapid rate of recombination with electrons, but attested the new particle a high stability in vacuum. In 1932 Anderson finally detected the positron for the first time [And33].

In this chapter the fundamentals of positron physics and the application of positrons in condensed matter physics will be introduced. As the universe is predominantly filled with matter some effort has to be undertaken to produce anti-matter. Therefore, the first section of this chapter will deal with the production of positrons, before a bound state of electron and positron, the so-called positronium (Ps) is introduced. The third, and most extensive part of this chapter deals with the role of the positron as a probe particle in condensed matter physics and different experimental techniques associated with it.

3.1 Positron Sources

Positrons are predominantly produced by two different processes, firstly β^+ decay and secondly pair production. Sources exploiting the radioactive decay are mostly used in laboratory scale experiments while the second path is mainly used at large scale facilities. Both principles will be introduced in the following

sections, however, a detailed discussion is limited to the ^{22}Na-isotope, as it is the source of choice for the 2D-ACAR spectrometer used in this work (see section 4.1.3), and the high-intensity monoenergetic positron source neutron induced positron source Munich (NEPOMUC).

Radioactive Sources

Unstable proton rich atoms are likely to convert a proton into a neutron either by electron capture or by β^+ decay. The reaction scheme of the latter is given by,

$$\mathrm{Z}^{\mathrm{A}} \quad \longrightarrow \quad (\mathrm{Z}-1)^{\mathrm{A}} + \mathrm{e}^+ + \nu_\mathrm{e}, \tag{3.1}$$

where a nucleus with Z protons and a mass number A decays into a nucleus with $(\mathrm{Z}-1)$ protons and the identical mass number, under emission of a positron e^+ and an electron neutrino ν_e.

Since we deal with a three body decay, the β-spectrum of this process is continuous and was first derived analytically by E. Fermi in 1934 [Fer34], assuming a neutrino mass of zero. The positron intensity $N(E)$ in the energy interval $\mathrm{d}E$ is given as,

$$N(E)\,\mathrm{d}E = const.\, F(Z,E)\, p\, E\, (E_\mathrm{max} - E)^2\ \mathrm{d}E \tag{3.2}$$

where $E = \sqrt{m_\mathrm{e}c^4 + p^2c^2}$, E_max and p are the total positron energy, the endpoint energy and the linear positron momentum, respectively. The factor $F(Z,E)$ is the correction for the influence of the Coulomb field of the daughter nucleus on the positrons and called the Fermi function. In essence it is given by the ratio of the electron density at the nucleus to the density at infinite distance evaluated at the nuclear radius R [KR65]. For positron emission $F(Z,E)$ is given by

$$\begin{aligned} F &= \frac{2(1+\gamma_0)}{(2pR/\hbar)^{2(1-\gamma_0)}} \frac{\left|\Gamma(\gamma_0 + iv)\right|^2}{\left[\Gamma(2\gamma_0+1)\right]^2} e^{\pi v}, \\ \gamma_0 &= \sqrt{1-(\alpha \mathrm{Z})^2}, \quad v = -\alpha \mathrm{Z} E/cp, \end{aligned} \tag{3.3}$$

with the fine-structure constant α, the speed of light c, the reduced Planck constant $\hbar$ and the gamma function Γ.

Due to parity violation in the weak interaction, first suggested by Lee and

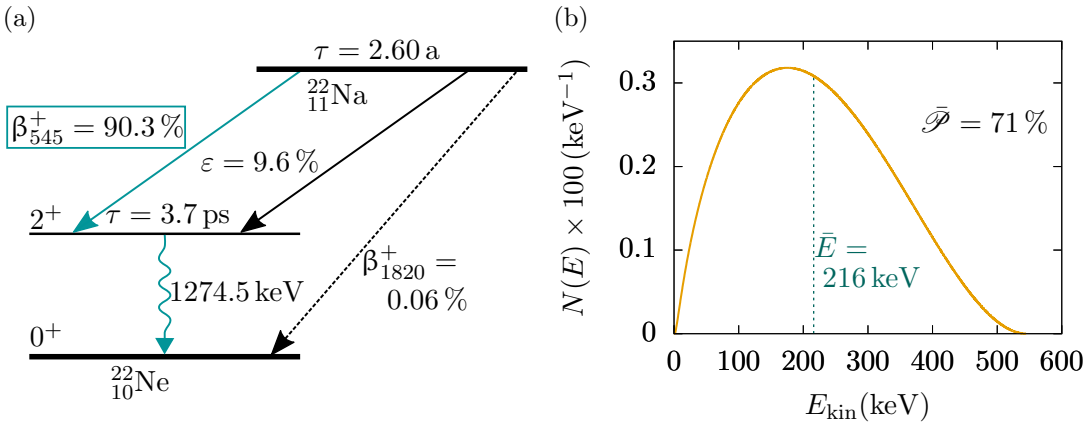

Figure 3.1 (a) Decay schema of ^{22}Na [Bas15]. The most relevant branch for positron production is the β^+ decay to an excited ^{22}Ne state (blue) which transitions into the ground state under emission of a 1275 keV photon. Electron capture ε and direct β^+ decay into the ^{22}Ne ground state (dashed line) are much less likely. (b) β-spectrum of the positrons emitted from ^{22}Na-decay. The mean energy of the spectrum is at $\bar{E} = 216\,\mathrm{keV}$ and the mean positron polarization is $\bar{\mathcal{P}} = 71\,\%$.

Yang [LY56], the positrons created by β^+ decay are longitudinally spin polarized. The polarization is found to be

$$\mathcal{P} = \frac{\mathrm{d}N_\uparrow - \mathrm{d}N_\downarrow}{\mathrm{d}N_\uparrow + \mathrm{d}N_\downarrow} = \frac{v}{c}, \tag{3.4}$$

where $v = c^2 p/E$ is the positron velocity. The symbols $\mathrm{d}N_\uparrow$ and $\mathrm{d}N_\downarrow$ denote the partial creation rates of positrons spinning parallel and antiparallel to the momentum of the positron, respectively [KR65].

The most prominent nuclide for laboratory sources is ^{22}Na, which decays into ^{22}Ne as shown in figure 3.1(a). The dominant decay channel (blue) with a branching ratio of 90.3 % is the β^+ decay into an excited ^{22}Ne state. Its maximum energy is 545 keV. After 3.7 ps the daughter nucleus further deexcites into the ground state under the emission of a 1275 keV photon, which is perfectly suited as a start signal in positron annihilation lifetime spectroscopy (PALS). Besides the high branching ratio and the prompt gamma emission, the long half life of 2.6 a is also a big advantage of this nuclide. It guarantees an approximately constant activity during long measurement times of several weeks. The energy distribution of the emitted positrons, according to equation 3.2, is shown in figure 3.1(b). From this analytical spectrum (see equation 3.2) an average energy of $\bar{E} = 216\,\mathrm{keV}$ and an average polarization (equation 3.4) $\bar{\mathcal{P}} = 71\,\%$ can be determined.

The Positron Source NEPOMUC

The NEPOMUC positron source at FRM II [1] operates by a cascade process of neutron capture and subsequent pair production. Fig. 3.2 shows a technical drawing of the in-pile element of NEPOMUC, which is placed in the D_2O tank of the reactor. Thermal neutrons are captured in the cadmium cap almost exclusively by the nuclear reaction ^{113}Cd(n,γ)^{114}Cd, as the isotope ^{113}Cd shows an extremely high neutron capture cross section of 20 600 barn. On average 2.3 high energy γ-quanta with an energy higher than 1.5 MeV are released in the deexcitation from a highly excited ^{114}Cd state into the ground state [HKR$^+$04]. As the natural abundance of the ^{113}Cd isotope is 11.6 % the Cd cap of NEPOMUC is enriched to about 80 % to ensure a lifetime of 25 years [HCG$^+$13]. The platinum structure serves two purposes. Firstly, it is the predominant origin of the pair production due to its high atomic number. Secondly, it moderates the produced positrons and emits the thermal positrons as Pt has a negative work function for positrons. Through the electric lens system, the emitted positrons are formed to a beam with a kinetic energy of 1 keV, which is then guided by a longitudinal magnetic guidance field of typically 7 mT. In its present state, the primary beam of NEPOMUC delivers more than 10^9 moderated positrons per second [HCG$^+$13].

The beam quality can be further improved by using a remoderator stage between the in-pile element and the connected experiments. Even if the remoderation efficiency is just about 5 % the beam brightness after remoderation is up to forty times higher in contrast to the primary beam [PKE$^+$08]. A very recent upgrade of the remoderator could increase the efficiency by a factor of 1.5 [DEK$^+$20].

The big advantage of NEPOMUC in comparison to β^+ sources is its mono-energetic positron spectrum. This would enable depth-dependent 2D-ACAR measurements and would thus allow to measure the evolution of the electronic structure from surface to bulk. A design study for such a future upgrade was conducted by [Cee15].

[1] Research Neutron Source Heinz Maier-Leibnitz (FRM II)

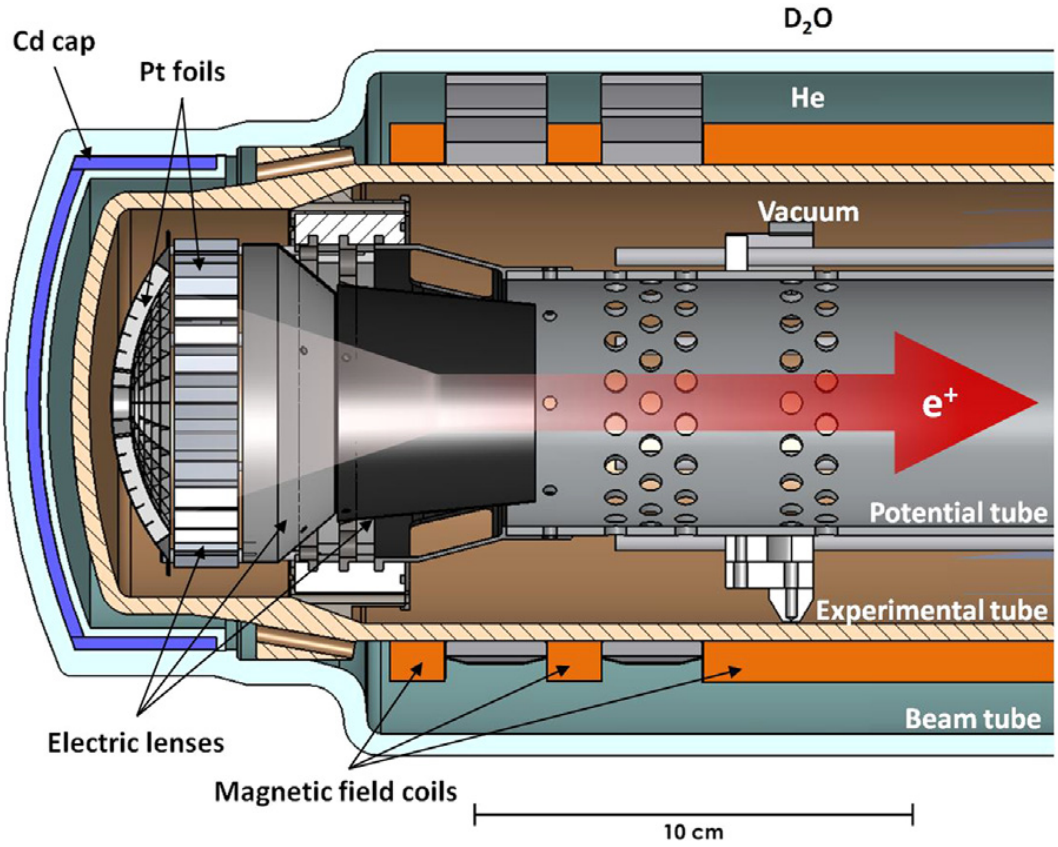

Figure 3.2 Schematics of the in-pile element of NEPOMUC [Hug16].

3.2 Positronium

Only six years after Dirac proposed the existence of the positron [Moh34] suggested a bound state of electron and positron, which he called "Electrum". Even if he correctly approximated the binding energy of the electrum, to be half of the hydrogen binding energy, his work did not get a lot of attention and we nowadays call this bound state positronium as suggested by [Rua45].

This section introduces the hydrogen-like bound state of positrons and electrons, the so-called positronium (Ps), starting with Ps in vacuum and the two spin configurations para-positronium (p-Ps) and ortho-positronium (o-Ps). In the second part the effect of an additional magnetic field will be considered, as the polarization of a β^+-source can be experimentally determined from the fraction of p-Ps and o-Ps created from positrons emitted into a magnetic field [PH57, NNK+00, Cee15].

3.2.1 Positronium in Vacuum

Similar to the Hamiltonian of the hydrogen atom, the Hamiltonian of free Ps (neglecting spin-spin interaction) can be written as

$$\hat{H} = \frac{\hat{\mathbf{p}}^{\mathbf{2}}}{m_\mathrm{e}} - \frac{\alpha\hbar c}{r}, \tag{3.5}$$

where $\hat{\mathbf{p}}$ is the momentum operator, m_e is the electron or positron mass, α is the fine-structure constant, $\hbar$ is the reduced Planck constant, and r is the positron-electron distance. This gives an orbital ground state with a degeneracy of four, which can be split into its hyperfine structure by introducing the spin-spin interaction

$$\hat{H}_\mathrm{hf} = \frac{1}{4}\Delta E_{o-p}\sigma_{\mathbf{e}^+}\sigma_{\mathbf{e}^-}, \tag{3.6}$$

with the Pauli spin matrices σ and the splitting energy $\Delta E_{o-p} = \kappa \cdot 0.8412\,\mathrm{meV}$ between the hyperfine $^1\mathrm{S}_0$ and $^3\mathrm{S}_1$ states. The contact parameter κ gives the ratio between the electron-positron overlap in matter to the overlap in free Ps. In vacuum, of course, κ is equal to unity. The eigenstate $|s, m\rangle$ of the $^1\mathrm{S}_0$ singlet state, the so-called p-Ps with total spin s = 0 and magnetic quantum number $m = 0$ can be expressed as:

$$|0,0\rangle = \frac{1}{\sqrt{2}}\left(|\uparrow\downarrow\rangle - |\downarrow\uparrow\rangle\right). \tag{3.7}$$

For the triplet $^3S_1$, the so-called o-Ps state with spin s = 1, the eigenstates with magnetic quantum number $m = -1$, 0 or 1 can be written as follows:

$$|1,0\rangle = \frac{1}{\sqrt{2}}\left(|\uparrow\downarrow\rangle + |\downarrow\uparrow\rangle\right) \tag{3.8}$$

$$|1,1\rangle = |\uparrow\uparrow\rangle \tag{3.9}$$

$$|1,-1\rangle = |\downarrow\downarrow\rangle\,. \tag{3.10}$$

In equations 3.7 - 3.10 the first arrow denotes the spin orientation of the positron and the second one the spin orientation of the electron [MSEG97].

Without preferred spin polarization of neither positrons nor electrons all states are equally probable to be formed and therefore the fraction of between p-Ps and o-Ps is 1:3. According to charge conjugation invariance [Yan50, WR52] only positronium annihilations following

$$(-1)^{n_\gamma} = (-1)^{l+s} \tag{3.11}$$

are allowed. Here, n_γ is the number of emitted photons and s and l are the spin and orbital angular momentum quantum numbers, respectively. This means that the $^1S_0$ p-Ps state can annihilate under emission an even number of photons while the $^3S_1$ o-Ps needs to annihilate into an odd number of photons[2]. As with every additional photon the annihilation probability is reduced by the fine structure constant α the lifetime of o-Ps $\tau_o = 142\,\text{ns}$ is much longer than the lifetime of p-Ps $\tau_p = 125\,\text{ps}$ [LC00].

3.2.2 Positronium in Magnetic Fields

Now we consider an additional external magnetic field B_{ext}. Therefore, new terms have to be added to the Hamilton operator leading to a total Hamiltonian

$$\hat{H}_{\text{tot}} = \hat{H} + \hat{H}_{\text{hf}} + \frac{1}{2}\hbar\gamma_{\text{e}}B_{\text{ext}}\sigma^z_{e^+} - \frac{1}{2}\hbar\gamma_{\text{e}}B_{\text{ext}}\sigma^z_{e^-}, \tag{3.12}$$

where γ_{e} is the gyro-magnetic ratio and the external magnetic field is taken along the z axis without loosing generality. The eigenstates of the new Hamiltonian,

[2] In general, one photon annihilation is not allowed due to conservation of momentum.

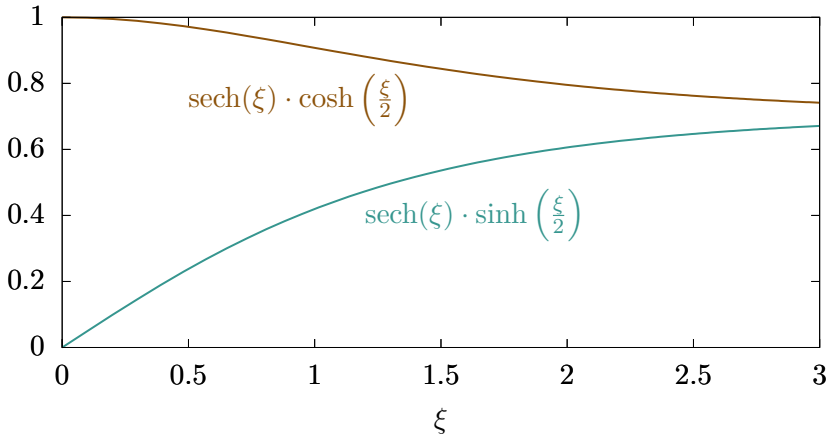

Figure 3.3 Evolution of the mixing of positronium states in external magnetic fields.

are a partial mixture of the eigenstates 3.7 - 3.10 and can be written as

$$|1\rangle = \sqrt{\operatorname{sech}\xi}\left(-\sinh\frac{\xi}{2}\cdot|0,0\rangle + \cosh\frac{\xi}{2}\cdot|1,0\rangle\right), \tag{3.13}$$

$$|2\rangle = |1,1\rangle\,, \tag{3.14}$$

$$|3\rangle = |1,-1\rangle\,, \tag{3.15}$$

$$|4\rangle = \sqrt{\operatorname{sech}\xi}\left(\cosh\frac{\xi}{2}\cdot|0,0\rangle + \sinh\frac{\xi}{2}\cdot|1,0\rangle\right). \tag{3.16}$$

Here, the external magnetic field is included by

$$\xi = \operatorname{arsinh}\frac{B_{\text{ext}}}{B_0} \quad \text{with} \quad B_0 = \frac{\Delta E_{\text{o-p}}}{2\hbar\gamma_{\text{e}}}, \tag{3.17}$$

where B_0 is the hyperfine magnetic field in positronium. Figure 3.3 shows the evolution of the functions defining the mixing between the o-Ps $m = 0$ and p-Ps states as a function of ξ and thus of B_{ext}. From that we can see that state $|1\rangle$ is dominated by the $|1,0\rangle$ o-Ps state and state $|4\rangle$ is dominated by the $|0,0\rangle$ p-Ps state, thus we call them ortho-like and para-like, respectively. With increasing magnetic field, the ortho-like positronium is more likely to oscillate into the p-Ps which in turn leads to a much higher annihilation of the ortho-like positronium in strong magnetic fields in contrast to weak fields [Maj00].

In addition to the dependence of the annihilation rate on the magnetic field, the formation rates of the states 3.13 - 3.16 depend on the magnetic field as well as on the initial polarization of the positrons. The initial occupation numbers

of the states $|1\rangle$ - $|4\rangle$ are given by,

$$n_1 = \frac{1}{4}\left(1 - \mathcal{P}\tanh\xi\right), \tag{3.18}$$

$$n_2 = \frac{1}{4}\left(1 + \mathcal{P}\right), \tag{3.19}$$

$$n_3 = \frac{1}{4}\left(1 - \mathcal{P}\right), \tag{3.20}$$

$$n_4 = \frac{1}{4}\left(1 + \mathcal{P}\tanh\xi\right), \tag{3.21}$$

in case the electrons are initially unpolarized and $\mathcal{P}$ is the positron polarization along the magnetic field direction [Maj00]. This leads to the basic idea of determining the polarization of positrons from measuring the positronium annihilation as a function of the magnetic field [PH57, NNK$^+$00]. However, the discussion of all details of such experiments is beyond the scope of this work and can be found elsewhere [e. g. Cee15, ch. 4].

3.3 Positrons in Condensed Matter

In order to use positrons as a probe in condensed matter physics, we have to understand in detail how positrons interact with matter. This section will give an overview on the different stages a positron undergoes from implantation into a material to annihilation and which information can be gained from the annihilation process.

3.3.1 The Lifecycle of Positrons

Positrons, used in positron annihilation spectroscopy (PAS), are usually created either by β^+ decay or pair production (see section section 3.1). Figure 3.4 shows the processes positrons undergo when interacting with solids. Positrons are either implanted into the solid or reflected from the surface, which leads to a loss of positrons for most experimental purposes. The reflected fraction is significantly material dependent (especially on the atomic number Z) and also depends on incident energy and incident angle. Even for implantation perpendicular to the surface this can range from approximately 11 % at 5 keV in aluminum to up to almost 40 % at 35 keV in gold. After having overcome the surface barrier the positron starts to loose energy via different scattering processes depending on the positrons actual energy and the material. At high

energies of a few MeV, radiative loss effects (i. e., bremsstrahlung) are dominant. Below the MeV range the energy loss is governed by positron-electron scattering, where the positron can even loose 100 % of its energy in a single collision in contrast to electron-electron scattering, where 50 % is the upper limit [SL88]. This process stays dominant down to the Fermi energy below which we have to distinguish between materials with and without band gap. In metals, the positrons will continue to scatter with electrons and loose energy by plasmon excitations. After phonon scattering below 1 eV the positron is fully thermalized. The whole thermalization process in metals takes a few picoseconds [Nie00].

In semiconductors and insulators, the scattering with conduction electrons is not possible, as due to the band gap, no allowed states for the electrons to scatter into are available. Therefore, the much less effective plasmon scattering has to take over at higher energies which subsequently leads to increased thermalization times [SL88].

During thermalization some positrons might reach the surface of the solid and leave the material as fast or epithermal positrons or Ps. The fully thermalized positrons, are able to diffuse through the crystal lattice (white paths in figure 3.4). At some point they either annihilate in the defect free bulk or are trapped in a defect in which they finally also annihilate as they cannot leave the attractive potential of the defect. Those positrons, annihilating in the solid are the ones that are crucial for PAS.

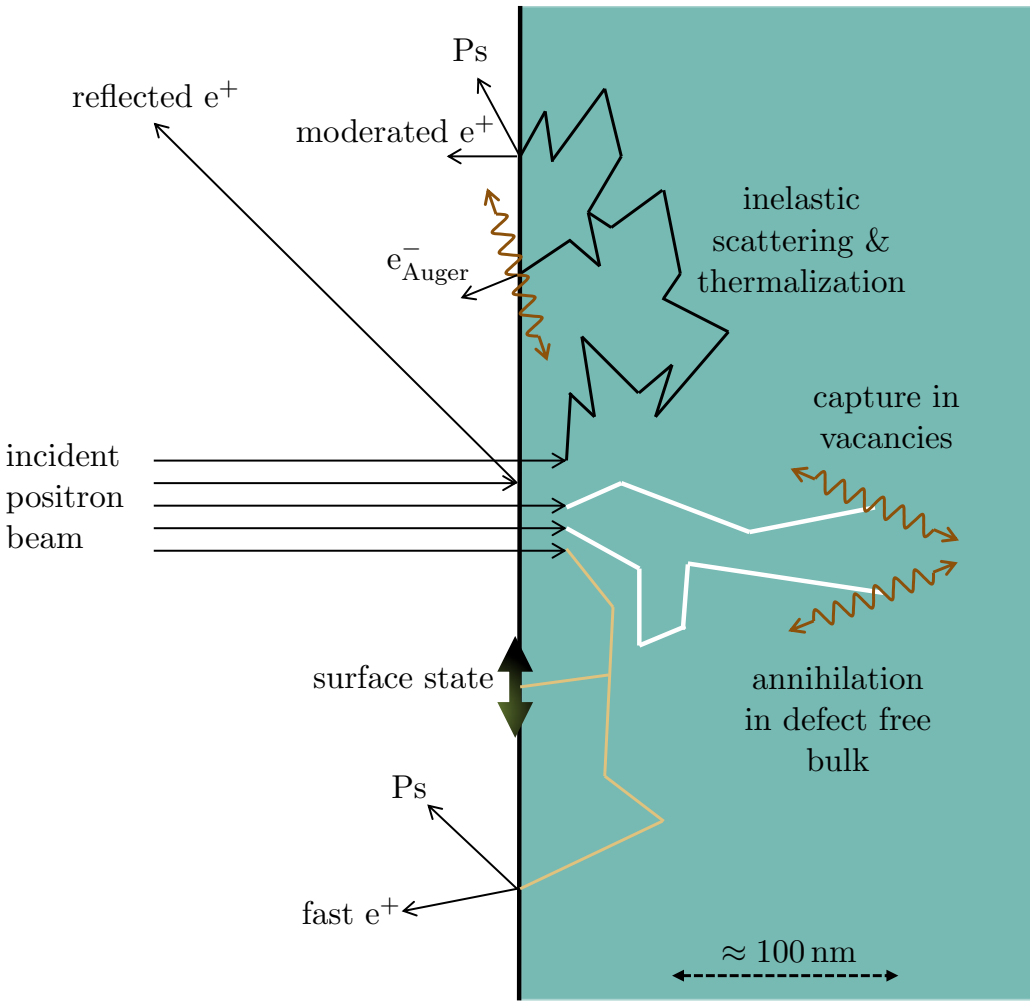

Figure 3.4 Possible processes for positrons interacting with matter. The most desired process for ACAR spectroscopy is the annihilation in defect free bulk (adapted from [Nie00]).

3.3.2 Implantation Depth of Positrons

This section takes a closer look on the depth distribution of positrons after implantation, also known as stopping profile. Makhov derived a model for the implantation of monoenergetic electrons into a solid, which can be adapted for positrons [Mak61a, Mak61b, Mak61c]. The so-called Makhovian distribution is given by

$$I(z) = \frac{m z^{m-1}}{z_0^m} e^{-(z/z_0)^m}, \tag{3.22}$$

with the material dependent shape parameter m. The corrected implantation depth z_0 is given by

$$z_0 = \frac{\bar{z}}{\Gamma\left[(1/m)+1\right]}. \tag{3.23}$$

Here, the Γ-function gives the connection to the mean implantation depth $\bar{z}$ which depends on the initial energy E by

$$\bar{z} = AE^n, \tag{3.24}$$

where A and n are additional material parameters. Even if formulations exist in which the Makhovian profile is only dependent on the density of the material, those profiles might differ significantly from implantation profiles resulting from Monte Carlo simulations. Therefore, nowadays material specific values for m, A and n can be found from Monte Carlo calculations [VN83, VN84, RLG$^+$93, JW93, GA95]. Figure 3.5(a) shows Makhovian implantation profiles of monoenergetic positrons in Cu possessing different kinetic energies. As expected, positrons with higher energies proceed further into the material and their depth distribution is larger. The parameters for the calculations were taken from [JW93].

In the case of β^+ sources, the positrons are not monoenergetic but exhibit a wide energy distribution with high mean and endpoint energies as pointed out in section 3.1. An implantation profile can be calculated by integrating all Makhovian profiles (equation 3.22), weighted with the probability of a positron having the corresponding energy (equation 3.2). Another way to calculate implantation profiles for β^+ sources was first suggested by Brandt and Paulin [BP77] and later applied by others (e. g. [BP77]), with one of the most recent results measured by Dryzek and Singleton [DS06]. From transmission experiments they determine a functional dependence of the mass absorption

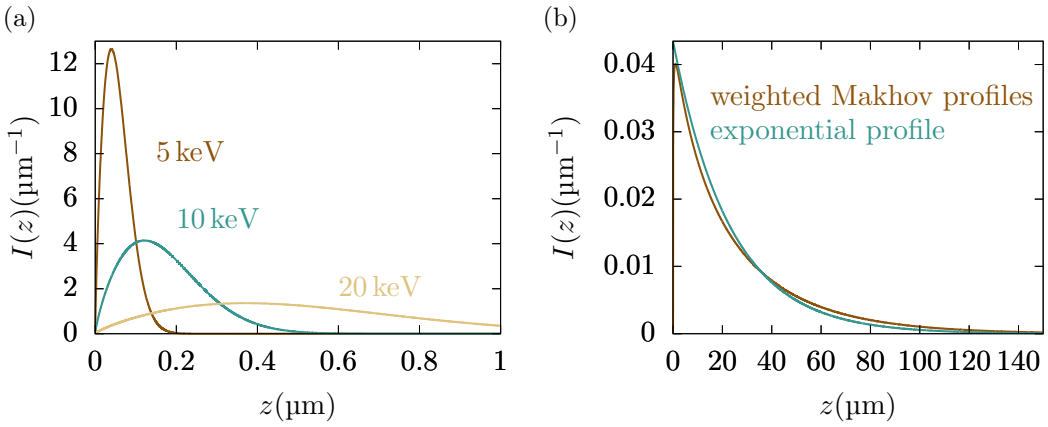

Figure 3.5 (a) Makhovian implantation profiles in Cu of positrons with different kinetic energies. (b) Implantation profile of positrons from a ^{22}Na source in Cu calculated by two different models.

coefficient $\frac{\alpha}{\rho}$ for positrons from ^{22}Na and ^{68}Ge/^{64}Ge sources as

$$\frac{\alpha}{\rho}\left[\frac{\mathrm{cm}^2}{\mathrm{g}}\right] = \frac{12.6\, Z^{0.17}}{E_{\mathrm{max}}^{1.28}}, \tag{3.25}$$

where Z and ρ are the atomic number and density of the target, respectively and E_{max} is the endpoint energy of the β^+-spectrum. Figure 3.5(b) shows, profiles for both approaches. The one, calculated from the weighted Makhovian profiles (brown) is very close to the exponential profile (blue) calculated according to equation 3.25. However, it should be stated that the parameters needed for the Makhovian profiles are predominantly determined for energies up to 50 keV, which is comparably low if we consider typical endpoint energies of the β^+-spectra of several hundred keV.

Comparing both plots of figure 3.5, especially the scales of the z-axes, it becomes clear that experiments with monoenergetic, low-energy positrons are suitable to perform depth dependent experiments. By varying the implantation energy it is possible to distinguish between bulk and surface, which for example enables the determination of positron diffusion length by Doppler broadening spectroscopy (DBS). Experiments with β^+ sources on the other hand, almost exclusively probe the bulk and surface effects can be neglected in typical ACAR experiments.

3.3.3 Positron Diffusion and Trapping

After implantation and thermalization the positrons continue to scatter quasielastically off phonons. The resulting motion is a homogeneous random walk, since due to the absence of external driving forces like an electric field[3], the dominating scattering from acoustic phonons is isotropic. The quantum mechanical Bloch state of the positron can classically be described by diffusive motion.

Starting point is the continuity equation

$$\frac{\partial n(\mathbf{x},t)}{\partial t} + \boldsymbol{\nabla}\vec{J}(\mathbf{x},t) = -\lambda(\mathbf{x})\, n(\mathbf{x},t), \tag{3.26}$$

where $n(\mathbf{x},t)$ is the time dependent positron density, $\vec{J}(\mathbf{x},t)$ is the positron current and $\lambda(\mathbf{x})$ denotes the total loss rate of diffusing positrons. During the diffusion positron can be lost by annihilation or defect trapping, therefore we can write $\lambda(\mathbf{x})$ as follows:

$$\lambda(\mathbf{x}) = \lambda_{\text{ann}} + \kappa(\mathbf{x}). \tag{3.27}$$

Here, λ_{ann} is the annihilation rate in the bulk material and $\kappa(\mathbf{x})$ denotes a spatially varying trapping rate. Fick's law gives a relation for the positron current:

$$\vec{J}(\mathbf{x},t) = -D_+ \boldsymbol{\nabla} n(\mathbf{x},t) = \frac{\eta_+}{e} k_{\text{B}} T\, \boldsymbol{\nabla} n(\mathbf{x},t) \tag{3.28}$$

After the second equality sign we have already applied the Nernst-Einstein relation to express the positron diffusivity D_+ through the mobility η_+ and the temperature T. Finally we arrive at the diffusion equation for thermalized positrons

$$\left(\frac{\eta_+}{e} k_{\text{B}} T \boldsymbol{\nabla}^2 - \lambda_{ann} - \kappa(\mathbf{x})\right) n(\mathbf{x},t) = \frac{\partial n(\mathbf{x},t)}{\partial t}, \tag{3.29}$$

which can be solved by standard numerical techniques [Nie00].

One interesting measure in positron physics is the positron diffusion length

$$L_+ = \sqrt{D_+ \tau} = \sqrt{\frac{D_+}{\lambda}} \tag{3.30}$$

with the lifetime of the Bloch positron τ [HC95]. Diffusion length may vary greatly. While in defect-free metals diffusion lengths of several 100 nm can be expected [BPK$^+$74], Van Petegem et al. [VPDVH$^+$04] reported a diffusion

[3] External fields are neglected in this section.

	Lifetime
free diffusion	$\approx 100\,\mathrm{ps}$
trapped in monovacancy	$\approx 200\,\mathrm{ps}$
trapped in multivacancy	$\approx 400\,\mathrm{ps}$
trapped in surface state	$\approx 400 - 600\,\mathrm{ps}$

Table 3.1 Lifetime of positrons in different bulk states [data taken from SL88]

length below 10 nm in amorphous SiO_2. Especially the defect concentration plays a major role in positron diffusion, as diffusion can be terminated at open-volume defects that posses a lower energy level in contrast to the delocalized Bloch state. Thermal positrons with energies in the meV range cannot leave the defect, as typical defects potentials are in the range of up to a few eV. This trapping process and the high sensitivity of positrons for defects build the basis for experimental defect spectroscopy techniques like PALS and coincident Doppler broadening spectroscopy (CDBS), while it can be "destructive" in ACAR spectroscopy.

3.3.4 Positron Lifetime

The lifetime of a positron in matter strongly depends on the material as well as on the local surroundings of the positron in the material. In the defect free bulk a large number of electrons is available for the positron to annihilate with and the lifetime is short. In contrast, the electron density is strongly reduced in vacancy type defects and therefore trapped positrons live significantly longer. Table 3.1 gives an overview of different positron lifetimes.

This allows us to learn something about the defect distribution of a material by measuring the positron lifetime. To determine "birth" and "death" of the positron a start and stop signal have to be defined. Obviously, a 511 keV gamma ray from the annihilation serves as the stop signal. For the start signal we have to distinguish positron beam experiments, like the pulsed low-energy positron system (PLEPS) instrument at NEPOMUC and laboratory experiments [WSK+94]. The former get a start signal from bunching the positrons and therefore knowing when the positron entered the material. In the laboratory ^{22}Na is typically used as a positron emitter. The prompt emission of a 1275 keV photon is detected and acts as the start signal (compare section 3.1).

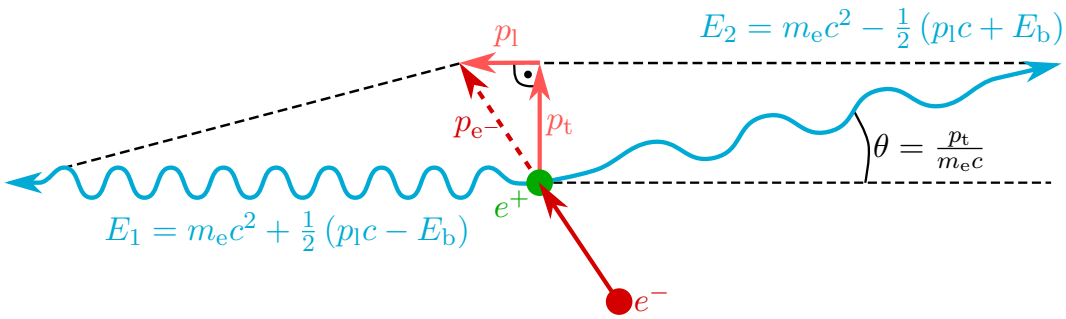

Figure 3.6 Illustration of the conservation of energy and momentum in the positron electron annihilation process into two photons. The transverse momentum of the electron positron pair causes an angular deviation θ, while the longitudinal momentum leads to a Doppler shift of the γ-energy.

3.3.5 Positron Annihilation

After entirely following the positron from creation to annihilation in section 3.3.1, we will now take a close look on the annihilation process, which builds the basis for (coincident) Doppler broadening spectroscopy ((C)DBS) and ACAR experiments. Here, the commonly used approximation is derived from a semi-classical model.

Figure 3.6 depicts the conservation of energy and momentum in the annihilation process. The electron-positron pair predominantly annihilates under emission of two gamma quanta. The sum of the energy of the two photons $E_1 + E_2$ is equivalent to the sum of the energy corresponding to the electron and positron masses minus the binding energy of electron and positron in matter E_b . To get the energies of the single gamma quanta, we additionally have to either add or subtract the kinetic energy component following from the longitudinal momentum of the electron positron pair p_l. From conservation of momentum it follows that

$$E_1 - E_2 = p_\mathrm{l}c = \Delta E, \tag{3.31}$$

which directly shows the proportionality of the Doppler shift of the photons to the longitudinal electron momentum if we neglect the thermal momentum of the positron.

The transverse momentum p_t leads to a deviation of the emission angle between the two photons from 180°. As the energy shift of the photons, originating from E_b and p_l is small in contrast to $m_\mathrm{e}c^2$, we get an angular

deviation θ as follows:

$$\theta \approx \tan(\theta) = \frac{p_\mathrm{t}}{m_\mathrm{e}c}. \tag{3.32}$$

Here, the small angle approximation is valid as the measured angles are in the mrad range. This shows, that θ is directly proportional to the transverse component of the initial electron momentum, if the thermal positron momentum is neglected.

Equations 3.31 and 3.32 show us, that the positron-electron annihilation process gives us access to all components of the electron momentum, by either measuring the Doppler shift ((C)DBS) or the angular deviation (ACAR). Even if ACAR and (C)DBS measure projections of the same quantity, their application in condensed matter physics is very different. Here a short overview on the applications of (C)DBS is given. The basic technique DBS only measures the Doppler broadening of one of the two gammas. This produces a high Compton, small angle scattering and pile-up background, which usually does not allow the comparison of measured spectra to ab initio calculations. The annihilation probability of a positron trapped in a defect with a core electron is strongly reduced in contrast to positrons freely diffusing in the bulk. As valence electrons have a narrow momentum distribution in contrast to core electrons, the one dimensional (1D) Doppler spectrum is also more narrow if a lot of positrons annihilate in defects. Therefore, DBS spectra are usually analyzed by determining a line shape parameter, the S-parameter, which gives a ratio between the counts in a predefined center region of the peak and the overall counts in the spectrum. By performing depth-resolved S-parameter scans we can determine the diffusion length and thus the defect concentration in the material.

In case we want to learn more about the location of defects in a crystal lattice, we can perform CDBS measurements. By measuring both annihilation photons in coincidence, we can strongly reduce the background and acquire more information from electronic core states, which contribute more at higher momenta. As the core states are not influenced by chemical bondings, we thus get information on the element specific surrounding of the positron annihilation site.

3.3.6 Two-Photon Momentum Density

Now we take a closer look at the measurand of an ACAR experiment. By looking at a huge number of annihilations, we measure a projection of the quantum mechanical probability density $\rho^{2\gamma}$, the so-called two-photon momentum density (TPMD). In simple words, the TPMD can be described as the EMD *seen by the positron*. Neglecting electronic correlations, the TPMD can be expressed as

$$\rho^{2\gamma}(\boldsymbol{p}) = \sum_{\boldsymbol{k},j} n_{\boldsymbol{k},j} \left| \int \sqrt{\gamma(\boldsymbol{r})} \psi_{\boldsymbol{k},j}(\boldsymbol{r}) \psi_+(\boldsymbol{r}) \mathrm{e}^{-i\boldsymbol{p}\cdot\boldsymbol{r}} \mathrm{d}\boldsymbol{r} \right|^2, \tag{3.33}$$

which is closely related to the definition of the EMD in equation 2.26. They differ by the positron wave function, $\psi_+(\boldsymbol{r})$, and electron-positron correlations described by the so-called enhancement factor $\gamma(\boldsymbol{r})$ [SK91, DLRNP11].

Positron Wave Function Effects

The sampling of the electronic states by the positron is not uniform as the probability of the positron to be found close to the core is strongly reduced due to the repulsive potential of the nuclei. Figure 3.7 shows a calculation of the positron wave function in fcc nickel. We can clearly see that the probability of finding the positron is highly concentrated at the interstitial space between the atoms.

Jensen and Weiss [JW90] performed theoretical calculations for the annihilation of positron bulk and surface states with different electronic orbitals. Their results show that in all cases the annihilation is dominated by the valence states. In the case of palladium for example, annihilation with 4s and 4p states dominates the annihilation with the more core like states by two orders of magnitude. This makes 2D-ACAR especially sensitive for the investigation of the FS as the electronic states close to the FS dominate the spectra.

However, it should be considered that due to the different symmetry of the electron and positron wave function, the probability within the valence band can vary. This was e. g. shown in ferromagnetic nickle by Singru and Mijnarends [SM74]. It was found that the contribution of two different valence electron bands is reduced in positron annihilation due to the symmetry of the wave function. This deforms the Fermi surface breaks and thus, makes the identification of two Fermi surface sheets difficult.

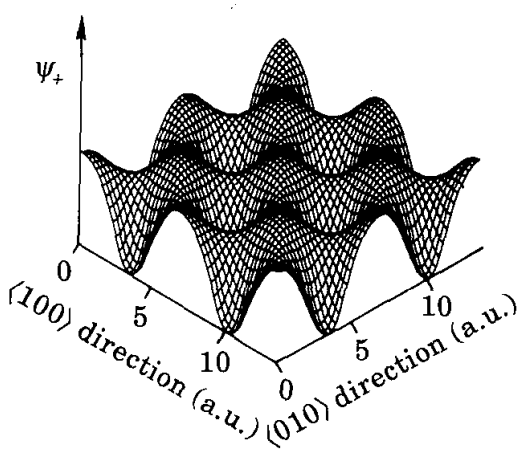

Figure 3.7 Positron wave function in fcc nickel (taken from [HC95]).

Electron Positron Correlations

The second important contribution discerning the TPMD and EMD are the electron-positron correlations know as enhancement. Similar to electron-electron correlations, the positron will interact with the surrounding electrons by polarizing the electronic medium. Even if the positron density is assumed to be low, the probability to find an electron close to the positron is increased due to the attractive Coulomb interaction. As electrons close to the FS are generally more mobile, they will be predominantly influenced. Figure 3.8 illustrates the effect of electron-electron and electron-positron correlations on the electron occupancy.

If electron-positron enhancement is neglected ($\gamma = 1$), the calculation is described as being in the independent particle model (IPM). Kahana was the first one to treat this problem on the basis of a non-interacting electron gas, as the IPM did not give a satisfactory description of the annihilation problem [Kah63]. Nowadays various implementations of enhancement models, largely based on quantum Monte Carlo simulations exist [MS79, BanN86, JS87, DLRNP11]. A good overview on the different approximations can be found in [LHAD10]. However, the exact treatment of the electron-positron correlations in dynamical mean field theory (DMFT) is still a challenge.

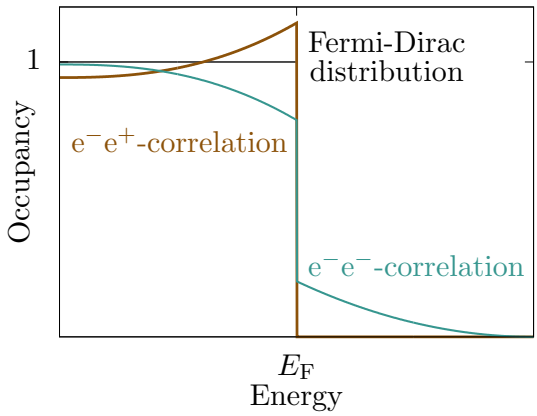

Figure 3.8 Deviations from the Fermi-Dirac distribution ($T = 0\,\mathrm{K}$) for electron-electron (blue) and electron-positron correlations (brown).

Chapter 4

Methods

This chapter covers the two experimental techniques used in this thesis, namely 2D-ACAR and high-resolution x-ray Compton scattering, both of which are sensitive to the bulk electronic structure of crystals in momentum space. The electronic structure is analyzed either by Compton scattering, i. e. through the inelastic scattering of photons from electrons, or by 2D-ACAR based on the annihilation process of electrons and positrons. Here, the theories behind the two techniques are covered and a short overview on existing literature applying those techniques is given. Furthermore, the details on the used experimental setups are given and the important steps of the data analysis for both techniques are described.

4.1 2D-ACAR

After the prediction of the positron in 1920s [Dir28] and its discovery in 1930s [And33] the focus was first put on understanding the fundamentals of the annihilation process itself. In 1942, finally, Beringer and Montgomery could measure the annihilation radiation with high enough precision to conclude that a positron and an electron annihilate into a pair of gamma quanta which are emitted with a deviation of less than 15 arcminutes from anti-collinearity [BM42]. They attributed this small deviation to either scattering of the annihilation radiation or the initial momentum of the electron-positron pair.

After this first period of positron experiments, scientist began to use the annihilation process for the investigation of solids. At the end of the 1940s the first DBS experiment proofed that positrons thermalize before annihilation and preferably annihilate with conduction electrons due to repulsion from the positively charged atomic core [DLW49]. In 1950 finally the history of ACAR starts.

This section will first give a short overview on the history of ACAR spectroscopy, before explaining its details and introducing the 2D-ACAR spectrometer in our research group at the Technische Universität München. At the end of this section the principles of the data treatment process will be introduced.

4.1.1 History of 2D-ACAR

In 1950 DeBenedetti et al. [DCKP50] used a so-called linear-slit geometry (see Fig. 4.1 (a)) and thus one-dimensional angular correlation of electron positron annihilation radiation (1D-ACAR) spectroscopy to confirm the findings of Dumond et al. [DLW49] but with higher resolution. For more than twenty-five years ACAR experiments were almost exclusively performed in this geometry besides a very few exceptions [CFT63, FS66] using the so-called point-slit geometry, shown in figure 4.1(b). However, even if the information content on the TPMD is higher in the point-slit geometry in contrast to the long-slit geometry and the achieved angular resolution was remarkably good, its application was limited due to low counting rates.

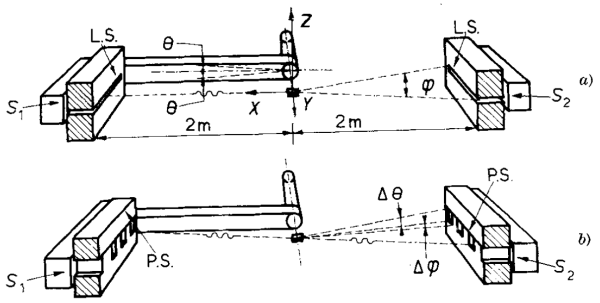

Figure 4.1 Schematics of ACAR spectroscopy in the (a) linear-slit and (b) point-slit geometry (taken from [CFT63]).

In contrast, 1D-ACAR in the long-slit geometry was used to investigate numerous simple crystalline materials. One of the most investigated materials is Cu due to the simple electronic structure [BP58, Mij69, CEB70]. Other metals investigated with 1D-ACAR are Al [BP58, SE68], Be and Mg [Ber62], the alkali metals Li and Na [DS67b, DS67a] and the rear earths Y, Gd, Tb, Dy, Ho, and Er [WM68]. Furthermore the semi-conductors Si and Ge were measured [EM66, SE68] and the application of 1D-ACAR was extended to alloys like V_3Si [BW70] and an equiatomic alloy of Ho and Er [WM68]. Towards the end of the 1960s the parity violation in the weak interaction found by [LY56]

was exploited by first spin-polarized measurements on Gd [HWB68], Fe [MH71] and Ni [BM71].

In 1977 Berko et al. performed the first 2D-ACAR experiment, using the multicounter detectors they developed two years earlier [BM75, BHM77]. In the following years the detector systems were further developed with the first measurements using proportional chamber [MFPJ78] and Anger cameras [WMW81]. Still today Anger cameras are state of the art systems for the gamma detection in 2D-ACAR. Since that, 2D-ACAR was used to investigate a wide range of material classes, from elemental crystals like Cu [e. g. KKN$^+$93, NCT$^+$01], Ni [SMW88, KKN$^+$91, DFH$^+$98], Mo [DFH$^+$98] and Va [WBA$^+$17], as well as spin-polarized measurements were performed on the ferromagnets Co [KKN$^+$92], Ni [GMWP91, CWB$^+$16], on more complex systems like Heusler alloys [WBB$^+$15], heavy fermion systems [RB05] or superconductors [SLB$^+$88, MDW$^+$04]. One of the most important applications of 2D-ACAR was the proof of the existence of half-metallicity first suggested by de Groot et al. [dGMEB83]. In two works Hanssen et al. [HM86, HMRB90] could proof that half-metals exist by determining the electronic structure of NiMnSb.

The aim of this section was to give a flavor on the wide range of applications of ACAR spectroscopy. Detailed reviews on 1D-ACAR (e. g. [BM75]) and 2D-ACAR measurements can be found elsewhere [Dug14, Cee15].

4.1.2 Fundamentals of 2D-ACAR

In chapter 3.3.5 the basic process of the annihilation of an electron-positron pair was introduced. The two-dimensional angular correlation of electron positron annihilation radiation (2D-ACAR) technique measures the angular deviation of the annihilation quanta to gain information on the transverse component of the electron momentum. Figure 4.2 shows the principally setup of a 2D-ACAR experiment. The angular deviation is measured by two spatially resolving detectors which are positioned along a common line of sight (z-axis) at distances l_1 and l_2 from a sample position at the origin of the coordinate system. By measuring the positions of the two annihilation photons $\begin{pmatrix} x_1 \\ y_1 \end{pmatrix}$ and

$\begin{pmatrix} x_2 \\ y_2 \end{pmatrix}$ the angular deviation relative to the x- and y-axes can be determined:

$$\begin{aligned} \theta_x &= \arctan\frac{x_1}{l_1} - \arctan\frac{x_2}{l_2} \approx \frac{x_1 l_2 - x_2 l_1}{l_1 l_2} \\ \theta_y &= \arctan\frac{y_1}{l_1} + \arctan\frac{y_2}{l_2} \approx \frac{y_1 l_2 + y_2 l_1}{l_1 l_2} \end{aligned} \tag{4.1}$$

The image of one detector has to be flipped vertically, as the two detectors face each other. This leads to the minus sign in the first line of equation 4.1. By using equation 3.32 we can directly get the momentum components p_x and p_y:

$$\begin{aligned} p_x &= \theta_x \cdot m_\mathrm{e} c \\ p_y &= \theta_y \cdot m_\mathrm{e} c \end{aligned} \tag{4.2}$$

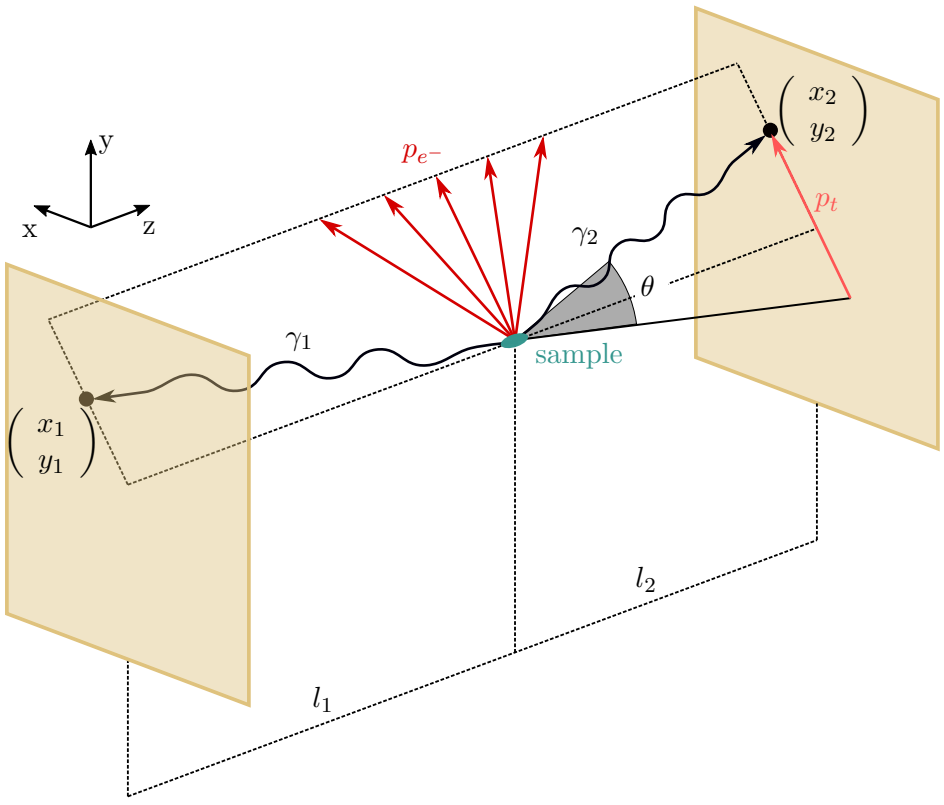

Figure 4.2 Schematics of a 2D-ACAR spectrometer. Two spatially resolving detectors are placed at distances l_1 and l_2 on a common line of sight around a sample. The coincident measurement of both annihilation photons allows the determination of the transverse component of the electron momentum. However, it is not possible to distinguish between electrons with different longitudinal momenta, as the energy of the photons is not resolved by the detectors.

Usually scintillation detectors are used in ACAR experiments and the longitudinal momentum component of the electron cannot be resolved. Therefore, all electrons carrying the same transverse momentum lead to the identical angular deviation and the result of a 2D-ACAR experiment ρ^{2D}_{ACAR} is the projection of $\rho^{2\gamma}$ along the detector-detector axis

$$\rho^{\mathrm{2D}}_{\mathrm{ACAR}}(p_x, p_y) = \int \rho^{2\gamma}(\mathbf{p})\mathrm{d}p_z * R(p_x, p_y). \tag{4.3}$$

The experimental resolution function $R(p_x, p_y)$ takes into account the finite spatial resolution of the detectors as well as the annihilation spot size and the smearing due to the thermal motion of the positrons.

4.1.3 Experimental Setup at Technische Universität München

In this chapter a concise overview of the 2D-ACAR spectrometer at the Technische Universität München (TUM) is given. A detailed description of the mechanical and physical setup can be found in the PhD thesis of H. Ceeh [Cee15], while the signal processing is extensively explained in the PhD thesis of J.A. Weber [Web17].

Figure 4.3(a) shows a true-to-the-scale sketch of the TUM spectrometer. The source-sample stage is positioned between two position sensitive detectors. In contrast to any other ACAR setup [WMW81, HCK$^+$95, Kru99] the detectors and samples are approximately 2 m above ground level to improve the usage of the available space in the experimental hall. The γ-quanta created by annihilation events in the sample can leave the source-sample chamber through bores in the lead shielding and are detected by the Anger camera type detectors.

Source-Sample Stage

This section gives an overview of the source-sample stage as used during the majority of this work. Some recently implemented upgrades to the stage will be introduced in the subsequent section.

Figure 4.3(b) shows a sectional view of the source-sample stage and figure 4.3(c) additionally magnifies the center. The ^{22}Na is sealed in a standard source capsule [KRBBvdW01], which is embedded in a W_8Cu_2 rod serving as a first radiation shield. The source manipulator is used to move the source capsule vertically from the measurement position (lowest position) into the

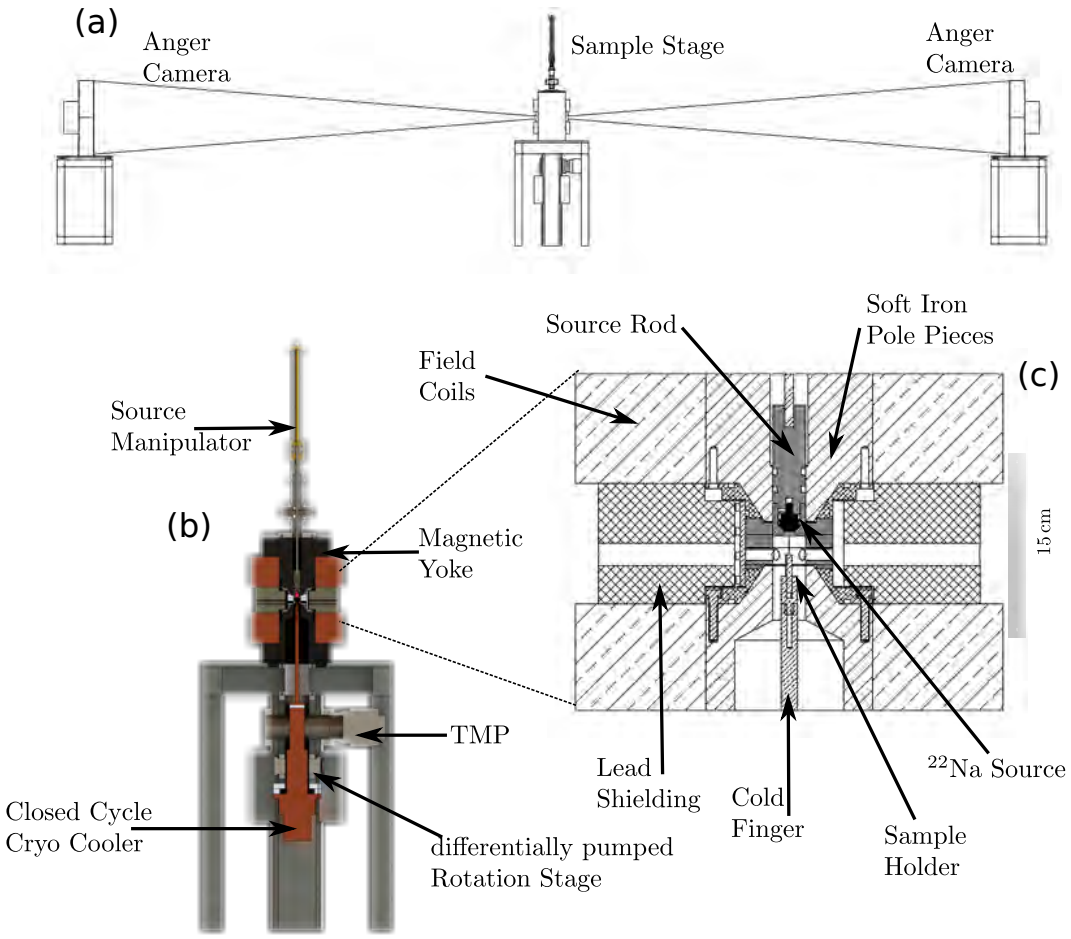

Figure 4.3 a) Schematics of the 2D-ACAR spectrometer at TUM with the source-sample stage position between the Anger cameras. The baseline of the detectors is 17.5 m. (b) Cut view of the source-´sample stage. (c) Magnified view of the sample environment including the magnetic field coils and pole pieces. Sample and source are positioned symmetrically with respect to the pole pieces [figures take from Cee15].

lead shielding (top position) and reverse. When the source is inside the lead shielding an additional shutter can be closed to further protect the researcher from radiation during sample change. Around the source-sample chamber, a commercially available water cooled electromagnet is positioned. The pole pieces of the magnet are designed to produce a homogeneous magnetic field to reduce positron reflection in strong field gradients. By applying a magnetic field of 1.0 T the positrons can be focused to a Gaussian shaped spot with FWHM of (3.8 ± 0.4) mm.

Opposite the source, the sample holder is positioned onto one of two exchangeable sample holders. The first sample holder is constructed for temperatures from 300 to 650 K, while the second one can be used from room temperature down to 10 K. The high temperature sample holder consists of a simple 8 Ω coaxial heating wire wrapped around a heating support directly below the sample and a long aluminum rod positioning the sample at the correct height of 20 mm below the source. This distance is a compromise between positron transport efficiency and reduction of background radiation.

The low temperatures of the second sample holder are achieved by a Sumitomo RDK-415D closed cycle cryostat, which can reach temperatures down to 4.7 K in the second stage. The thermal contact between second stage and sample is realized by a copper cold finger fixed at the top of the second stage. By heat introduction along the 22 cm long cold finger the minimum sample temperature is raised to approximately 15 K. Higher temperatures up to approximately 300 K[1] can be attained with resistive cartridge heaters connected to a PID-controller.

For the measurement, one of the sample holder arrangements is connected to a differentially pumped, rotary flange with a angular resolution of 0.1°. This allows the change of the projection direction without breaking vacuum or stopping the cryostat pump. The vacuum is needed to avoid absorption of positrons in air and suppress thermal flux between the walls of the sample chamber and the sample. Therefore, a scroll pump and an additional turbomolecular pump are connected to the sample environment, which allow pressures down to 1×10^{-8} mbar.

[1] higher temperatures may destroy the cryostat

Upgrade of the Source-Sample Stage

In a recent upgrade of the 2D-ACAR setup at TUM, the source-sample stage was further optimized. As explained in the last section, a differential pumped, rotary flange was used to change the projection direction in the old configuration. Since, the rotator was far from the sample position (see figure 4.3b) a small deviation between the axis of the rotation flange and the correct rotation axis in the center of the experimental setup can lead to large deviations at the sample position.

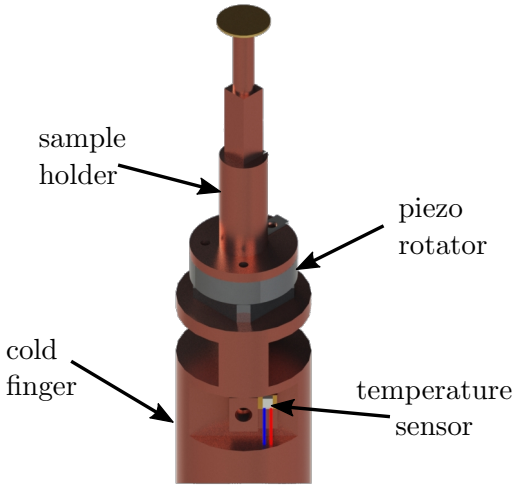

Figure 4.4 CAD model of the upgraded sample holder. The sample can be rotated with a piezo rotator, positioned just a few centimeters below the sample itself. A temperature sensor is also connected close to the sample.

Figure 4.4 shows the uppermost part of the new sample holder. In the upgrade the rotation flange is replaced by an Attocube ANR51/LT/HV 360° endless piezo rotator which is mounted directly below the sample holder. The rotator can be operated in a temperature range of 1 to 373 K, in magnetic fields up to 35 T and pressures down to 1×10^{-8} mbar. Its fine position resolution is in the µ° range and it can take loads up to 30 g. Due to the removal of the rotatory flange, the length of the cold finger could be reduced by approximately 7 cm which leads to less temperature rise along the cold finger in contrast to the older version. According to simulations by C. Oswald [Osw21] sample temperatures down to 10 K seem feasible. This, however, would require the additional introduction of a heat shield along the cold finger. First test measurements have shown temperatures in the 15 K range, which is comparable to the old setup. A reason why there is no direct effect of the shorter cold finger visible,

might lie in a lower heat transmission over the piezo ceramics itself in contrast to the old copper sample holder which was directly mounted on the cold finger. The temperature is measured close to the sample position by a radiation robust Cernox^{TM} 1070 sensor which was purchased from Quantum Design GmbH. The sensor is calibrated in a temperature range of 4 to 325 K with a typical precision of ±6 mK at 10 K and ±40 mK at 300 K.

Anger Camera Detector System

Anger cameras consist of a large scale scintillation crystal which converts γ-rays into (visible) light. This light is detected by a photo multiplier tube (PMT) matrix mounted onto a glass plate connected with the crystal. Analog electronic circuits evaluate the PMT response. The position of the absorbed γ quantum is then reconstructed by nonlinear amplification and determination of the center of gravity of the collected light. This simple principle was developed by H.O. Anger in 1958 [Ang58].

The two Anger cameras of the 2D-ACAR spectrometer at TUM were designed and built by the company Scintronix presumably between 1987 and 1990 and bought from the positron group of Stephen Dugdale and Ashraf Alam at the University of Bristol. The photopeak efficiencies at 511 keV of the two detectors are $(7.4 \pm 0.1)\,\%$ and $(6.6 \pm 0.1)\,\%$, respectively [CWL$^+$13]. Each detector consists of a 10.5 mm thick NaI:Tl scintillator crystal mounted in front of a matrix of 61 PMTs arranged in a hexagonal pattern. Every PMT has a diameter of 63.5 mm and is surrounded by six other multipliers with a spacing of 7 mm. A lead ring with a diameter of 419.1 mm restricts the field of view of the detectors to their central region in order to reduce boundary effects.

The detectors and sample chamber were positioned by using a laser positioning system and theodolite in order to guarantee firstly, the collinearity of the detector centers and the sample and secondly that both detectors are parallel to the front side of the sample chamber. To protect the NaI crystals from rapid temperature changes each detector is encased in a transparent plastic housing and additionally in a removable styrofoam box. Figure 4.5 shows a front (a) and back (b) view of the Anger cameras.

One commonly known problem inherent to Anger cameras are spatial distortions. Assuming the naive approach of calculating the position of an event as the weighted sum of the PMT responses, this is clear as the signal created by a single PMT varies nonlinearly with the distance between the positions of the

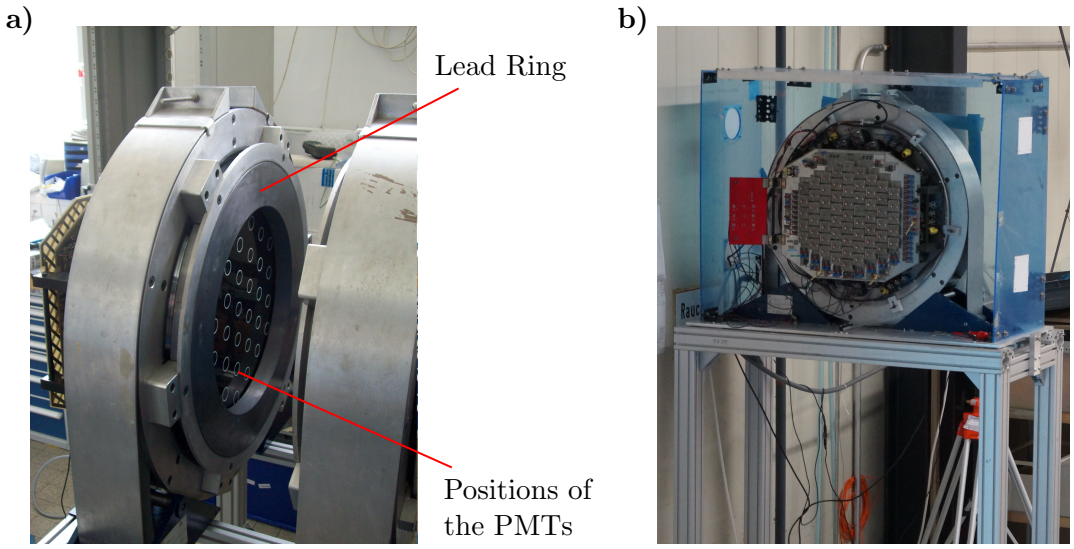

Figure 4.5 a) Front side of a Anger camera. The positions of the PMTs is marked on the front cover with white circles. The lead ring reduces boundary effects. **b)** Back view of a Anger camera inside the (opened) plastic housing.

event and the PMT. A commonly used approach to solve this problem is the use of weighting factors which depend nonlinear on the PMT signal [Sho84]. An algorithm developed by Leitner et al. [LCW12] solves this problem by using a reference measurement performed on a regular spatial pattern from which a look-up table is created, mapping back all measured positions on the Anger cameras to their expected positions. Every time, settings of the Anger cameras have been changed, a new calibration measurement should be performed and a new look-up table should be calculated.

4.1.4 ACAR Data Analysis

For every measurement, three files are generated by the signal processing unit of the experiment. The signal processing part itself is comprehensively discussed in the thesis of J.A. Weber [Web17] and not further explained here. Our starting point are the three binary list mode data files containing the experimental data. For each detector the single events are stored in a separate file. Since significantly more single events are registered in comparison to coincident counts, only every 20^{st} single event is saved in the list. The single events are saved with a 64 bit time-stamp from the ADC clock followed by two 32 bit number corresponding to the actual x and y positions on the detector and a 32 bit numbers corresponding to the energy of the event (z signal). The

last file collects the coincident events stored in the form of six 32 bit numbers corresponding to the actual x and y position and the energy of detector one as well as the actual x and y position and the energy of detector two. The form of these data allows to determine the energy windows for the 511 keV photo peak in the offline analysis.

The process to retrieve the final ACAR spectrum from the raw data is shown in the flow chart of figure 4.6. First the single as well as the coincident data are filtered by energy windows to only use the true 511 keV events. The spatial distortion correction, developed by Leitner et al. [LCW12] is applied, yielding an undistorted data distribution. Afterwards the distortion corrected list mode data are moved in order to center the final spectrum without interpolation. That means that constant shifts Δx and Δy are added to the data stream of either detector one or detector two. It is important to apply this step to the single data as well as to the coincidence data. As at the beginning the correct shifts are not known, they are set to zero in the first iteration. Now the data can be histogrammed, which is straight forward for the single events. To calculate the histogram of the coincident data equations 4.1 are applied, which leads to a spectrum that is twice the size of the single spectra. Now the momentum sampling function (MSF) (details see below) is calculated from the single spectra and the coincidence data is divided by the MSF to finally arrive at the 2D-ACAR spectrum. From this spectrum, the shifts Δx and Δy can be determined and the corresponding steps can be repeated until the 2D-ACAR spectrum is perfectly centered.

Momentum Sampling Function

The MSF describes the (inhomogeneous) detection efficiency of the momenta in the ACAR spectrum. The 2D-MSF is given by the convolution of the detection efficiencies ϵ_1 and ϵ_2 of detector one and detector 2, respectively:

$$MSF(\theta_x, \theta_y) = \int\int \epsilon_1(\theta_x - \theta'_x, \theta_y - \theta'_y) \cdot \epsilon_1(\theta'_x, \theta'_y)\, \mathrm{d}\theta'_x\, \mathrm{d}\theta'_y. \tag{4.4}$$

The detection efficiency is determined by two factors. The first one is the limited field of view of the detectors. If we consider a symmetric setup and an angular deviation of $\theta = 0°$ between the two annihilation photons, the second photon will always hit the active detector area if the first photon is detected. For all larger angles this is not the case and the MSF decreases. The

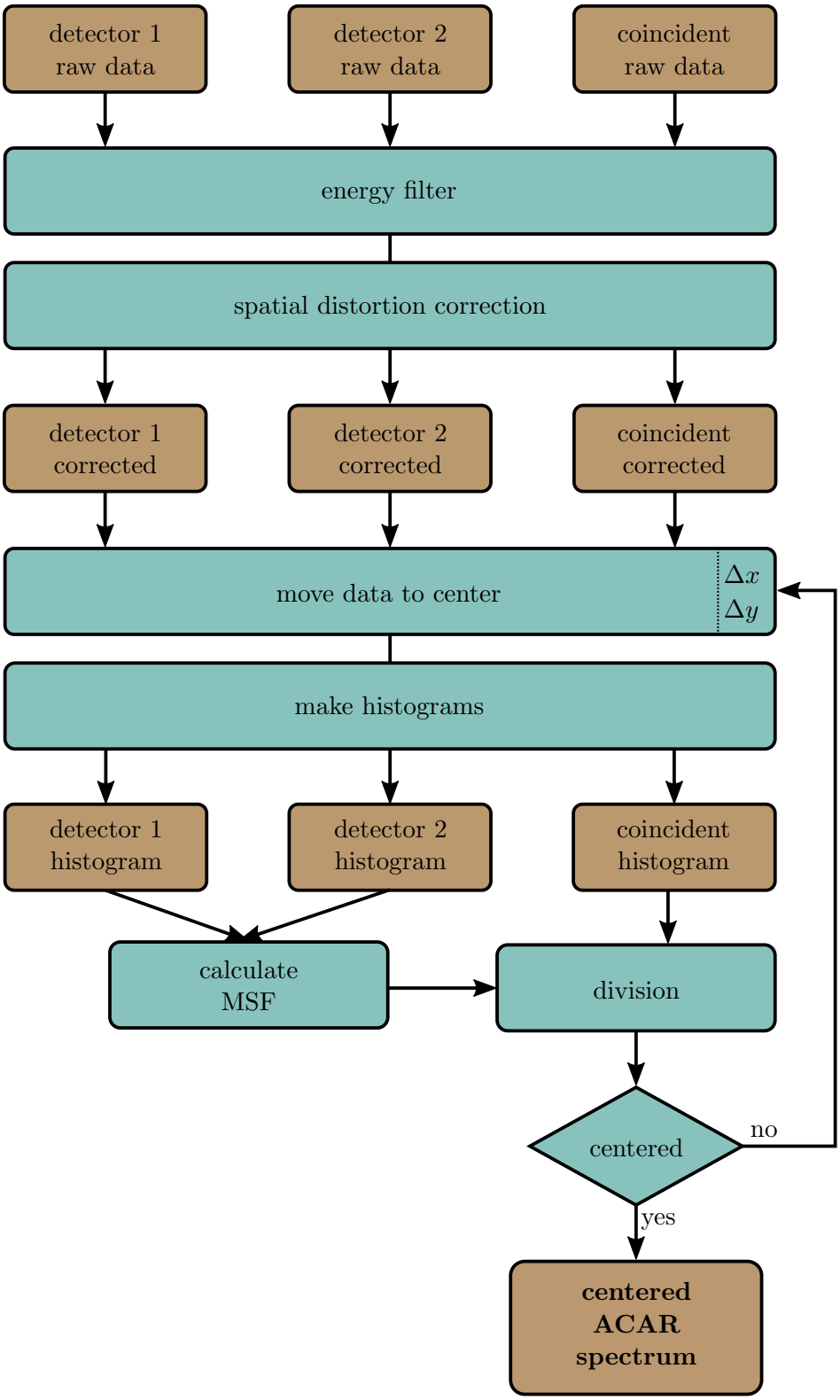

Figure 4.6 Flowchart depicting the data analysis process from raw data to a centered ACAR spectrum. Files are shown by brown boxes, while method boxes are colored blue.

second important factor is the varying detection efficiency within the active area. This can be influence either by differing sensitivity of the 61 PMTs or by inhomogeneous illumination of a detector, e. g. due to photon absorption in the sample.

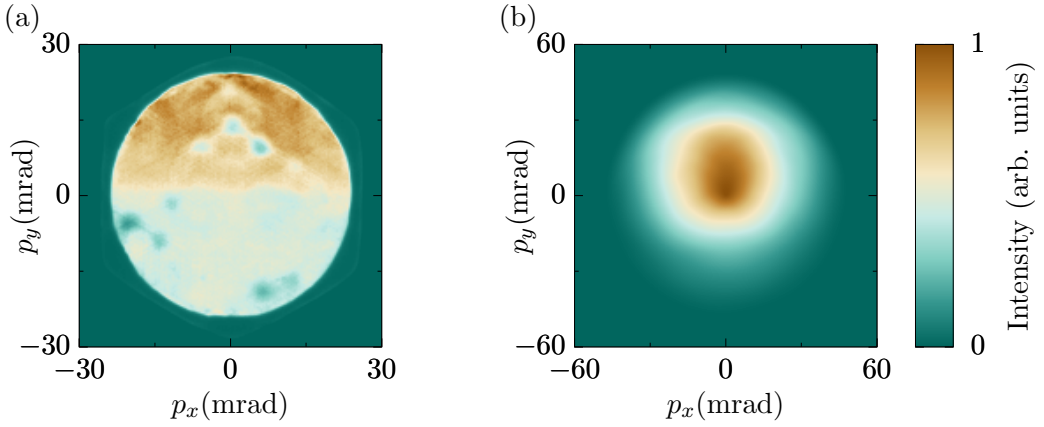

Figure 4.7 (a) Highly inhomogeneous intensity distribution on one of the detectors from a measurement of tungsten. (b) MSF of the corresponding measurement.

Figure 4.7(a) shows an extreme example of a very inhomogeneous single detector image. The lower half of the detector registers much less counts due to strong photon absorption in the tungsten sample. Furthermore, we can see that the efficiency of the different PMTs varies significantly. The second effect can be reduced by readjusting the electronics. The resulting MSF from such a distribution is shown in figure 4.7(b). Due to the strong γ-absorption in tungsten the MSF is much more pronounced in the upper half of the momentum space.

Radial Anisotropy

In general, the positron annihilation probes all electrons (weighted by the annihilation probability) in the system. Electrons close to the core give a nearly isotropic distribution, which is superimposed by an anisotropic contribution mainly produced by the electrons near the FS. Therefore, one of the most important concepts in the analysis of 2D-ACAR is the calculation of the radial anisotropy ρ_{aniso}. Mathematically, the radial anisotropy ρ_{aniso} is calculated from the ACAR spectrum ρ^{2D}_{ACAR} by subtracting the isotropic contribution $\bar{\rho}_{\mathrm{ACAR}}$:

$$\rho_{\mathrm{aniso}}(p_x, p_y) = \rho^{\mathrm{2D}}_{\mathrm{ACAR}}(p_x, p_y) - \bar{\rho}_{\mathrm{ACAR}}(p_x, p_y) \tag{4.5}$$

where the isotropic part is the radial average $\bar{\rho}_{\mathrm{ACAR}}(p_x, p_y) = \bar{\rho}_{\mathrm{ACAR}}\left(\sqrt{p_x^2 + p_y^2}\right)$, which averages $\rho^{\mathrm{2D}}_{\mathrm{ACAR}}(p_x, p_y)$ over all data points in equidistant intervals $[p_r; p_r + \Delta p_r[$.

J. Weber developed a fast algorithm to calculate the radial anisotropy [Web17]. It uses rings around the center to determine the isotropic contribution and decides for every pixel in the spectrum to which ring it belongs. This leads to some problems especially at very small momenta close to zero, as quadratic pixels do not map to circles very well. For example the anisotropy in the center might not be exactly zero. This is not a big problem for many applications like the centering of the spectra.

However, in order to yield higher quality calculations of the radial anisotropy a new algorithm was implemented in this thesis. It is a multistep process. First, the original spectrum ρ_0 is averaged with a 180° rotated ρ_0 spectrum which gives ρ_1. This new spectrum ρ_1 is again averaged with the 90° rotated spectrum ρ_1 leading to the spectrum ρ_2 and so on. After, e. g., twelve iterations the rotation angle is as low as $\frac{360^\circ}{2^{12}} \approx 0.88^\circ$ and in a typical spectrum of 512×512 pixels even the pixels which have maximum distance from the center are rotated by less than one pixel. In contrast to the former implementation this algorithm is significantly slower but gives better results over the full momentum range.

One of the most common applications of the radial anisotropy is the qualitative comparison between different measurements or several theoretical calculations. Furthermore it enables conclusions about the crystal quality. In case of crystals with high defect density or polycrystalline samples, the radial anisotropy will only show experimental noise. Therefore, checking the radial anisotropy for the expected symmetries of the measured crystal direction is always the first step in the experimental data analysis.

4.2 Compton Scattering

The Compton effect, first discovered by Arthur H. Compton in 1923 [Com23], describes the inelastical scattering of a photon by an electron. By considering light as particles, this inelastical scattering process leads to a shift in the wavelength of the outgoing photons, which was deduced by Compton who applied conservation of energy and momentum in this two-particle process. This effect was a very strong argument that the description of light as a wave phenomenon is not the only possibility. Two years later Dirac was the first one to link a broadened x-ray emission line to the motion of hot electrons in stellar atmosphere [Dir25]. However, the most important contribution in the early theory of Compton scattering was made by DuMond [DuM29], who was the first one to recognize the importance of the motion of the target electron in producing a Doppler shift of the Compton-scattered photon. In this paper DuMond provided the first experimental evidence for Fermi-Dirac statistics, as he showed that the Compton profiles from scattering in beryllium are much broader than expected from pure Maxwell-Boltzmann statistics. Therefore, having access to the EMD is one of the most important applications of Compton scattering in condensed matter physics and laid the foundation for modern Compton scattering experiments.

In this chapter, the Compton scattering will be explained in detail. First, a short history of the application of Compton scattering experiments in condensed matter physics will be given before the theoretical principles are explained. The third part will show the details of the high resolution Compton spectrometer located at the synchrotron SPring-8 in Japan. Finally, the reader will be taken through the relatively complex Compton data analysis process.

4.2.1 A Brief History of Compton Scattering

After the first condensed matter Compton experiment of DuMond in 1929 [DuM29], hardly any experimental advances had been made during the subsequent three decades. In the year 1965, Compton scattering experiments got restarted by measurements on lithium [CLW65], even if the results did not show big progress compared to the experiments more than thirty years before. The experiments at that time suffered from low fluxes and comparably low x-ray energies and thus a strong dominance of photoelectric absorption. With the advance of high-power rotating anode x-ray sources in the 1970s the momentum

resolution could be increased and many experiments were conducted. However, due to the low x-ray energies, the samples were limited to light elements like gaseous and liquid He and H_2 [Eis70], and gaseous N_2, Ne and O_2 [Eis72] or Be [CLC+82].

The next big step was the first γ-ray Compton scattering experiment [Coo79]. By sacrificing resolution and flux but strongly increasing the photon energies above 50 keV, it became possible to investigate heavier elements. Some examples are Si, Ge and Diamond [RE72] or Lu and $LuH_{2.05}$ [LLGP79].

The most recent era of Compton scattering started around 1985 with the availability of high energy synchrotron radiation. With the advance of synchrotrons the photon flux at high energies increased significantly while momentum resolution could be further improved. This opened up completely new fields of studies like the investigation of electron systems as functions of temperature, composition or orientation. Nowadays, synchrotron based Compton scattering is a well established technique in condensed matter physics and is used in various material classes like elemental crystals [DDG+98, BPA+13], alloys [RML+20], magnetic compounds [DDM+00, DIS+01, MDW+04, DAV+11, MOO+12, BEM+15] or superconductors [SIB+11].

4.2.2 Compton Scattering Cross Section

Scattering from a Free Stationary Electron

The following two sections are based on [Coo85] and [CMS+04, chap. 2]. In general Compton scattering is the term used for the inelastic scattering of a photon with an electron. In figure 4.8 the scattering interaction is depicted and the terminology for the following calculations is introduced. In this section the non-relativistic Compton cross-section is deduced, since the relativistic derivation is much more complicated and the main points can be seen from the non-relativistic case. The whole relativistic deduction can be found in [Hol88] and some results are used in the data treatment (section 4.2.4).

The well known formula for the shift of the wavelength of the photon $\Delta\lambda = \lambda_2 - \lambda_1 = \frac{h}{mc}(1 - \cos\varphi)$ can be written in terms of energy ($\lambda = \frac{2\pi c}{\omega}$) as follows:

$$\omega_2 = \omega_1 \left[1 + \frac{\hbar\omega_1}{mc^2}(1 - \cos\varphi)\right]^{-1}. \tag{4.6}$$

From this formula we can see that the energy shift of the outgoing photon with

respect to the incoming photon increases with increasing ω_1 and is monotonically decreasing for increasing scattering angles φ. But even if the Compton shift formula is an important verification of quantum principles and relativistic kinematics, it does not give any information about the scattering target. Also the quantum electrodynamic derivation of the scattering cross section by Klein and Nishina (equation (4.7)) only considers scattering of unpolarised photons by free electrons [JR76]

$$\left(\frac{d\sigma}{d\Omega}\right)_{K-N} = \frac{1}{2}\left(\frac{e^2}{mc^2}\right)^2 \left(\frac{\omega_2}{\omega_1}\right)^2 \left(\frac{\omega_2}{\omega_1} + \frac{\omega_1}{\omega_2} - \sin^2\varphi\right). \tag{4.7}$$

So far all formulas consider free and stationary electrons. The main question at this point is the influence of bound electrons carrying a momentum.

Impulse Approximation and Compton Profiles

In the 1920s, Jauncey [Jau25] and DuMond [DuM29] calculated the Compton spectra for moving electrons and found a Doppler broadening of the Compton scattered beam. In fact, the results of DuMond where in good agreement with first experiments on Beryllium since he used the, at that time new, Fermi-Dirac distribution in his calculations. Remarkably is to say that both used scattering from free electrons in their calculations. If this assumption should still be valid for electrons in a material the interaction between photon and electron has to be impulsive. That means that the surrounding electrons do not participate in the interaction and the time of the scattering event is extremely short. Hence, the potential the target electron sees immediately before and after the interaction is constant and cancels out on both sides of the energy conservation law. To obtain the validity of the impulse approximation the energy transfer to the recoil electron has to be much higher than its binding energy. For the example of the BL08W beamline at SPring-8 the energy transfer is approximately 35 keV, i. e. large compared to typical binding energies of the interesting outer electrons in a solid of several eV; thus the impulse approximation is in most cases fulfilled.

To deduce a (classical) formula describing the Compton profile we start with the conservation equations, assuming that the potential energy terms cancel

out:

$$\text{Momentum:} \quad \hbar\boldsymbol{k}_1 - \hbar\boldsymbol{k}_2 = \boldsymbol{p}_2 - \boldsymbol{p}_1 \tag{4.8}$$

$$\text{Energy:} \quad \hbar\boldsymbol{\omega_1} - \hbar\boldsymbol{\omega_2} = \frac{1}{2m}\left(p_2^2 - p_2^2\right) \tag{4.9}$$

By getting an expression for $\boldsymbol{p}_2$ from equation 4.8, plugging it into equation 4.9 and using the scattering vector $\boldsymbol{K} = \boldsymbol{k}_1 - \boldsymbol{k}_2$ we get the energy transfer as

$$\hbar(\omega_1 - \omega_2) = \frac{1}{2}m\left[\boldsymbol{p} + \hbar\left(\boldsymbol{k}_1 - \boldsymbol{k}_2\right)\right]^2 - \frac{p^2}{2m} = \frac{\hbar^2|\boldsymbol{K}|^2}{2m} + \frac{\hbar\boldsymbol{K}\cdot\boldsymbol{p}}{m}, \tag{4.10}$$

where the index of $\boldsymbol{p}_1$ is dropped as the recoil electron does not play any role in the following discussion. The $|\boldsymbol{K}|^2$ term in equation (4.10) gives the energy shift equal to equation (4.6). If we choose the z-axis of a Cartesian coordinate system along $\boldsymbol{K}$ we can see that the second term is linearly dependent on the p_z component of the electron's ground-state momentum and this momentum creates a Doppler shifted Compton signal. Thus, the measured Compton profile $J\left\langle p_z|p_z\right\rangle$ for target electrons with a ground-state EMD $n\left\langle\boldsymbol{p}|\boldsymbol{p}\right\rangle$, is the projection of $n\left\langle\boldsymbol{p}|\boldsymbol{p}\right\rangle$ along $\boldsymbol{K}$:

$$J\left(p_z\right) = \int_{p_x}\int_{p_y} n\left(p_x, p_y, p_z\right)\,\mathrm{d}p_x\mathrm{d}p_y. \tag{4.11}$$

To get a feeling which dimension the Doppler shift will have we can evaluate the second term in equation (4.10) for the case $\omega_1 \ll \frac{mc^2}{\hbar}$. Using this condition we can assume $\omega_1 \approx \omega_2$ and additionally use the cosine law $K = |\boldsymbol{k}_1 - \boldsymbol{k}_2| = \sqrt{k_1^2 + k_2^2 - 2k_1k_2\cos\varphi}$ to obtain:

$$\begin{aligned}\hbar\Delta\omega &= \frac{\hbar\boldsymbol{K}\cdot\boldsymbol{p}}{m} = \frac{\hbar K p_z}{m} = \frac{\hbar p_z}{mc}\sqrt{\omega_1^2 + \omega_2^2 + 2\omega_1\omega_2\cos\varphi} \\ &= \frac{2\omega_1}{mc}\sqrt{4\omega_1^2\frac{1-\cos\varphi}{2}} = \frac{2\hbar\omega_1}{mc}\sin\left(\frac{\varphi}{2}\right)p_z.\end{aligned} \tag{4.12}$$

An electron at the Fermi surface of aluminium has a velocity of $\sim 2\times10^6\,\mathrm{m\,s^{-1}}$. This gives $\frac{\Delta\omega}{\omega_1} \sim \frac{1}{50}$ which could be easily resolved by experimental setups.

4.2.3 The BL08W Spectrometer at SPring-8

All measurements for this thesis have been conducted on the high resolution Compton scattering spectrometer at the beamline BL08W of the synchrotron SPring-8 in Japan [HIO+01]. This beamline is dedicated to high-energy inelastic scattering (Compton scattering) and uses an elliptical multipole wiggler with a periodicity of 12 cm and a total length of 4.5 m to create hard x-rays with energies up to 300 keV. The beamline serves two experimental stations: One for high-resolution Compton scattering and the second one for magnetic Compton scattering [Sak98]. In the following only the high resolution setup is considered.

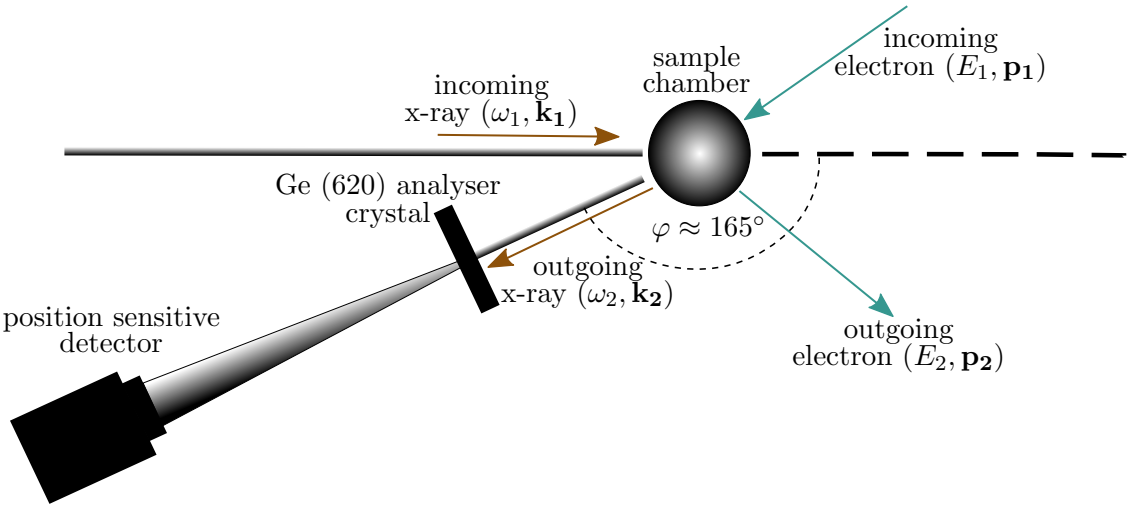

Figure 4.8 Schematic diagram of the high resolution Compton scattering setup at BL08W, showing the main hardware components [HIO+01] and the variables of the Compton scattering interaction. Index 1 is given to incoming and index 2 to outgoing particles. $\mathbf{k}_1$ and $\mathbf{k}_2$ are the wavevectors of the photons (brown), $\hbar\omega_1$ and $\hbar\omega_2$ their energies. The electron (blue) momenta and energies are denoted $\mathbf{p}_i$ and E_i and the scattering angle is φ.

Figure 4.8 shows a schematic diagram of the spectrometer. The setup corresponds to an energy dispersive Cauchois type spectrometer. The incoming x-rays are double bent monochromated by a Si(400) crystal to (115.61 ± 0.17) keV [Sak98]. This energy is chosen since it allows the optimization of the monochromator using the uranium K-edge absorption. After hitting the sample the photons scattered under an angle of $\approx 165°$ are focused onto the position sensitive detector (PSD) using the Ge(620) bent crystal analyser. The PSD is mounted on the so called Rowland circle which leads to a focussing of all photons of the same energy onto one well defined position.

The detector itself consists of an optical image intensifier mounted in front of

a charge-coupled device (CCD) camera. The image intensifier is composed of a 500 µm CsI screen which converts the x-rays into visible light going through optical lenses onto the CCD camera [SI04]. The detector covers the energy range of 70 to 90 keV and the overall momentum resolution of the spectrometer is ≈ 0.14 a.u..

4.2.4 Compton Data Analysis

A very demanding step in Compton scattering experiments is the data analysis. Several corrections have to be applied to the experimental data to get meaningful Compton profiles. The following section will introduce the most important ones in more detail. All corrections are presented in the order of their application to the data, except the saturation correction which is the first one to be applied but for the sake of clarity explained in the third subsection.

Distortion

Like mentioned in section 4.2.3 the PSD consists of an optical intensifier and a CCD camera. The lens of the optical intensifier creates distortion on the raw CCD image. The distortion is modeled by a pincushion function [PBL09].

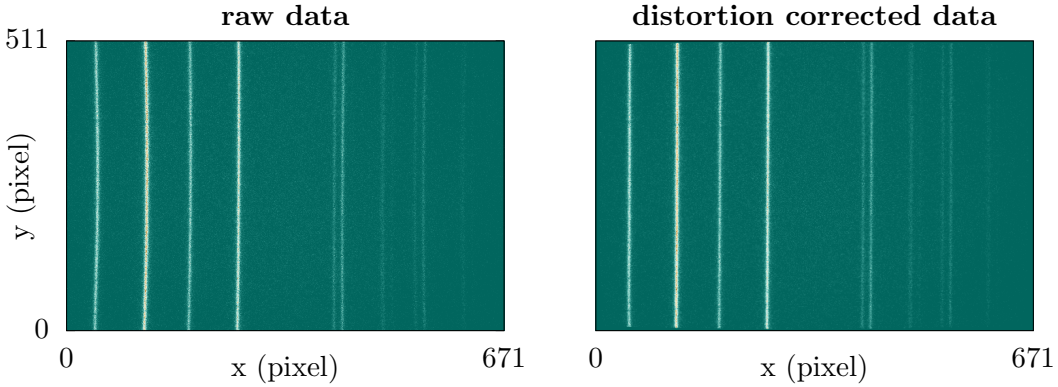

Figure 4.9 CCD image before (left) and after (right) the distortion correction

Figure 4.9 shows the raw CCD image on the left side and the distortion corrected image on the right side. The image displays the emission lines of a BiTl sample, which is used for the energy and efficiency calibration and further explained in the efficiency and energy calibration parts. Each "line" in the images originates from photons with a constant energy and should therefore be straight lines on the detector. Since the detector uses optical lenses to map the photons created on the CsI screen onto the CCD, the incoming straight lines

are distorted on the CCD. The left image shows clearly the pincushion type distortion.

The straight line condition can be used to obtain the correction values for the distortion center (x_c, x_c) and factor κ. Therefore, the sum of the vertical variance of the counts is minimized by iteratively changing the center and factor of the pincushion distortion. Having found the correct correction values the undistorted positions (x_u, x_u) are calculated from the distorted positions (x_d, y_d) by the mapping function

$$\begin{bmatrix} x_u \\ y_u \end{bmatrix} = \begin{bmatrix} x_d \\ y_d \end{bmatrix} \left[1 + \kappa R_D^2\right] \tag{4.13}$$

where $R_D = \sqrt{(x_d - x_c)^2 + (y_d - y_c)^2}$ is the distance of the pixel from the distortion center. Finally, instead of interpolating the measured intensities onto the new position grid, the measured counts are redistributed in the new pixels in order to preserve the measurement statistics.

Image Integration, Normalisation and Background Subtraction

After the distortion correction, the two-dimensional CCD images are vertically integrated along the y-direction (see figure 4.9) to obtain a one-dimensional energy dependent Compton profile in the channel scale. It should be stated here, that energy and channels are not connected linearly (see below). The 1D spectra are then normalized to the incoming beam monitor counts, which is proportional to the beam intensity and measurement time.

At the end of the experiment the background is measured by using a flat Ge (620) analyzer crystal instead of the bent one. Therefore, the scattered photons are not focused any more and only the background is registered at the detector. The background image is corrected for saturation and distortion, integrated vertically, normalized and fitted with a high order polynomial. The fitted background is then subtracted from every profile.

Saturation

In the Compton scattering experiment, the CCD is operating in the so called single photon detection mode. In this mode, the CCD is read very frequently and every pixel is checked if a photon was registered during the exposure or not. Since this is a binary information (photon or no photon), every pixel of

the camera can only register one photon at maximum per exposure. In the case that a second photon hits the same pixel during one exposure, it is not registered. Thus, pixels exposed to higher intensities saturate faster. The effect can be modeled with the following relationship

$$m = n \exp\{-\tau n\} \tag{4.14}$$

where m is the measured intensity per pixel and exposure, n the expected intensity per pixel and exposure and τ the so called saturation coefficient [BPA+13]. For an exposure time of 61 ms a saturation coefficient of $\tau = 1.214$ was determined for the x-ray intensifier camera at BL08W by Brancewicz et al. [BPA+13]. An exposure time of 61 ms corresponds to the standard operation mode of the detector in the Compton scattering experiment. The factor itself was determined by comparing measurements on an aluminum sample with a very short exposure time of 706 µs (to avoid saturation) and the standard exposure time.

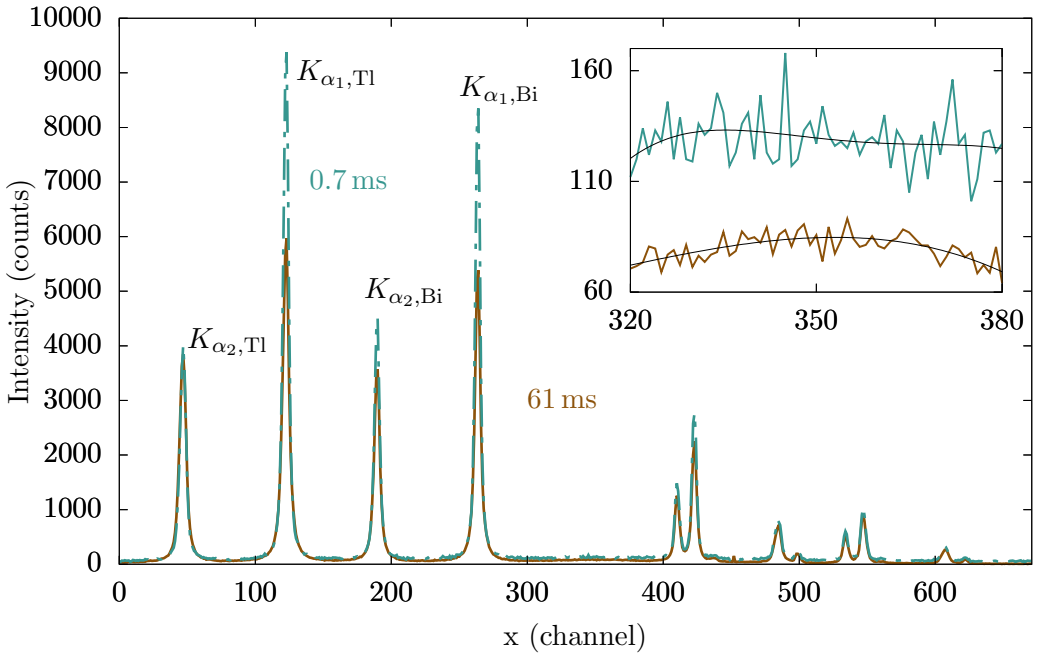

Figure 4.10 Spectra measured with an exposure time of 61 ms and 0.7 ms on a BiTl sample. Both spectra are normalised to the same total exposure time. The inset shows a zoom into the Compton region between channel 320 and 380. The black lines show polynomial fits and serve as a guide to the eye.

However, the comparison of two spectra of a BiTl sample taken with different exposure times of 61 ms and 0.7 ms reveals some problems. In figure 4.10 the

two spectra are normalised to the same total acquisition time (equal to the number of acquisitions multiplied by the exposure time). The high peaks show a clear saturation effect of the spectrum with the long exposure time (brown). This makes sense, since the CCD will saturate more if the exposure time is increased. Anyway, the inset, which shows a zoom into the Compton scattering region, still reveals a huge saturation effect of the same order of magnitude. As we can see from equation 4.14 the CCD should saturate more, the higher the count rate is. Furthermore, the fluorescence peaks show a strange behavior as well. The ratio of the two Tl Kα lines (two peaks on the left in figure 4.10) changes much more between the two exposure times than the ratios between the two Bi Kα lines (peak three and four from the left) of the two spectra. Since the number of counts is very similar for both pairs of Kα lines, also the ratio should be very similar.

One possible explanation of this observation might be a varying efficiency of the detector with at different exposure times. This does not mean different efficiencies for the creation of visible light in the CsI screen (further explanation in section 4.2.3) since there is no physical reason for such an effect, but a changing efficiency on the software level of the single photon detection. If this is the case, determining the saturation coefficient by using two different exposure times might lead to a wrong value. Since all measured spectra are corrected for saturation, this can lead to mistakes in following steps of data processing like, e. g., the correction of detector efficiency. A possible improvement might be the utilization of two different incoming beam intensities instead of different exposure times for the determination of the saturation coefficient.

Even if it is not mentioned as the first correction, the saturation correction should be the first correction to be applied, especially since the distortion correction is redistributing intensity between the pixels and thus would change the n on the right side of equation 4.14.

Efficiency

To calibrate the efficiency of the detection system, the eight most intensive fluorescence lines (see table 4.1) from a specially prepared calibration sample made of Bi- and Tl-oxides (in the following only called BiTl-sample) are measured. The relative intensities of the different fluorescence lines are known and thus the measured intensities can be corrected.

To determine the measured intensities a sum of Voigt profiles (one for each

Table 4.1 Fluorescence lines and corresponding energies, relative intensities and natural line widths of the eight most intensive fluorescence lines of Bi and Tl taken from [TAG+09, KO79].

Element	Fluorescence line	Energy [keV]	Intensity [%]	Natural line width (FWHM) [eV]
Tl	K_{α_2}	70.8319	29.557	63.8
	K_{α_1}	72.8715	49.261	63.1
	K_{β_3}	82.118	5.911	
	K_{β_1}	82.576	11.330	
Bi	K_{α_2}	74.8148	29.412	70.1
	K_{α_1}	77.1079	49.020	69.4
	K_{β_3}	86.834	5.882	
	K_{β_1}	87.343	11.275	

peak) is fitted to the spectrum. A Voigt profile $V(x)$ is the convolution of a Lorentzian function $L(x)$ with a Gaussian function $G(x)$ where x is the channel number as follows:

$$\begin{aligned} V(x) = (G * L)(x) &= \int G(\tau)\, L(x-\tau)\, \mathrm{d}\tau \\ G(x) &= \frac{1}{\sigma\sqrt{2\pi}} \exp\left(\frac{-x^2}{2\sigma^2}\right) \\ L(x) &= \frac{\gamma}{\pi\left((x-x_0)^2 + \gamma^2\right)}. \end{aligned} \tag{4.15}$$

The Lorentzian models the natural lineshape of the emission line, while the convolution with the Gaussian accounts for the experimental resolution. By setting the width of the Lorentzian function γ to the natural linewidth of the according emission line (taken from [KO79]), the energy resolution of the spectrometer can be directly found from the standard deviation σ of the Gaussian function. The third fitting parameter is the position of the Lorentzian x_0, which corresponds to the energy of the fluorescence line.

Figure 4.11 shows the relative efficiency, determined from the spectra taken with an exposure time of 61 ms (brown) and 0.7 ms (blue), as a function of the channel number. The spectra are corrected for distortion and saturation and the peaks were fitted with Voigt functions. To get the expected intensities, the theoretical intensities from [TAG+09] are corrected for the absorption cross-section and internal absorption. Finally, the measured intensities are divided by the expected intensities to obtain the relative efficiency. For both curves

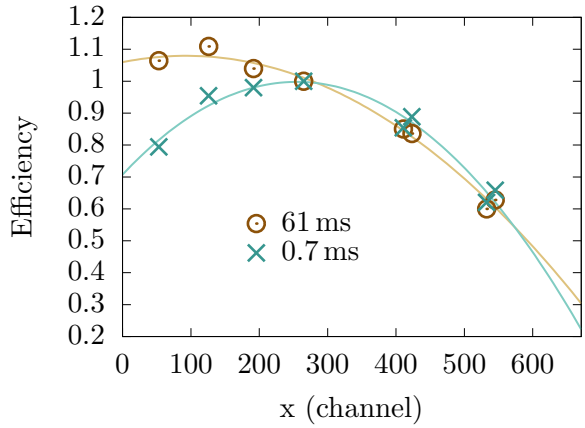

Figure 4.11 Relative efficiency of the spectrometer determined by fluorescence lines of Bi and Tl with an exposure time of 61 ms (brown) and 706 µs (blue). The solid lines show polynomial fits to the data.

the second order polynomial fit describes the data well.

The measured data is corrected by the 61 ms curve as this corresponds to the exposure time in standard operation mode. As the difference in the detector efficiencies with 61 ms and 706 µs cannot originate from a different efficiency of the CsI screen [2], it has to come from a difference on the electronics level as already mentioned in the saturation correction part. So this is another clear sign that the saturation correction procedure should be improved.

Energy Calibration

The fluorescence lines of BiTl are also used for the energy calibration of the spectrometer. Since the energies of the lines are well known (see table 4.1), a relationship between channel number and energy can be established. Figure 4.12 shows the non-linear calibration line.

From the non-linear connection between the channel and energy scale it becomes obvious that an energy bin in the high and low energy regions corresponds to smaller or larger channel bins, respectively. Therefore, a naive interpolation onto the new scale would change the measurement statistics. To solve this problem, within this project, a redistribution of the intensity in the channel bins into the energy bins was chosen.

[2] The screen does not know about the detector settings.

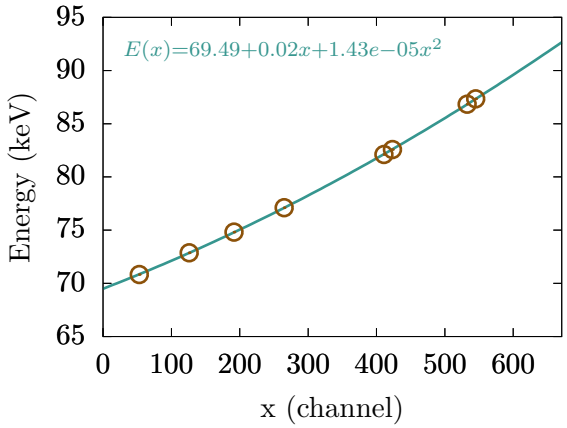

Figure 4.12 Second order polynomial fit (blue) to the experimental Bi/Tl data showing the energy calibration of the spectrometer. The insert text shows the equation of the parabola.

Absorption

The next step is the correction for the x-ray absorption in the sample. Instead of looking at the absorption we look at the percentage of photons being transmitted from source to detector without being absorbed. Since the energy of the scattered photon E_2 is not fixed, the transmission $T(E_2)$ is a function of the energy and can be described by

$$T(E_2) = I_2/I_1 = \frac{1-\exp(-d\cdot C)}{d\cdot C}, \qquad C = \left(\frac{\mu\,(E_1)}{\cos\alpha} + \frac{\mu\,(E_2)}{\cos\beta}\right) \tag{4.16}$$

where I_1 and E_1 are the flux and energy of the incoming beam while I_2 corresponds to the rate of photons hitting the detector [CMS+04]; $\mu\,(E)$ is the photon absorption coefficient at the energy E and d is the thickness of the sample (see blue line in figure 4.14). The angles α and β are the angles between incoming and outgoing beams and the surface normal, respectively (see inset of figure 4.13). The Compton profiles are then divided by this energy dependent transmission factors.

Figure 4.13 shows the transmission factors for four different scattering geometries of the Pd sample used for the study in chapter 6. Due to the comparably high[3] atomic number of Pd in some geometries more than 80 % of the incoming x-rays are absorbed.

[3]High in the context of Compton scattering experiments.

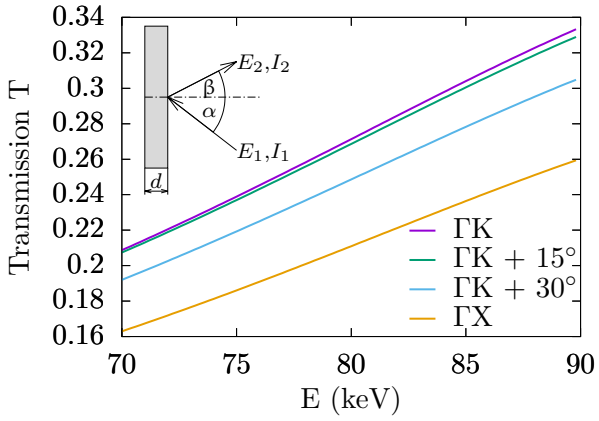

Figure 4.13 Transmitted intensity for Compton scattering in Pd with an incoming energy of$E_1 = 115.6\,\text{keV}$. The transmitted intensity is shown for four different scattering geometries for a crystal of 1 mm thickness and with a surface normal along the (110) crystal direction. The inset on the upper left shows the definitions of the angles α and β. Indices 1 and 2 are used for initial and scattered beam respectively.

Multiple Scattering

The correction for multiple scattering in the sample is of crucial importance to obtain physically meaningful Compton spectra. In most x-ray experiments, multiple scattering does not influence the results significantly since in the relevant energy range the absorption cross section is much higher than the scattering cross section. The situation changes completely in the Compton scattering regime. Figure 4.14 shows the cross sections for different kinds of photon-matter interactions in Pd[4] and shows clearly that at energies used for Compton scattering (typically $\sim 100\,\text{keV}$) the cross sections for Compton scattering (green line) and photoabsorption (red line) become equal.

At the beginning of Compton scattering era, in the 1970s, this issue was solved by using samples of different thickness for the measurements and extrapolating to zero thickness, where the multiple scattering contribution is assumed to be zero [RE72, TE74]. Felsteiner et al. [FPC74] could solve the multiple scattering problem for the first time using Monte Carlo simulations. Later the simulations were adapted to linearly polarized photons from a synchrotron source [CLF85, BF95, FHBS98] which build the basis for Compton profile evaluation nowadays.

[4]The spectra are calculated with the XCOM program created by the NIST (National Institute of Standards and Technology).

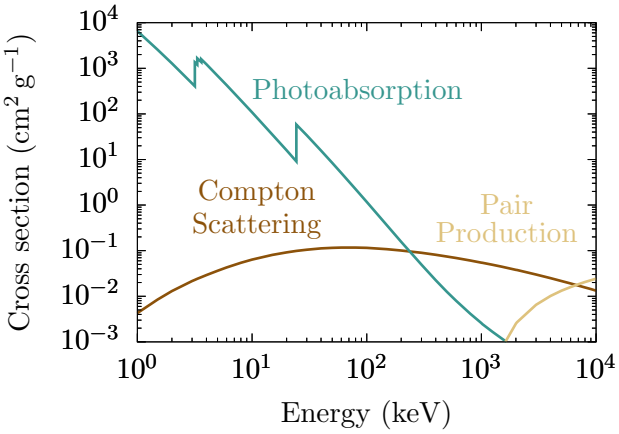

Figure 4.14 Cross section for different photon-electron interactions in Pd.

In this thesis, the MUSCAT program developed by Brancewicz et al. [BIS16] is used to calculate the double scattering and higher order contributions. Figure 4.15 shows a typical multiple scattering spectrum as simulated by MUSCAT. The diagram shows single scattering, double scattering, higher order scattering (triple+) and total scattering intensities. Typically in metallic samples the multiple scattering contribution can be around 10 %. However, the size and especially thickness of the sample play a crucial role.

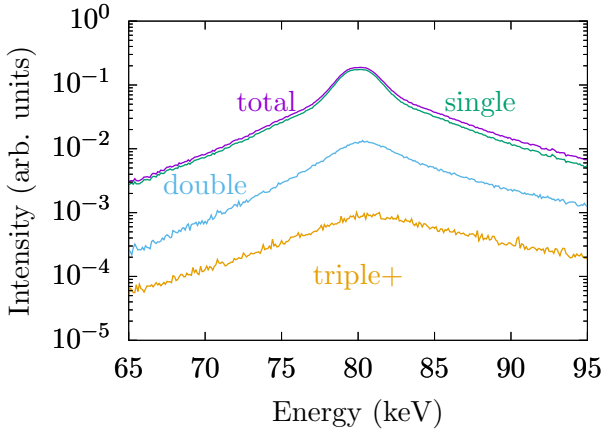

Figure 4.15 Multiple scattering profiles for single, double, triple and higher order (triple+) scattering in Pd obtained with the Monte Carlo program MUSCAT. The sum of all scattering processes is also shown (total).

Cross Section

The double differential cross section $\frac{d^2\sigma}{d\omega_2 d\varphi}$ is related to the Compton profile $J(p_z)$ via a factor $C(\omega_1, \omega_2, \varphi, p_z)$ depending on the scattering parameters.

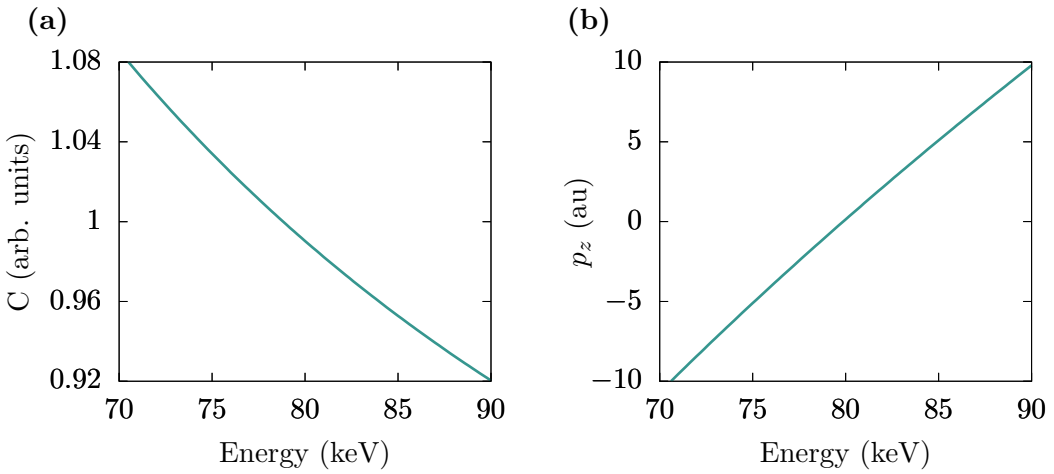

Figure 4.16 (a) Correction function of the Compton scattering cross section calculated for an incoming energy of $\omega_1 = 115.6\,\text{keV}$ and a scattering angle $\varphi = 165°$. (b) Transfer function between the energy and momentum scales.

The following equations will only give the result (using natural units) on how to calculate C-factor without further explanation. For the full relativistic derivation please refer to the work by Holm [Hol88].

$$J(p_z) = C\left(\omega_1, \omega_2, \varphi, p_z\right) \cdot \frac{d^2\sigma}{d\omega_2 d\varphi} \tag{4.17}$$

$$C\left(\omega_1, \omega_2, \varphi, p_z\right) = \frac{2\omega_1 K}{m^2 r_0^2 \omega_2} \frac{E(p_z)}{\bar{X}_{int}(|p_z|)} \tag{4.18}$$

$$\bar{X}_{int}(|p_z|) = \frac{R_1}{R_2} + \frac{R_2}{R_1} + 2m^2\left(\frac{1}{R_1} - \frac{1}{R_2}\right) + m^4\left(\frac{1}{R_1} - \frac{1}{R_2}\right)^2 \tag{4.19}$$

$$R_1 = \omega_1\left[E(p_z) - D(|p_z|)\right] \tag{4.20}$$

$$R_2 = R - \omega_1\omega_2(1 - \cos\varphi) \tag{4.21}$$

$$D = \frac{1}{K}(\omega_1 - \omega_2\cos\varphi)A(p) \tag{4.22}$$

$$A = \frac{1}{K}\left[(\omega_1 - \omega_2)E(p_z) - \omega_1\omega_2(1 - \cos\varphi)\right] \tag{4.23}$$

$$E(p_z) = \sqrt{m^2 + p_z^2} \tag{4.24}$$

$$p_z = \frac{K}{2} - (\omega_1 - \omega_2)\left[\frac{1}{4} + \frac{m^2}{2\omega_1\omega_2\left(1 - \cos\varphi\right)}\right]^{1/2} \tag{4.25}$$

$$K = |k_1 - k_2| = \left(\omega_1^2 + \omega_2^2 - 2\omega_1\omega_2\cos\varphi\right)^{1/2} \tag{4.26}$$

Here m is the electron rest mass, r_0 is the classical electron radius, φ is the scattering angle and ω_1 and ω_2 are the frequencies or energies of the incoming and scattered photons, respectively.

The cross section correction function for incoming energy of $\omega_1 = 115.6\,\mathrm{keV}$ and a scattering angle $\varphi = 165°$ is shown in figure 4.16 (a). Those parameters are typical for a scattering vector perpendicular to the surface normal of the sample at the SPring-8 spectrometer. All Compton profiles are multiplied by this function.

Calibration of Momentum Scale

Until this step, all corrections have been applied either on the channel or energy scale. Finally the energy scale can be transferred to momentum scale using equations 4.26 and 4.25. The transfer function for the standard parameters at the SPring-8 spectrometer ($\omega_1 = 115.6\,\mathrm{keV}$, $\varphi = 165°$) is shown in figure 4.16 (b). As already explained in the energy calibration part, rebinning should be used instead of interpolation as this is a non-linear relationship.

Normalisation of the Profile

Finally all profiles are normalized to the number of electrons involved in the Compton scattering. As the accessible momentum range of the BL08W spectrometer is approximately -9.9 to $9.9\,\mathrm{a.u.}$ the number of electrons is usually determined in this range from Hartree-Fock Compton profiles [BMM75].

Chapter 5

Reconstruction in Higher Dimensions

While calculating projections from a higher dimensional distribution is mathematically trivial, the inverse transformation is more complex. Usually, the 1D-to-2D reconstruction problem, relevant e. g. in Compton scattering, or the 2D-to-3D reconstruction problem, e. g. from 2D-ACAR data, is solved by methods either inspired by the analytical inversion of the Radon transformation or by series expansion, as e.g. applied by the Cormack's method (CM) [KS09]. In this work, a more general approach to solve this inverse problem is presented[1]. It employs linear matrices to model the experiment and a quadratic regularization functional to reduce experimental noise in the reconstruction. Thus, the solution of the reconstruction problem is the solution of a linear system of equations, which can be found by direct inversion. This is why this method is called the direct inversion method (DIM).

In the first two sections of this chapter an overview of the most established reconstruction methods is given. First the approaches based on the analytical inversion of the Radon transform namely the direct Fourier transformation (DT) and filtered back-projection (FBP) are introduced. After that, CM, which is based on series expansion, is explained. As this is the most frequently used algorithm in ACAR and Compton scattering experiments in the last thirty years, the new DIM algorithm is benchmarked against CM in chapter 6. The last two parts of this chapter introduce the algebraic reconstruction technique (ART) and the DIM as a realization of it.

[1] Parts of this chapter, in particular section 5.4, have been published elsewhere [KBD+21].

5.1 Analytical Reconstruction

The Radon Transformation

Starting point for all analytical reconstruction techniques is the Radon transformation $\mathcal{R}$ [Rad17]. In his work Radon proofed three theorems that relate a 2D density $f(x, y)$ and its projection $F(\theta, p)$ onto a line $p = x\cos\theta + y\sin\theta$ with the projection angle θ. The first one,

$$\begin{aligned} F(p,\theta) = \mathcal{R}\big\{f(x,y)\big\}(p,\theta) &= \int_{-\infty}^{+\infty} f\left(p\cos\theta - s\sin\theta, p\sin\theta + s\cos\theta\right) \mathrm{d}s \\ &= \iint f(x,y)\delta(x\cos\theta - y\sin\theta - p)\,\mathrm{d}x\,\mathrm{d}y, \end{aligned} \tag{5.1}$$

is the forward integral, commonly known as Radon transformation, which gives the projection from 2D densities to 1D line integrals. Here, δ is the delta distribution and s is the second polar coordinate perpendicular to p. Already at that time, Radon found an analytical solution to the inverse problem, which is given by the following two equations. In a first step the mean of $F(p, \theta)$ for the tangential lines of a circle around the center $P = (x, y)$ with radius q is calculated by

$$\bar{F}_P(q) = \frac{1}{2\pi}\int_0^{2\pi} F(x\cos\theta + y\sin\theta + q, \theta)\,\mathrm{d}\theta. \tag{5.2}$$

Finally, $f(x, y)$ can be recovered by

$$f(x,y) = \frac{1}{\pi}\lim_{\epsilon\to 0}\left(\frac{\bar{F}_P(\epsilon)}{\epsilon} - \int_\epsilon^{+\infty}\frac{\bar{F}_P(q)}{q^2}\,\mathrm{d}q\right). \tag{5.3}$$

However, this solution to the reconstruction problem, nowadays known as simple backprojection, is often not useful in real world, as experimental noise leads to blurring in the reconstructed image.

The Fourier Slice Theorem and Direct Fourier Transform

A first practically useful solution to the reconstruction problem is the so-called direct Fourier transformation (DT), which employs the Fourier slice theorem, that directly connects the Radon transformation and the Fourier transformation (FT). Figure 5.1 depicts the Fourier slice theorem in 2D.

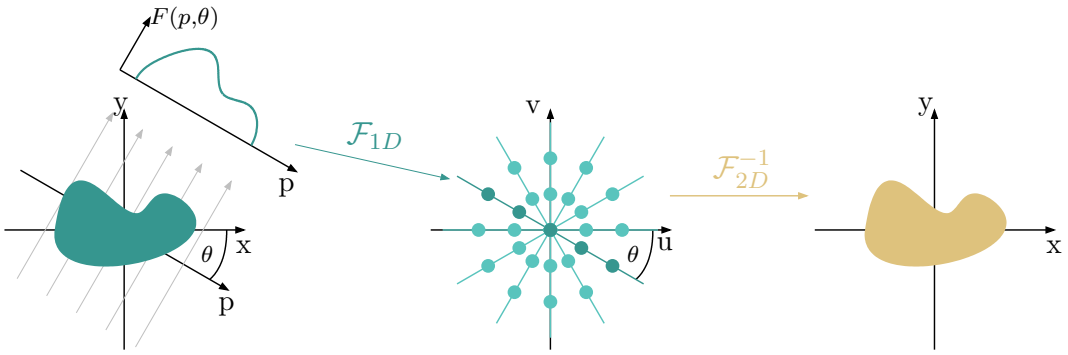

Figure 5.1 The object function $f(x, y)$ is projected by forming the line integral $F(\theta, r)$. According to the Fourier slice theorem the 1D Fourier transformation (FT) of a single projection $F(\theta, r)$ corresponds to a slice of the 2D FT of $f(x, y)$ under the same angle θ. The object function $f(x, y)$ is determined via a 2D inverse FT.

Starting point is the FT of a 1D projection $F(p, \theta)$ of a 2D density $f(x, y)$. The following equations show the equality of this 1D Fourier transform to a slice in the 2D Fourier space, also known as frequency space:

$$\begin{aligned}
\mathcal{F}_{1\mathrm{D}}\big\{F(p,\theta)\big\} &= \int F(p,\theta)e^{-2\pi i\omega p}\,\mathrm{d}p \\
&\overset{(5.1)}{=} \int \left[\iint f(x,y)\delta(x\cos\theta - y\sin\theta - p)e^{-2\pi i\omega p}\,\mathrm{d}p\right]\mathrm{d}x\,\mathrm{d}y \\
&= \iint f(x,y)e^{-2\pi i\omega(x\cos\theta - y\sin\theta)}\,\mathrm{d}x\,\mathrm{d}y \\
&= \mathcal{F}_{2\mathrm{D}}\big\{f(x,y)\big\}(u,v)|_{u=\omega\cos\theta, v=-\omega\sin\theta}.
\end{aligned} \tag{5.4}$$

This can be generalized to three dimensions, meaning that in general the FT of a projection of a density $\rho(x, y, z)$ along an arbitrarily chosen direction corresponds to a slice in the three dimensional Fourier space. Therefore, by knowing *all* projections the full Fourier space can be recovered and thus $\rho(x, y, z)$ can be determined by an inverse FT. In reality, a finite number of projections is sufficient for the DT, which enabled the first application of this analytically exact algorithm in the reconstruction of 3D structures in electron microscopy [DRK68, CDK70].

However, even if DT is a straight forward and fast technique it also inhibits some drawbacks. As the middle plot in figure 5.1 illustrates the data gets more sparse at higher frequencies, if we consider the u,v space as frequency. Thus, the necessary interpolation of the data to perform the inverse FT may introduce artifacts especially if high experimental noise is present. These drawbacks can

be compensated by measuring a high number of projections (less sparse data points) with high statistics. Even if this two requirements are rarely fulfilled in ACAR and Compton measurements at the same time, the DT technique was applied for both experiments multiple times. When it became popular in Compton scattering [e. g. TSS+01, KNS+06] it was already applied in ACAR [e. g. SOT+89, KKN+91, KKN+92] for about ten years.

Filtered Back Projection

The FBP, a technique that is closely related to the DT method was developed in 1971 [RL71]. It is the inverse process of getting the object function $f(x, y)$ from the experimentally measured projections $F(p, \theta)$ by applying the Fourier slice theorem. The original density $f(x, y)$ can be expressed as the inverse FT as follows:

$$\begin{aligned} f(x,y) &= \iint_{-\infty}^{+\infty} \mathcal{F}_{2\mathrm{D}}\big\{f(x,y)\big\}(u,v) e^{2\pi i(ux+vy)}\,\mathrm{d}u\,\mathrm{d}v \\ &= \int_0^{2\pi}\int_{-\infty}^{+\infty} \mathcal{F}_{1\mathrm{D}}\big\{F(p,\theta)\big\}(\omega,\theta)|\omega| e^{2\pi i\omega(x\cos\theta - y\sin\theta)}\,\mathrm{d}\omega\,\mathrm{d}\theta, \end{aligned} \tag{5.5}$$

where $\mathrm{d}u\,\mathrm{d}v = |\omega|\,\mathrm{d}\omega\,\mathrm{d}\theta$ originates from the Jacobian matrix of the coordinate transformation. If we now apply the symmetry of the FT with respect to the radial frequency $\mathcal{F}_{1\mathrm{D}}\big\{F(p,\theta)\big\}(\omega,\theta) = \mathcal{F}_{1\mathrm{D}}\big\{F(p,\theta)\big\}(-\omega,\theta+\pi)$, equation 5.5 can be simplified to

$$f(x,y) = \int_0^{\pi}\int_{-\infty}^{+\infty} \mathcal{F}_{1\mathrm{D}}\big\{F(p,\theta)\big\}(\omega,\theta)|\omega| e^{2\pi i\omega(x\cos\theta - y\sin\theta)}\,\mathrm{d}\omega\,\mathrm{d}\theta. \tag{5.6}$$

To understand the principle of FBP from this equation, it can be separated into two parts. The inner integral,

$$F(p,\theta) = \int_{-\infty}^{+\infty} \mathcal{F}_{1\mathrm{D}}\big\{F(p,\theta)\big\}(\omega,\theta)|\omega| e^{2\pi i\omega p}\,\mathrm{d}\omega, \tag{5.7}$$

weights the FT of the projection, and hence the measurement, with $|\omega|$ and transforms it to real space. This step is equivalent to applying a Fourier filter to the measurement. The outer integral

$$f(x,y) = \int_0^{\pi} F(x\cos\theta - y\sin\theta, \theta)\,\mathrm{d}\theta, \tag{5.8}$$

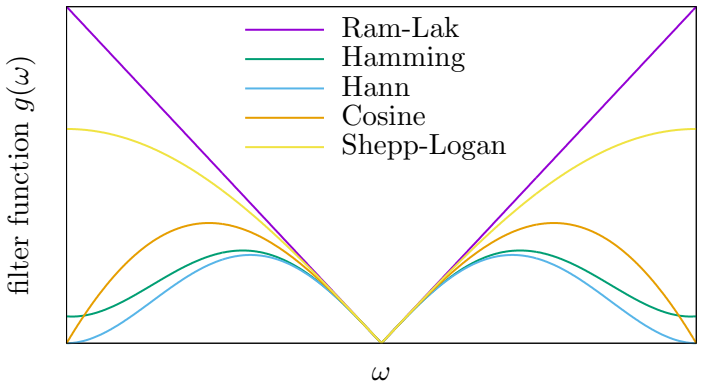

Figure 5.2 Different FBP filter functions. The basic Ram-Lak filter which originates from the coordinate transformation may lead to noise amplification at higher frequencies. This can be suppressed by the increasing roll-off at higher frequencies of the other filters.

defines the back projection. $F(p, \theta)$ is smeared out along the direction of projection as for a fixed projection angle θ and without the integration of all points (x, y) on the line $p = (x \cos\theta - y \sin\theta)$ have identical values. To finally arrive at the reconstruction the integral forms the mean of all filtered back projections over all angles θ.

As the $|\omega|$-factor, first introduced by Ramachandran and Lakshminarayanan [RL71] and thus called Ram-Lak filter, leads to an amplification of high frequency noise, over the years several other filter functions $g(\omega)$, rolling off in comparison to the linear Ram-Lak filter, at higher frequencies, were introduced. Some examples are shown in figure 5.2. These filter functions are defined as follows:

$$g(\omega) = \begin{cases} |\omega|\,[0.5 + 0.5\cos(2\pi\omega)] & \text{Hamming} \\ |\omega|\,[0.54 + 0.46\cos(2\pi\omega)] & \text{Hann} \\ |\omega|\cos(\pi\omega) & \text{Cosine} \\ |\omega|\text{sinc}(\omega) & \text{Shepp} - \text{Logan} \quad [\text{SL74}] \end{cases} \tag{5.9}$$

As all of those functions roll off at higher frequencies they are capable of reducing the noise. However, this comes with the trade-off of reduced spatial resolution.

While several examples for the application of FBP in 2D-ACAR exist [FSBB79, Man82, JMP83], to the authors knowledge it was not used in the analysis of Compton scattering data so far.

5.2 Cormack's Method

In contrast to the analytical inversion of the Radon transformation discussed in the previous chapters, Cormack's method (CM) uses the expansion of measurements into a set of orthogonal functions for the reconstruction. An important feature of this function set is their known transformation from Radon space to real space. The starting point of CM is the expansion of both, the measurement $F(p,\theta)$ under angle θ and the original density in polar coordinates $f(r,\Phi)$ into Fourier series:

$$\begin{aligned} F(p,\theta) &= \sum_{n=-\infty}^{+\infty} F_n(p)\, e^{i\theta n} \\ f(r,\Phi) &= \sum_{n=-\infty}^{+\infty} f_n(r)\, e^{i\Phi n} \end{aligned} \tag{5.10}$$

where the expansion coefficients are given by

$$\begin{aligned} F_n(p) &= \frac{1}{2\pi}\int_0^{2\pi} F(p,\theta) e^{-in\theta}\,\mathrm{d}\theta \\ f_n(r) &= \frac{1}{2\pi}\int_0^{2\pi} f(r,\Phi) e^{-in\Phi}\,\mathrm{d}\Phi. \end{aligned} \tag{5.11}$$

Cormack derived a solution for the coefficients $f_n(r)$ from the projections coefficients $F_n(p)$ based on Chebyshev polynomials of the first kind, $T_n(x) = \cos(n \arccos x)$ [Cor63]:

$$f_n(r) = \frac{1}{\pi}\frac{\mathrm{d}}{\mathrm{d}r}\int_0^{\pi} \frac{F_n(p) T_n(r/p)}{\sqrt{r^2-p^2}}\,\mathrm{d}p. \tag{5.12}$$

As this analytically exact solution has the practical disadvantages of the necessary numerical differentiation and integration, Cormack only applied it to the most simple case, namely a density $f(r)$ which was only varying with radius r but not with angle Φ. However, just one year later he published two solutions to this drawback by expanding $f_n(r)$ and $F_n(p)$ themselves [Cor64].

The first solution is valid inside the unit circle and uses the expansion into Zernicke polynomials $R_n^m(r)$ [Zer34], defined by

$$R_n^m(r) = \sum_{s=0}^{m} \frac{(-1)^s (n+2m-s)!}{s!(n+m-s)!(m-s)!} r^{n+2m-2s}. \tag{5.13}$$

If the $F_n(p)$ are expanded into

$$F_n(p = \cos\psi) = 2\sum_{l=0}^{+\infty} a_n^l \sin[(n + 2l + 1)\psi] \tag{5.14}$$

the coefficients $f_n(r)$ are given by

$$f_n(r) = \sum_{l=0}^{+\infty}(n + 2l + 1)a_n^l R_n^l(r). \tag{5.15}$$

In practice, the theoretical limitation to the unit circle hardly plays any role as most problems can be mapped to the unit circle. However, even this limitation was overcome by Cormack through expansion into Hermite polynomials $H_m(p)$. Thus, if the measurement coefficients are given by

$$F_n(p) = e^{-p^2}\sum_{l=0}^{+\infty} b_n^l H_{n+2l}(p), \tag{5.16}$$

the density coefficients can by calculated as

$$f_n(r) = \frac{e^{-p^2}}{\sqrt{\pi}}\sum_{l=0}^{+\infty}(-1)^l 2^{n+2l} l! b_n^l r^n L_{2l}^n(r^2), \tag{5.17}$$

where $L_{2l}^n(r^2)$ are the Lageurre polynomials as defined in [Erd53].

As the whole reconstruction is basically an expansion into orthogonal functions it is easy to take into account the statistical accuracy of the data. Furthermore, in the reconstruction, the crystal symmetries can be taken into account by replacing the Fourier expansion with an expansion into lattice harmonics [Mij67]. Due to these two advantages CM was regularly used in both the analysis of Compton scattering and ACAR data. In a review article Kontrym-Sznajd [KS09] counted more than twenty publications using CM between 1989 and 2007. Two recent examples for Compton scattering and 2D-ACAR are measurements on $PdCrO_2$ [BEM+15] and Ni_2MnGa [HWL+12], respectively. In chapter 6 the CM as modified by Kontrym-Sznajd [KS90] in the particular implementation of Dugdale [Dug96] was used.

5.3 Algebraic Reconstruction Techniques (ART)

There are four conditions which make all the previously explained reconstruction methods analytically exact:

- *infinitely* good statistics
- *homogeneous* resolution function
- projected data measured in *continuous* space
- measuring *all* projection angles.

In x-ray computed tomography (CT) those conditions may be *almost* fulfilled. However, neither in Compton scattering nor in ACAR experiments any of the conditions is fulfilled. Statistics of a measurement are not infinitely high due to limited measurement time and only a few projections of a crystal are measured. Furthermore the data are always measured for a limited number of bins/pixels and are thus far from being continuous. Also the resolution function is not homogeneous. The most simple reasons are the non-linear binning between channel and momentum scale in Compton scattering, or the limited spot size in an ACAR experiment.

Therefore, Gordon et al. [GBH70] used a new approach, which they called ART. They replaced the continuous projection integral by an algebraic equation which calculates the measured projection y^α of a density ρ along at angle α through a matrix multiplication with a linear projection operator $\boldsymbol{T}^\alpha$

$$y^\alpha = \boldsymbol{T}^\alpha \rho. \tag{5.18}$$

Here, ρ can either be a 2D or a 3D density, as the pixels or voxels can be rearranged as a 1D vector. Already in the first years, several solutions for the inversion of equation 5.18 were found [HL76]. However, due to high dimensionality of the problem and limited computer power, most of those methods used iterative approaches.

In the last twenty years ARTs were regularly used in the 2D-to-3D reconstruction in 2D-ACAR [CMS+04, FPP+10, PDKS11, PKSD11, WBB+15, WBA+17] due to advantages like the relatively simple consideration of the experimental statistics or resolution. However, as all of those approaches use an entropy-like, non-linear regularization functional, iterative algorithms are required to find a

reconstruction even if modern computers would be capable of performing the inversion of large matrices within reasonable time. In contrast, the new direct inversion method (DIM), introduced in the next section, uses general cases of the Thikonov regularization [Tik63] to reconstruct a large area of interest without iterations.

5.4 Direct Inversion Method (DIM)

The DIM was first published for the reconstruction of Compton data measured on Pd [KBD+21]. The following section is adopted from chapter II.B. of this paper.

The starting point for this approach is a linear operator, $\boldsymbol{T}^{\alpha}$ (dimension $n \times m$), which projects a density ρ (m voxels or pixels rearranged as a 1D vector), onto a 1D or 2D spectrum, y^{α}, and thus mimics the Compton scattering or 2D-ACAR experiment. Therefore y^{α} either describes the Compton profiles, each of which is a vector of intensity values with length n, or the 2D-ACAR spectrum with a total number of n pixels, again rearranged as a 1D vector. One fact that we implicitly take into account is that a 3D-to-1D projection can be seen as successive projections from 3D to 2D and then from 2D to 1D. $\boldsymbol{T}^{\alpha}$ distributes the density in every element of ρ into the bins or pixels of y^{α}, where α indexes the N measured projections, as shown in equation 5.18. While y^{α} can be computed easily from a given ρ, solving the inverse problem, i. e. finding ρ from a small number of projections, is more complex since it is under-determined.

Many elements of ρ are equivalent due to the crystal point symmetry. Therefore, we can introduce the symmetry operator, $\boldsymbol{S}$, which reduces the dimension of the problem to the independent degrees of freedom, x, representing the irreducible area or wedge of the reconstructed density,

$$\rho = \boldsymbol{S}x. \tag{5.19}$$

The exact dimensions of $\boldsymbol{S}$ and x depend on the symmetry of the reconstructed density. However, as a rule of thumb, we can state that x has approximately the length of m divided by the number of symmetry operations.

By concatenating the y^{α} vectors to a vector y with length l (where $l = nN$ for Compton profiles or ACAR spectra of equal size), representing all of the

measured data, and the $\boldsymbol{T}^{\alpha}$ matrices to a corresponding projection operator, $\boldsymbol{T}$ (dimension $l \times m$) the α index can be neglected in the following. The maximum-likelihood estimation of x, can now be obtained by minimizing the χ^2-functional,

$$\chi^2(x) = (y - \boldsymbol{T}\boldsymbol{S}x)^{\top} \boldsymbol{W} (y - \boldsymbol{T}\boldsymbol{S}x). \tag{5.20}$$

The weighting matrix, $\boldsymbol{W}$ (dimension $l \times l$), is a diagonal matrix with the values σ_i^{-2}, where σ_i are the uncertainties of each measured data point.

Since the inverse problem is under-determined, a large number of different reconstructions, x, may give χ^2 values in accordance with the correct statistical accuracy. Additionally, were $\chi^2(x)$ to be minimized without any additional regularization, the Poisson noise of the data would arguably lead to noise in the reconstruction, commonly known as over-fitting. A regularization functional, $r(x)$, is therefore introduced to find a smooth and, thus, physically meaningful solution. This leads to the new functional,

$$f(x) = \chi^2(x) + r(x), \tag{5.21}$$

which has to be minimized.

One problem, which especially arises in Compton scattering is the fact, that the momentum density decays only slowly with increasing momentum as all electron states (including the strongly localized core states) contribute to the measurement signal. Conventionally, a large momentum range thus has to be reconstructed in order to avoid reconstruction artefacts, implying either an excessive increase of the required computational power or a coarse sampling of momentum space. We solved this problem by utilizing the fact that the core levels, which are exclusively responsible for the densities at large momenta, have a signature that is isotropic for all practical purposes. This leads us to the following procedure: All spectra, y^{α}, are averaged and fitted with a sum of Gaussians centered at zero momentum. The sum of Gaussians is then subtracted from every Compton profile, giving the 1D anisotropies. From those, the anisotropy of ρ is reconstructed and, since the transformation of a Gaussian from 1D to 2D or 3D is known, the isotropic higher dimensional Gaussian functions can be added to the reconstruction of the anisotropy afterwards, which gives the reconstruction of the full signal. Even if this problem is not equally present in ACAR experiments, as due to influence of the positron, the TPMD decays much faster in momentum space (see chapter 3.3.6), subtracting

the isotropic part of the measured data and reconstructing only its anisotropy can still minimize the dimensionality of the problem.

As the anisotropy of the data comprises positive and negative values, the classical maximum entropy regularization [GD78] cannot be applied since the logarithm can only deal with positive densities. Additionally, the logarithm is not linear and thus the direct inversion would not be possible. Therefore, another functional which is both linear and able to deal with positive and negative densities has to be found. Here it is necessary to distinguish if the reconstructed density is 2D, and thus a projection of the EMD or TPMD itself, or 3D. While the 3D-EMD or TPMD shows sharp steps at the FS, their 2D projection is smeared. Thus different regularization functionals are used.

Reconstruction of a 2D density

The projection integral, in general, leads to continuous 2D spectra. To bias the reconstruction towards the aforementioned behavior, the use of a sum of first and second derivatives as a regularization functional seems reasonable. The first derivative operator $\boldsymbol{D_1}$ can be expressed as a discrete difference operator which, by operating on ρ, gives the difference between every pixel and the pixel to the right, and the difference between the pixel and the pixel below. Thus, if ρ consists of m pixels, $\boldsymbol{D_1}$ has a dimension of $2m \times m$ (neglecting boundary effects). The second derivative operator $\boldsymbol{D_2}$ can easily be derived by multiplying $\boldsymbol{D_1}$ with its transpose matrix. To summarize, $f(x)$ can be written as follows,

$$\begin{aligned} f(x) =& \chi^2(x) + \lambda_1 x^\top \boldsymbol{S}^\top \boldsymbol{U}^\top \boldsymbol{D_1}^\top \boldsymbol{D_1} \boldsymbol{U} \boldsymbol{S} x \\ &+ \lambda_2 x^\top \boldsymbol{S}^\top \boldsymbol{U}^\top \boldsymbol{D_2}^\top \boldsymbol{D_2} \boldsymbol{U} \boldsymbol{S} x, \end{aligned} \tag{5.22}$$

where $\lambda_{1,2}$ are positive real numbers. As a given absolute variation of anisotropy is more likely where the intensity itself is high, we scale the trial densities so as to correspond to the relative deviations from the isotropic 2D reconstruction. This is achieved through multiplication by a diagonal scaling matrix $\boldsymbol{U}$ (dimension $m \times m$) before applying the derivative operators.

To find the minimum of the quadratic function $f(x)$ we have to find the x obeying $\nabla f(x) = 0$. The matrices associated to both the χ^2 and the regularization functionals can be written as the square of real matrices (or a sum thereof) and are consequently positive semi-definite. The null space of

the regularization functional matrix consists of the space of constant densities, which is not in the null space of the χ^2 functional matrix, thus the quadratic form $f(x)$ is positive definite, its associated matrix is invertible, and the linear system of equations

$$\begin{aligned} 0 = &- 2\boldsymbol{S}^\top \boldsymbol{T}^\top \boldsymbol{W}^\top (y - \boldsymbol{T}\boldsymbol{S}x) \\ &+ 2\lambda_1 \boldsymbol{S}^\top \boldsymbol{U}^\top \boldsymbol{D}_\mathbf{1}^\top \boldsymbol{D}_\mathbf{1} \boldsymbol{U}\boldsymbol{S}x \\ &+ 2\lambda_2 \boldsymbol{S}^\top \boldsymbol{U}^\top \boldsymbol{D}_\mathbf{2}^\top \boldsymbol{D}_\mathbf{2} \boldsymbol{U}\boldsymbol{S}x, \end{aligned} \tag{5.23}$$

has exactly one solution. This unique x can easily be calculated by standard methods for solving linear systems of equations and is formally given by

$$\begin{aligned} x = \Bigg[&\boldsymbol{S}^\top \left(\boldsymbol{T}^\top \boldsymbol{W}\boldsymbol{T} + \lambda_1 \boldsymbol{U}^\top \left(\boldsymbol{D}_\mathbf{1}^\top \boldsymbol{D}_\mathbf{1} \right) \boldsymbol{U} + \right. \\ &\left. \lambda_2 \boldsymbol{U}^\top \left(\boldsymbol{D}_\mathbf{1}^\top \boldsymbol{D}_\mathbf{1} \boldsymbol{D}_\mathbf{1}^\top \boldsymbol{D}_\mathbf{1} \right) \boldsymbol{U} \right) \boldsymbol{S} \Bigg]^{-1} \left(\boldsymbol{S}^\top \boldsymbol{T}^\top \boldsymbol{W} y \right). \end{aligned} \tag{5.24}$$

Reconstruction of a 3D density

The 3D EMD and TPMD both show sharp steps at the FS. Therefore, the first and second derivative regularization would smooth this step as variations of neighbouring voxels would be punished. This can be inhibited by using the zero order derivative, meaning the reconstructed anisotropies as a regularization. By that, strong deviations from zero originating from noise are reduced, but neighbouring voxels can behave independently. Since variations are more likely to be stronger, if the intensity itself is larger, analogically to above, the scaling matrix $\boldsymbol{U}$ is used.

Thus, the final functional $f(x)$ can be written as

$$f(x) = \chi^2(x) + \lambda x^\top \boldsymbol{S}^\top \boldsymbol{U}^\top \boldsymbol{U}\boldsymbol{S}x \tag{5.25}$$

and the reconstruction is given by

$$x = \left[\boldsymbol{S}^\top \left(\boldsymbol{T}^\top \boldsymbol{W}\boldsymbol{T} + \lambda \boldsymbol{U}^\top \boldsymbol{U} \right) \boldsymbol{S} \right]^{-1} \left(\boldsymbol{S}^\top \boldsymbol{T}^\top \boldsymbol{W} y \right). \tag{5.26}$$

The fact that the results for both cases can be found by direct inversion, makes the DIM reconstruction technique fast and efficient in comparison to

reconstruction algorithms applying non-linear regularization functionals. Furthermore, in case of the iterative methods, a convergence criterion has to be defined. This is not necessary for the DIM as the inversion directly gives the final result.

For simplicity additional information like the resolution function or the MSF of an ACAR experiment were neglected in the derivation above. However, as generally in ART, such effects can easily be incorporated by simply introducing additional matrices.

Chapter 6

2D-ACAR and Compton Scattering on Pd

The electronic structure of the $4d$ transition-metal Pd is well studied, both theoretically and experimentally. Figure 6.1 shows the FS obtained from first-principles calculations within this project. In 1970 already all FS sheets were predicted theoretically. Müller et al. [MFDF70] found a Γ-centered electron sheet and three hole-like sheets. The first of which is a series of cubic-arranged interconnecting pipes, while the other two are small hole pockets centered at the high symmetry X- and L-points, respectively. Since the L-hole pockets have not been seen experimentally before [VP65], Müller et al. did not believe that it exists in reality. Two years later, however, its existence was confirmed by means of magnetoacoustic quantum oscillation measurements [BKMP72] and thus all FS sheets of Pd, as we know them today, were determined theoretically and experimentally. Nowadays it is the exact FS topology which is still subject of different studies. Östlin et al. [OADM$^+$16], e. g. have investigated the exact shape of the L-hole pocket influenced by local and non-local correlations which they have taken into account by different theoretical frameworks like local density approximation (LDA)+DMFT or the *GW* method [Hed65].

Another reason for the large interest in the high-susceptibility paramagnet Pd in condensed matter research is its proximity to ferromagnetism. It shows a high density of states at the Fermi level and a large Stoner enhancement in the magnetic susceptibility [CFGT68], which makes it a good candidate for the observation of spin fluctuations. The reduction of the electronic heat coefficient of 7.8 % at 11 T in specific heat experiments [HRW$^+$81] suggested that this might originate from reduced spin-fluctuations at high magnetic fields. Such a reduction of spin-fluctuations should subsequently lead to a difference

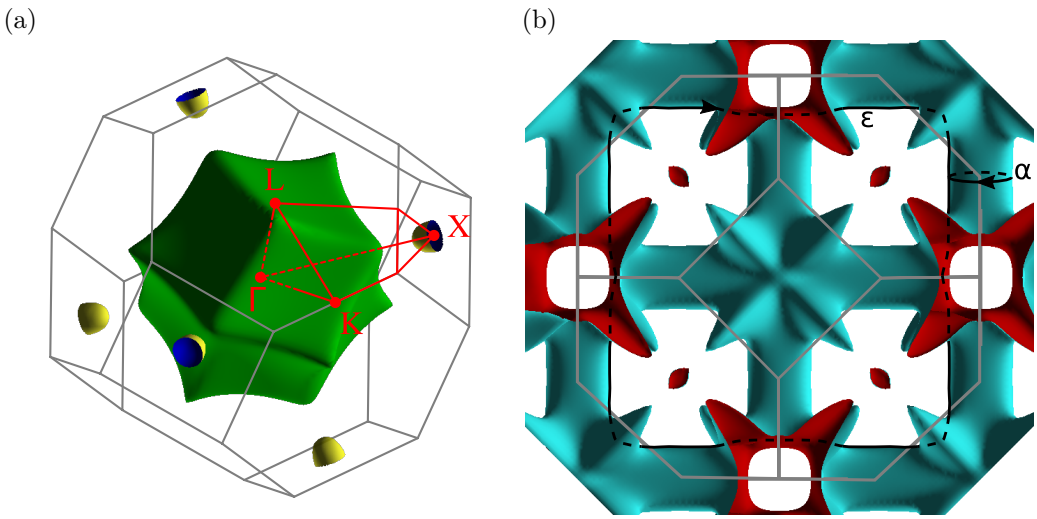

Figure 6.1 (a) Γ-centered electron sheet and X-hole pockets of the Fermi surface of Pd in the first Brillouin zone. The Γ, X, K, and L high symmetry points are shown in red (with Γ at the zone center). (b) Open-hole sheet and L-hole pockets of the Fermi surface. Additionally, the dHvA α and ϵ-orbit are shown. The ϵ-orbit lies in the (001) plane through the center of the Brillouin zone (plotted in XCrySDen [Kok99]).

in the volume between the spin-up and spin-down FS and a reduction of the cyclotron effective mass [DE66]. This could, however, not be seen in magnetic field dependent dHvA measurements up to 15 T [JHCV84, JC84]. Finally the nontrivial magnetic properties and dynamical fluctuations could be explained by Larson et al. by considering the mean-square amplitude of the spin-fluctuations instead of their average as commonly done [LMS04].

In this study Pd, is serving as a model system with a well characterized electronic structure. The main focus, however, is put on the experimental comparison between ACAR spectroscopy and Compton scattering. Although there have been measurements of both 2D-ACAR and Compton scattering on the same material (for example, Mg [NKKT92, BPA$^+$13] or Y [DFA$^+$97, KSSCP$^+$02]) it is very unusual for measurements to be made on the identical single crystalline sample. Here, 1D and 2D projections of the EMD and TPMD are compared in $\boldsymbol{p}$ space as well as in the reduced zone scheme of the first Brillouin zone ($\boldsymbol{k}$ space). Additionally, the experimental data are compared to first-principles calculations. For the comparison in 2D, the direct inversion method (DIM) algorithm introduced in section 5.4 is applied to experimental data for the first time. To benchmark its performance, the results are compared to a reconstruction by Cormack's method (CM). Main parts of this chapter have recently been published elsewhere [KBD$^+$21].

6.1 Experimental Details

In this study, 2D-ACAR and Compton scattering are compared in a systematic manner by performing measurements on the same disc-shaped Pd single crystal. The surface polished crystal has a diameter of 10 mm, a thickness of 1 mm and the surface normal is oriented along the [011] direction.

During the Compton scattering experiment, ten Compton profiles were measured at room temperature along crystallographic directions spaced equally between Γ-X and Γ-K. For the measurement of the Compton profiles, the crystal was mounted on a rotating stage with the [001] crystallographic direction oriented along the vertical rotation axis. For every profile, data was collected for at least 380 min leading to more than 1.6×10^5 counts in the Compton peak. Additionally, calibration measurements using a BiTl sample were made (see section 4.2.4). Background spectra were taken along the Γ-X and Γ-K directions and halfway between them. The background for all other directions was linearly interpolated. As explained in section 4.2.4 the measured raw data were corrected for several systematic effects to retrieve the Compton profiles from the measured data. The 1D-profiles were at the end normalized to the number of electrons in the corresponding momentum range (determined from Hartree-Fock free-atom Compton profiles [BMM75]) and have units of electrons per atomic unit of momentum space (el./a.u.). The momentum resolution of the measurement was 0.14 a.u..

In total, five 2D-ACAR measurements within the (011) plane were performed. The projections were taken along the crystallographic cubic high symmetry directions [100], $[0\bar{1}1]$ and $[1\bar{1}1]$, and at 27.4° and 72.4° away from [100] in the (011) plane. All measurements were conducted at 10 K to minimize the resolution degradation due to the thermal motion of the positron, and more than 5×10^7 coincident counts were collected per spectrum. The experimental resolution (FWHM) was 0.21 and 0.17 a.u. in the $p_{horizontal}$ and $p_{vertical}$ directions, respectively [LCW12]. Both momentum directions are perpendicular to the detector-detector direction.

6.2 First-Principles Electronic Structure Calculation

Ground-state electronic structure calculations were performed, in order to compare theoretical spectra with the experimental momentum densities. The calculations have been performed by collaborators from Cardiff University and University of Bristol. The Elk code [DSN$^+$], a highly-accurate full-potential augmented plane-wave plus local orbital (FP-APW+lo) method, was used to calculate the ground-state electronic structure of fcc Pd at the experimentally-determined [MB71] cubic lattice constant, $a = 3.890\,\text{Å}$. Convergence was achieved with a $16 \times 16 \times 16$ $\boldsymbol{k}$-point grid with a plane-wave cut-off in the interstitial region of $|\boldsymbol{G}+\boldsymbol{k}|_{max} = 8.0/R_{\text{mt}}$ (where $R_{\text{mt}} = 2.57\,\text{a.u.}$ was the muffin-tin radius) and the Perdew-Burke-Ernzerhoff general gradient approximation (GGA) [PBE96] was used for the exchange-correlation functional. The valence electron configuration was $4s^2 4p^6 4d^{10}$, and the remaining 28 electrons were considered to be core. Since Pd has a relatively high atomic number, the spin-orbit interaction was included in the calculations by adding a term of the form $\boldsymbol{\sigma} \cdot \boldsymbol{L}$ (where $\boldsymbol{\sigma}$ is the spin vector and $\boldsymbol{L}$ is the orbital angular momentum vector) to the second variational Hamiltonian.

Because the Compton scattering and 2D-ACAR experiments were performed at room temperature and at $T = 10\,\text{K}$, respectively, smearing widths (effective electronic temperatures) of 300 K and 30 K were used in the ground-state calculations from which the EMD and TPMD, respectively, were calculated using the method of Ernsting *et al.* [EBH$^+$14]. Compton scattering is equally sensitive to *all* electrons (core and valence) and, while the EMD was calculated only for the valence electrons, the momentum cut-off was $|\boldsymbol{p}|_{max} = 16.0$ a.u. to include contributions from the most tightly bound semi-core valence states. In the case of the TPMD this cut-off could be reduced to $|\boldsymbol{p}|_{max} = 8.0$ a.u. due to the small overlap of the positron wave function with the more tightly bound electron states. In order to understand the effect of electron-positron correlations on the measured densities, two different TPMD calculations were performed namely one with the independent particle model (IPM), assuming no enhancement [$\gamma(\boldsymbol{r}) = 1$] and a second applying the positron enhancement model proposed by Drummond *et al.* [DLRNP11] with gradient corrections [BPTN95].

6.3 Results and Discussion

6.3.1 2D-ACAR and 1D Compton scattering: Experiment and Theory

First, we compare the experimental results with the corresponding theoretical calculations, namely the experimental 2D-ACAR data to TPMD calculations and Compton data to EMD calculations. One of the first useful quantities to consider is the radial anisotropy. In the case of a simple metal, this radial anisotropy can be dominated by the presence of the Fermi surface but it also contains information about the anistropy of the wavefunctions of electrons in filled bands. Figure 6.2 shows the radial anisotropy of the five 2D-ACAR measurements and the corresponding theoretical TPMD calculations (IPM and Drummond enhancement). The theoretical spectra are convolved with a two-dimensional Gaussian function accounting for the instrumental momentum resolution. All experimental spectra were symmetrized according to the expected crystal symmetry. Comparing the calculation with Drummond enhancement to the IPM, we can see that the enhancement generates stronger anisotropies at higher momenta due to the fact that the positron, which is screened by an electron cloud, has an increased overlap with the more tightly bound electrons (which contribute at larger momentum) due to the weaker Coulomb repulsion [Rub08]. Overall we can state that, while there are regions of the experimental data which agree more closely with either one or the other approximations, it is certainly not the case that the enhancement produces a significant improvement in the radial anisotropy.

Figure 6.3 shows the directional difference between four Compton profiles measured along different directions and the Compton profile measured along the Γ-K direction. In all but the lowest Z elemental metals, the anisotropy between directions is usually dominated by the electrons in filled bands (since there are many more of them), rather than the (small number of) partially filled bands which give rise to the FS. All measurements show very good agreement with the first-principles calculations (which have been convolved with a one-dimensional Gaussian accounting for the experimental resolution). This is also true for the other five directions which are not explicitly shown here. The uncertainties are calculated from counting statistics propagated through the corrections.

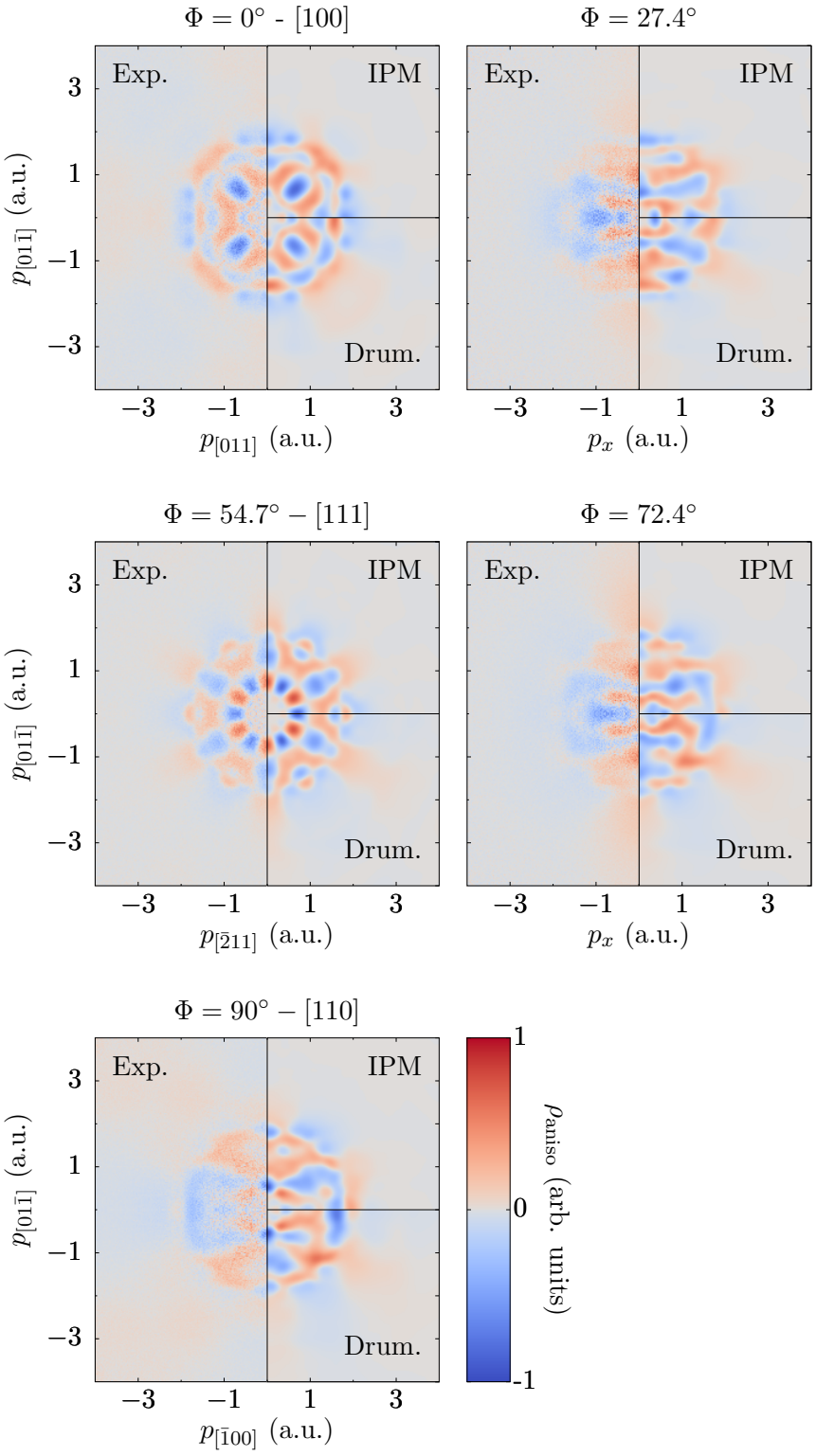

Figure 6.2 2D radial anisotropy of the five measured ACAR spectra (left half of each subplot) and the corresponding theoretical calculation, with (bottom right) and without Drummond (top right) enhancement. All calculations have been convolved with the experimental resolution, and all experimental spectra were symmetrized to the according crystal symmetry. The angle Φ denotes the angle measured from the [100] direction within the (011) plane.

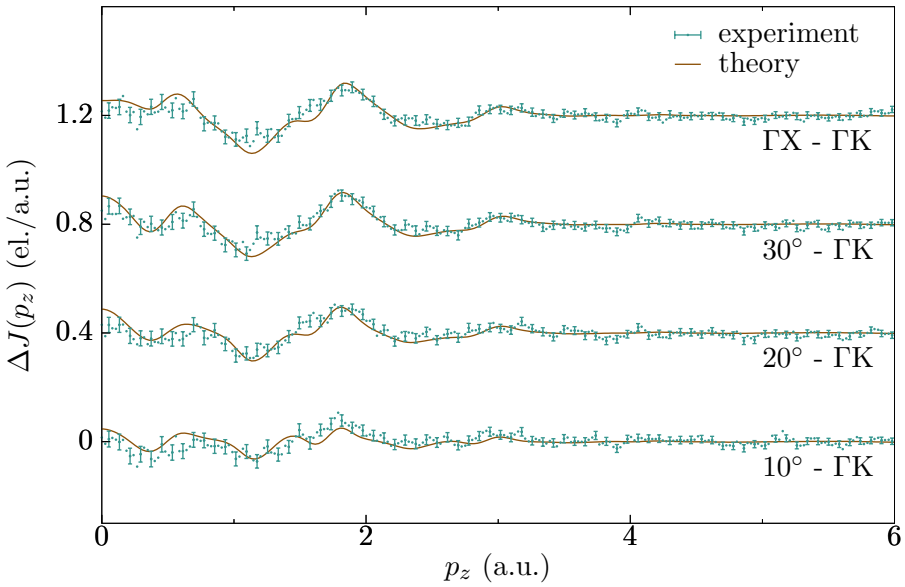

Figure 6.3 Directional differences of experimental (blue) and theoretical Compton profiles (brown). The labeled angles are measured from the Γ-K direction towards the Γ-X direction of the fcc Brillouin zone. The calculated profiles are convolved with a one-dimensional Gaussian accounting for the experimental resolution. For every third experimental data point an errorbar showing the statistical error of one standard deviation is plotted. The plots have been offset by 0.4 el./a.u. from one another for clarity.

6.3.2 2D-Reconstruction from 1D-Compton Profiles

As the Compton experiment measures 1D projections of the EMD, the 2D projection has to be reconstructed from a series of 1D measurements to compare it with the 2D-ACAR measurements. This was achieved with both the new DIM algorithm and the well-known CM [KS90] in order to benchmark the new algorithm. The required computational effort is much higher in DIM compared to CM due to the high number of free parameters in the DIM. However, a standard PC is still capable of calculating a reconstruction of 512×512 pixels from the ten Compton profiles within several minutes. In order to compare the results of both algorithms, it is, again, useful to consider the radial anisotropy of the (projected) EMD. This anisotropy will have contributions from both filled (due the anisotropy of the electron wavefunctions) and from partially filled bands (which additionally contains information about the FS). Figure 6.4(a) shows the radial anisotropy of the reconstructed spectra and of the first-principles calculations. All of the main features of the theoretical spectrum are reconstructed comparably well by both methods. At high momenta, the noise of the DIM reconstruction is more isotropic and, compared to CM, exhibits

(a)

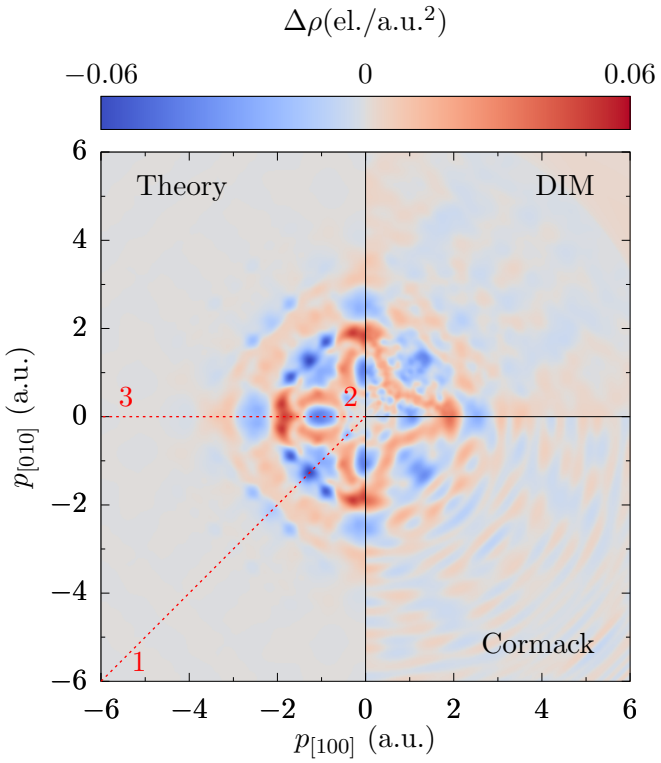

(b)

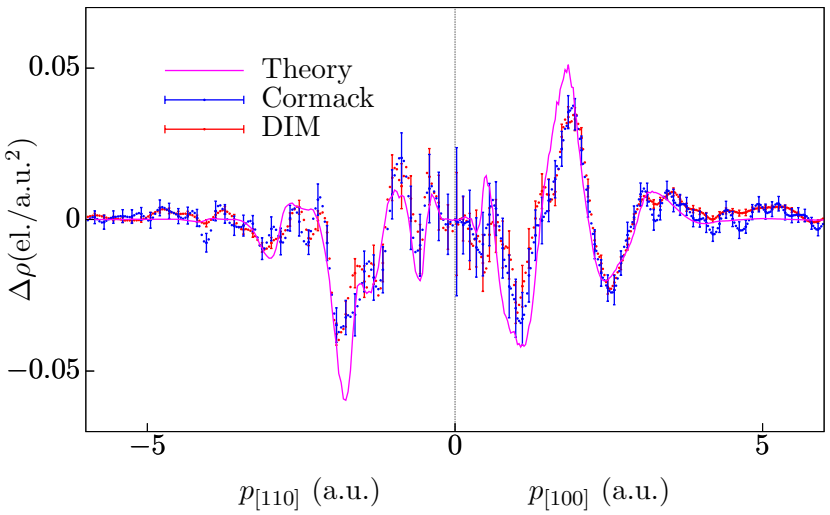

Figure 6.4 (a) 2D radial anisotropy of the projected EMD calculated by DFT (left), reconstructed from ten 1D Compton profiles by DIM (top right) and by CM (bottom right). The theoretical spectrum was convolved with a two-dimensional Gaussian accounting for the experimental resolution. (b) Cut through the 2D radial anisotropy along the red path (1→2→3) shown in (a).

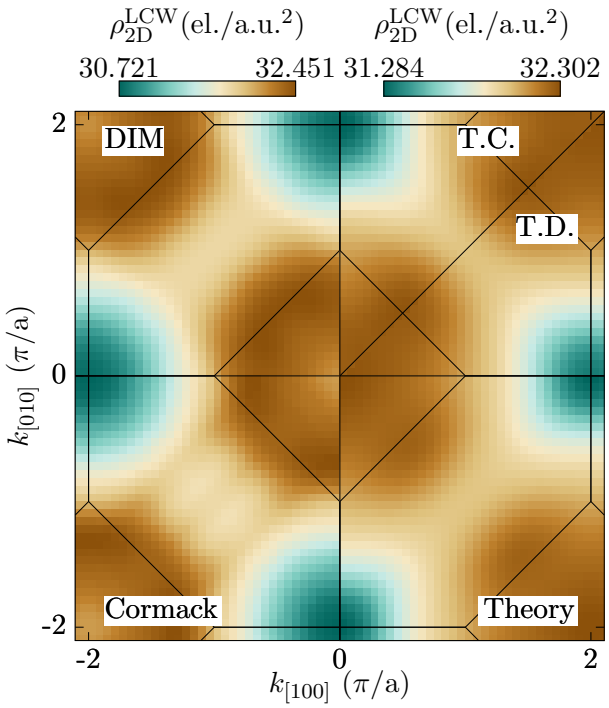

Figure 6.5 2D LCW of the experimental and theoretical 2D-EMD: Reconstructed experimental spectrum by DIM (top left) and by CM (bottom left); theoretical EMD (bottom right); reconstruction from theoretical 1D Compton profiles by CM (top right, T.C.) and DIM (top right, T.D.). The theoretical data in the right half of the plot was convolved with a two-dimensional Gaussian accounting for the experimental resolution, before back-folding.

smaller variation in the radial direction than the tangential direction. Figure 6.4(b) shows a cut through the 2D anisotropy along high-symmetry directions according to the red path (1→2→3) shown in (a). This cut highlights more clearly the good agreement of both reconstructions within the error bars.

The LCW back-folded data, presented in figure 6.5, is almost identical for both reconstruction methods. One interesting difference between theory (bottom right) and experiment (left) is the intensity distribution around the center (projected Γ-point), where the theory shows a high intensity while both reconstructions give a clear dip. The possibility of this behavior being an artifact of the reconstruction was excluded by reconstructing the 2D LCW from theoretically calculated 1D Compton profiles (top right), which did not show a dip in the center of the LCW. Typically, theoretical calculations using the LDA or GGA are not fully capable of reproducing all parts of the FS equally well [HLJD21]. From our FS calculations (figure 6.1), we numerically extracted multiple dHvA orbits using the SKEAF code [RJ12]. Most of the orbits agree

well with dHvA measurements [DCC$^+$81] and the area of the so-called ϵ-orbit, which originates from a heavy electron band with an effective cyclotron mass of $12.5\,m_e$ agrees with our calculations within 1 % [VHG99]. However, the area of the so-called α-orbit is about 11.5 % smaller in DFT in comparison to the dHvA experiment [DCC$^+$81]. As this orbit also originates from a heavy band, such differences might be expected as a slight change in the position of the band relative to the Fermi energy and can hence strongly influence the FS created by the band. To get a feeling of the size of the FS tube corresponding to the α-orbit in our Compton experiment, we calculated the first derivatives of cuts through the LCW along the Γ-X and Γ-K directions. Both curves indicate a hole pocket at the projected X-points which is larger than expected from theory. Therefore, we attribute the dip in the experimental LCW at the center of the projected Brillouin zone (where the X-points also projects) to this difference between theory and experiment.

To model the statistical error propagation of the reconstruction algorithms, LCW error maps were calculated [KSSC05]. For this, one hundred Compton profiles were simulated for each measured direction by adding statistical noise with the same error distribution as the experiment. From those one hundred data sets, reconstructions were performed with both methods and the standard deviation for each reconstructed pixel was calculated as shown in the error maps (figure 6.6). For the reconstruction using the DIM exhibits this standard deviation is smaller than that from the Cormack method over the whole projected Brillouin zone. As has been observed before, the error is largest at the points and along lines of highest symmetry, particularly at the center of the projected Brillouin zone. In the DIM reconstruction, the errors along the projected $\Gamma - L - \Gamma$ and $X - L - X$ directions are of a similar magnitude, while the error along the $X - L - X$ directions is strongly reduced in the Cormack reconstruction.

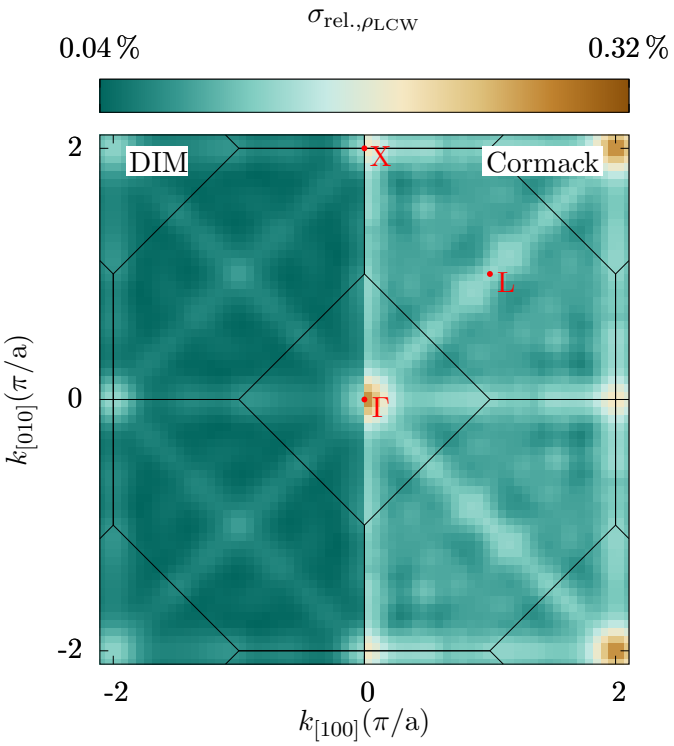

Figure 6.6 2D error map of the two reconstruction approaches DIM (left) and Cormack (right) calculated from 100 reconstructions from noisy theory data. The color bar indicates the percentage error per pixel. The positions of the projected high-symmetry Γ, L, and X points are indicated.

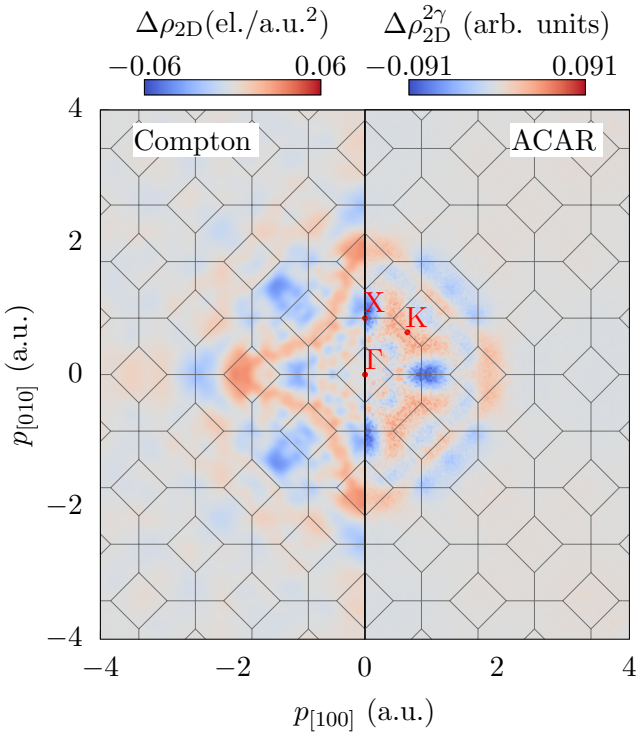

Figure 6.7 2D radial anisotropy of the EMD reconstructed (DIM) from ten 1D Compton spectra (left) and the corresponding 2D projection obtained by 2D-ACAR (right). Both spectra were normalized to the corresponding electron density of the EMD before calculating the radial anisotropy. The positions of the projected high-symmetry Γ, K, and X points are indicated.

6.3.3 Comparison of ACAR and Compton (in 2D and 1D)

Now, we compare the results of ACAR and Compton using the new DIM algorithm. Figure 6.7 shows the experimental radial anisotropy of the DIM-reconstructed 2D-EMD (from Compton) and the 2D-TPMD (from 2D-ACAR). The labelled Γ, K, and X points are the projected positions of the high symmetry points of the three-dimensional face-centered cubic Brillouin zone. The 2D-ACAR shows significantly larger anisotropy, especially at low momenta, compared to Compton scattering (note the scale of the colorbar). This behavior is expected because the positron wavefunction overlaps strongly with that of the delocalized electrons (particularly with electrons at the FS), but overlaps only very weakly with that of the most tightly bound states. Most of the main features like the low intensity pocket around X and the butterfly shaped high intensity around the K-point are revealed by both techniques. However, obvious differences are also present, particularly at higher momenta, e. g. for $|\boldsymbol{p}| > 2$ a.u., where 2D-ACAR hardly reveals any anisotropy, again due to the

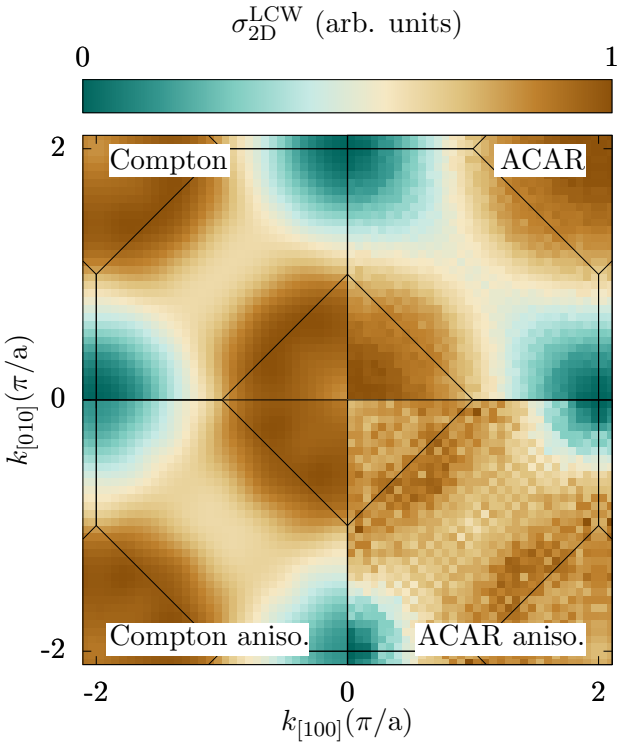

Figure 6.8 2D-LCW of the reconstructed (DIM) Compton spectrum (top left) and the 2D-ACAR spectrum (top right). 2D-LCW calculated from the radial anisotropies of the reconstructed (DIM) Compton spectrum (bottom left) and the 2D-ACAR spectrum (bottom right).

small overlap of the wavefunctions of positrons and (core) electrons.

For a further comparison, the spectra are back-folded into the first Brillouin zone [LCW73]. The Compton LCW is normalized, so that the integral over one Brillouin zone equals 18 valence electrons and a constant ($\boldsymbol{k}$-independent) contribution of 28 core electrons is added, since Compton scattering probes every electron equally. Although this normalization is not technically valid for the TPMD measured by 2D-ACAR, the LCW is also normalized in the same way for easier comparison. In the upper half of Fig. 6.8, the LCWs of the experimental 2D-EMD and 2D-TPMD are shown on the left and right side, respectively. In contrast to the Compton experiment, the 2D-ACAR spectrum does not show a dip in the center of the Brillouin zone. This is not expected from positron enhancement effects because the difference between the theoretical calculation including positron enhancement and the calculation using the IPM suggests a reduced intensity at the projected Γ-point (see figure 6.9). We attribute the increased LCW back-folded density at low momenta to a contribution of positrons annihilating in vacancy-type defects. As shown

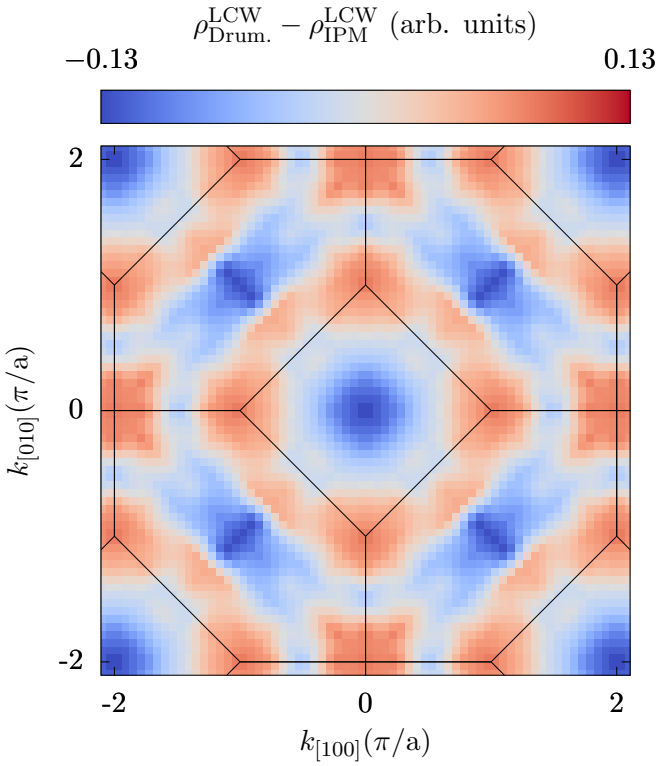

Figure 6.9 Difference between the TPMD calculation including enhancement (Drummond model [DLRNP11]) and the IPM calculation in the reduced zone scheme.

by Dugdale and Laverock [DL14], the FS information can still be recovered by instead back-folding the radial anisotropy to the first Brillouin zone instead of calculating the LCW from the full density. This is shown for Compton data (left) and 2D-ACAR data (right) in the lower half of Fig. 6.8. As depicted, the LCW of the back-folded anisotropies agree very well over the whole Brillouin zone, including the zone center.

To get a more quantitative comparison between 2D-ACAR and Compton scattering, 1D projections of the the 2D-ACAR measurements along the Γ-K and Γ-X directions are retrieved by summation of the [011] projection along the horizontal and vertical measurement directions, respectively. In order to visualize details of anisotropic features of the distributions more clearly, the directional differences of the two 1D profiles are calculated. The results are shown in figure 6.10 for Compton and 2D-ACAR measurements as well as for the EMD and TPMD (IPM and including enhancement) calculations. First, comparing the results of the DFT calculations, as expected, we can see significant differences between EMD and TPMD, which can be attributed to the influence of the positron. The same holds true if we compare the ACAR and Compton

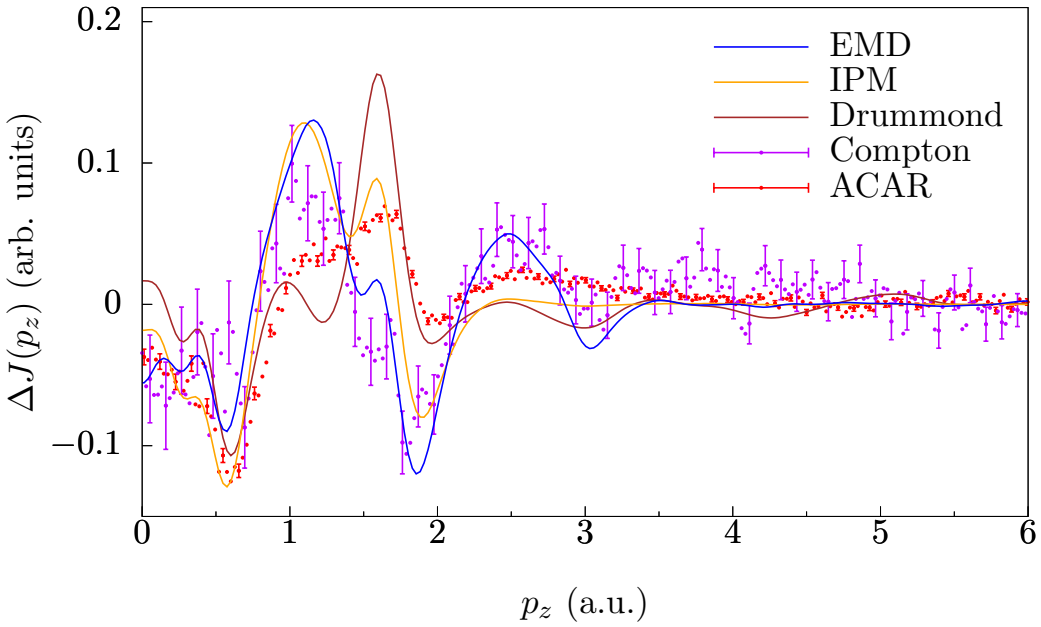

Figure 6.10 Directional differences between 1D projections along Γ-X and Γ-K of the Compton and 2D-ACAR experiments (purple and red points, respectively), together with the calculated (lines) EMD (blue) and TPMD, calculated with (brown) and without (yellow) positron enhancement. The calculated profiles are convolved with Gaussian functions accounting for their respective experimental resolutions. For every fourth experimental data point, error bars show the statistical error of one standard deviation.

measurements, especially in the region from 1 to 2.2 a.u.. Furthermore, we can clearly see an enhancement effect on the TPMD calculations by comparing the results from the IPM and the calculation using the Drummond enhancement model. Comparing experimental data to theory we see that the Compton experiment is very well described by the calculated EMD. The 2D-ACAR data is not equally well described by either of the two TPMD models over the whole momentum range. At low momenta and around 1.6 a.u. the data is better described by the IPM, while, at other momenta, the Drummond model seems to deliver the better approximation. This clearly shows how strongly TPMD calculations and 2D-ACAR experiments are influenced by positron wave function and enhancement effects that make theoretical modelling of positron spectra more difficult compared to Compton profile calculations.

6.4 Conclusion

We performed Compton scattering and 2D-ACAR measurements on a high-quality Pd single crystal in order to compare the results from both experiments and reveal the influence of positron probing effects on the measured electronic structure. In order to allow a reliable comparison of the 2D projections of the TPMD from 2D-ACAR with 1D Compton profiles, a new, direct reconstruction technique was developed for the 1D-to-2D reconstruction of Compton data. Our DIM algorithm uses the direct inversion of linear matrices and is a general case of Thikonov regularization to solve the reconstruction problem. The results from the DIM agree well with a reconstruction by the well-known CM method. Even if the new approach is computationally more demanding than the CM, with modest computational power, the DIM algorithm still enables an efficient method to get a high quality reconstruction of the 2D electron momentum density.

Differences between theory and experiment in the LCW back-folded spectra support earlier findings by dHvA experiments that the DFT calculations underestimate the size of the so called α-orbit.

In order to analyze the influence of positron probing effects on the determination of the electronic structure, first-principles calculations of the EMD and TPMD were performed. For the TPMD, clear differences between both models (namely, the IPM and the Drummond enhancement model) can be found, however, neither are fully capable of describing the experimental data over the whole momentum range.

A huge advantage of 2D-ACAR is the direct measurement of a 2D projection of the TPMD compared to a 1D projection of the EMD measured in Compton scattering. This drawback can be compensated by reconstruction of the 2D information from 1D Compton profiles along different directions. Although in this work an efficient reconstruction technique was used, the data treatment including the reconstruction of the 2D spectrum needed in Compton scattering is much more demanding compared to 2D-ACAR. Besides the fact that Compton scattering is practically insensitive to vacancy-type defects, the biggest advantage of Compton scattering is the much simpler calculation of theoretical spectra, compared to the calculation of 2D-ACAR spectra in which enhancement and positron wave function effects, which are difficult to calculate, might play an important role. This can be clearly seen in the directional differences

between the EMD and TPMD calculations, as well as the convincing agreement between EMD and Compton measurements.

Chapter 7

Fermi Surface Modeling of Light-Rare-Earth Hexaborides

The experimental work of the study presented in this chapter was conducted by the author while the theoretical calculations were done by collaborators from the University of Halle-Wittenberg, University of Bristol and University of Augsburg. The main part of this chapter was recently published elsewhere [KLB+21].

The rare-earth hexaborides (RB_6, R=La, Ce, Pr, Nd, and Sm) provide an interesting subject for experimental and theoretical studies because of a wide variety of macroscopic properties. Within those compounds, LaB_6 is considered as the reference non-f-electron system, CeB_6 is a Kondo lattice - heavy fermion system, whereas PrB_6 and NdB_6 are local-moment magnetically ordered metals. Among these compounds, SmB_6 is considered to be a "topological Kondo insulator" [DSGC10] due to the narrow hybridization band gap that opens at the Fermi level. In Kondo materials [Kon64], which are materials showing a resistance minimum at low temperatures, the width of this hybridization band gap is described by the Kondo temperature T_K. All of those features of the rare-earth hexaborides are usually ascribed to the particular role played by their $4f$-electrons [DFO+97, Ris00]. For the theoretical modeling of such systems, the unfilled $4f$-states are a challenging problem for an accurate description of the electronic structure of rare-earth compounds. Usually the $4f$ levels are treated as core states even if they often overlap with the non-$4f$ broad bands and form narrow resonances. A proper description, however, requires inclusion of the $4f$-states in valence bands where these states are also subjected to a strong on-site Coulomb repulsion. A simple theory that can capture this strong on-site Coulomb repulsion for $4f$ orbitals at the mean-field level is the

LDA(+U) approach [AAL97]. Another important ingredient in the physics of the rare-earth compounds is the presence of significant spin-orbit coupling, which fortunately can be included on an equal footing with strong on-site Coulomb interactions, which is modeled by the so-called Hubbard U. The recent theoretical models beyond the LDA, such as the GW method, which approximates the self-energy of a many-body system by a product of the single particle Green's function (G) and the screened Coulomb interaction W [AG98], or dynamic electronic correlations such as DMFT [KV04, KSH$^+$06], however, are difficult to use in case of multiorbitals (like $4f$) and strong spin-orbit coupling.

In DFT calculations for SmB_6 [CDC$^+$15] topologically non trivial phases were found, which can be ascribed to the band-character inversion due to the spin-orbit coupling between the rare-earth $4f/5d$ states situated around the Fermi level E_F. This can be understood as in general, some of the $4f$-bands of the rare-earth elements are located close to E_F, and are crossed by the more dispersive $5d$ band. The finite spin-orbit coupling splits these crossings and opens a gap. Also in other rare-earth hexaborides it was searched for such effects [HJ20]. The effects due to a finite Hubbard interaction, U, were also investigated for Sm-$4f$ and it was found that the topological features in SmB_6 are insensitive to the values of on-site Coulomb interaction. The latter, however, plays a crucial role in the other isostructural hexaborides [HJ20].

This study focuses on the electronic properties of two members of the RB_6 family, namely LaB_6 and CeB_6. Although the f-shell of La is empty while Ce has a single f-electron and CeB_6 exhibits a far richer phase diagram than LaB_6, undergoing several different magnetic phase transitions, dHvA measurements [JvRC$^+$87] yielded similar FS features for both CeB_6 and LaB_6. The FS of CeB_6 consists of large "ellipsoid" pockets around the X points of the BZ, whereas the states around the zone center (Γ-point) are shifted away by band-renormalization effects leading to a hole pocket [NAB$^+$15]. The first-principles calculations agree with the experimental results around the X-points but fail to capture the strongly renormalized electronic states around the Γ-point [NAB$^+$15]. The dHvA measurements [JvRC$^+$87] at temperatures $T < T_K$ below the Kondo temperature can be brought into accordance with a model in which f-electrons do not contribute to the Fermi volume. Above the Kondo temperature $T > T_K$, in the paramagnetic phase, dHvA measurements and 2D-ACAR results were also in agreement in the case of CeB_6 [JvRC$^+$87].

Results of the 2D-ACAR experiments on LaB_6 were reported earlier in the literature [BAD$^+$97, BFD$^+$97], where the analysis in terms of the back-folded momentum densities were conducted. 3D reconstruction of the FSs using 2D-ACAR projections was also reported [BMKS$^+$01], and contrary to the electronic structure calculations, the strong hybridization between B-p and La-d states (f-states are unoccupied) that produced additional FS sheets was not detected in the experiment.

The two compounds, LaB_6 and CeB_6, are investigated with 2D-ACAR spectroscopy and first-principles DFT calculations [HK64, JG89, Koh99, Jon15]. The experimentally determined and theoretically calculated momentum densities of LaB_6 are analyzed by means of radial anisotropies in the extended momentum $\boldsymbol{p}$ space Furthermore, the data was LCW backfolded into the crystal-momentum $\boldsymbol{k}$ space to identify the different FS features. Additionally, possible similarities between the theoretical spectra with the isostructural CeB_6 are also discussed. For the CeB_6 compound, in the absence of recent experimental measurements, the effects of the different U values of the Hubbard interaction and diverse double-counting schemes of the LDA+U method are studied theoretically.

7.1 Methods

7.1.1 Experimental Details

The crystal structures (see figure 7.1) of RB_6 belong to the simple cubic CsCl structure type ($Pm\bar{3}m$), with lattice constant $a = 4.1569$ Å and $a = 4.1391$ Å, for LaB_6 and CeB_6, respectively. The rare-earth atoms occupy the corner of the unit cell, corresponding to the 1a(0,0,0) Wyckoff site, whereas the B atoms are located at the octahedral sites in the body-centered position at the $6f(0.5, 0.5, z)$ Wyckoff sites, where z is 0.2011 for CeB_6 [T$\bar{\text{O}}$02] and 0.1996 for LaB_6 [CAI$^+$04].

The LaB_6 sample used in the 2D-ACAR experiment was a cuboid-shaped high-quality single crystal of $10 \times 5 \times 2\text{mm}^3$ size provided by N. Shitsevalova of the National Academy of Sciences of Ukraine. It was grown by the vertical crucible-free inductive floating zone melting in argon gas atmosphere. The grown crystal was characterized by Laue backscattering, optical spectral analysis, X-ray diffraction, and density measurements. The surfaces of the plate were

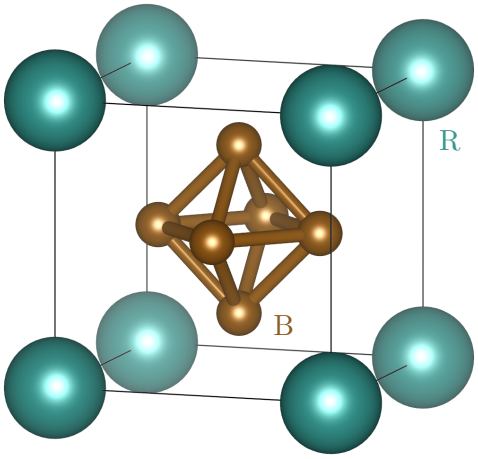

Figure 7.1 Crystal structure of the rare-earth hexaborides RB_6. The rare-earth atoms are shown in blue; the boron atoms at the octahedral sites in brown (created using *VESTA* [MI11]).

polished with diamond powder. More details on the preparation are given in the appendix. The 2D-ACAR measurements were carried out at 15 K to reduce the contribution of the thermal motion of the positron and the positrons were guided onto the sample by a magnetic field of 1.2 T at the sample position. 2D-ACAR projections along the high-symmetry [110], [001], and [111] directions within the (110) plane were measured and for each spectrum, more than 9×10^7 events were collected.

7.1.2 Electronic Structure Calculation

Electronic structure calculations were carried out by our collaborators (see above) using the ELKcode [DSN+], which is an all-electron full-potential linearized augmented plane-wave (LAPW) code for determining the properties of crystalline solids.

TPMD Calculations

For the calculations of the TPMDs the valence electron configuration for the rare-earth atoms (La=Ce) was $6s6p5d4f$, whereas the valence electrons of B were located in the $2s$ and $2p$ orbitals. The self-consistent calculations were carried out using the LDA exchange-correlation functional parameterized by Perdew and Wang [PW92]. The k-summations were conducted using the

tetrahedron method, with a $20 \times 20 \times 20$ k-mesh in the irreducible part of the BZ, and convergence was achieved in total energy with an accuracy of better than 1×10^{-5} Ry. For the detailed FS calculations, a significantly larger $80 \times 80 \times 80$ k-mesh was used.

The DFT can be generalized to electron-positron systems by including the positron density in the form of the two-component DFT [BanN86, PN94], where the positron was considered to be thermalized and described by a state with $\boldsymbol{p}_p = 0$ with s-type symmetry at the bottom of the positronic band. The photons resulting from the electron-positron annihilation carried the momentum of the annihilated pair, up to a reciprocal lattice vector, reflecting the fact that the annihilation took place in a crystal. Hence, an electron with a transverse wave vector k contributes to the spin-resolved TPMD, $\rho^{2\gamma}(\boldsymbol{p})$, not only at $\boldsymbol{p} = \boldsymbol{k}$ (normal process) but also at $\boldsymbol{p} = \boldsymbol{k} + \boldsymbol{G}$, with $\boldsymbol{G}$ being a vector of the reciprocal lattice (Umklapp process). In the LDA($+U$) framework (details below), the TPMD $\rho(\boldsymbol{p})$ was computed directly with the spin-resolved versions of equations 3.33 and 4.3. The 2D-ACAR spectra were calculated according to the method described in the study by Ernsting et al. [EBH$^+$14]. These TPMDs were calculated to a maximum momentum of 6 a.u. and the enhancement factor $\gamma(x)$ (see chapter 3.3.6) accounted for the electron-positron correlations. Here two approaches for the treatment of the enhancement were used. Firstly, the IPM ($\gamma(x) = 1$) and secondly the Drummond parametrization [DLRPN10, DLRNP11], which considers the momentum and energy dependencies and a separate treatment of f and d states in comparison with the s and p states.

LDA$+U$ Calculations

Among the most frequently used techniques to include short-range Coulomb interactions between the electrons in the frame-work of DFT are the self-interaction-corrected local-spin-density approximation (SIC-LSDA) [PZ81] and LDA$+U$ [AAL97]. In particular, LDA$+U$ calculations are computationally less demanding and hence can be easily used for systems with unit cells consisting of a considerable number of atoms. Therefore, in this study the rationally invariant formulation of the Coulomb interaction between the valence electrons was used [AAL97]. Furthermore, its flexibility allows a systematic study of effects of the on-site repulsion U, on the ground-state properties such as equilibrium lattice parameter, magnetic moment, and - in the current work - 2D-ACAR spectra. The orbital-dependent LDA$+U$ functional used in the present work is given by [AAL97]

$$E_{LDA+U} = E_{LDA} + \frac{U-J}{2} \sum_{\sigma} \left[tr\rho^{\sigma} - tr(\rho^{\sigma}\rho^{\sigma}) \right]. \tag{7.1}$$

Here, ρ^{σ} is the density matrix for the f-states and should not be confused with the TPMD. U and J are the local Coulomb and exchange Hund's parameters.

The lack of a diagrammatic expansion of the DFT total energy makes it difficult to model the effect of the local Coulomb interactions beyond the effects already captured by the exchange-correlation functionals. Here possible double counting of such effects have to be considered. Therefore, several schemes have been proposed for different kinds of materials, to avoid this double counting. One of them is the mean-field approximation to the Hubbard correction, the so-called fully localized limit (FLL). This formulation of the double-counting term mimics an expansion of the electronic energy around the strongly localized limit, by considering each localized (e. g. atomic) orbital as either full or completely empty, and thus tends to work quite well for strongly correlated materials with localized orbitals. However, for metals or "weakly correlated" materials for example, the excessive stabilization of occupied states due to the "$+U$" potential may lead to unphysical results. In weakly correlated metals like FeAl, e. g., this can lead to the enhancement of the Stoner factor [PMCL03]. A different double-counting scheme, the around mean-field (AMF), was introduced in the study by Czyzyk et al. [CdzS94] and further developed in the study by Petukhov et al. [PMCL03]. In the present study, the AMF double-counting scheme failed to produce the correct position of the $4f$ bands; therefore, FLL double counting was used in all presented results.

7.2 Results and Discussion

7.2.1 LaB_6: Experiment and Theory

To compare experimental and theoretical data on LaB_6 in the p-space, the radial anisotropy $\rho_{\text{aniso}}(p_x, p_y)$ is calculated, to emphasize the spectral contribution from electrons near the Fermi level. Figure 7.2 shows the radial anisotropy for all three measured projections (from left to right (110),(001), and (111)) in the upper half and the corresponding theoretical calculations in the lower half of the plots. The calculated results are for the momentum distributions with IPM (left) and Drummond enhancement (right). As the experimental

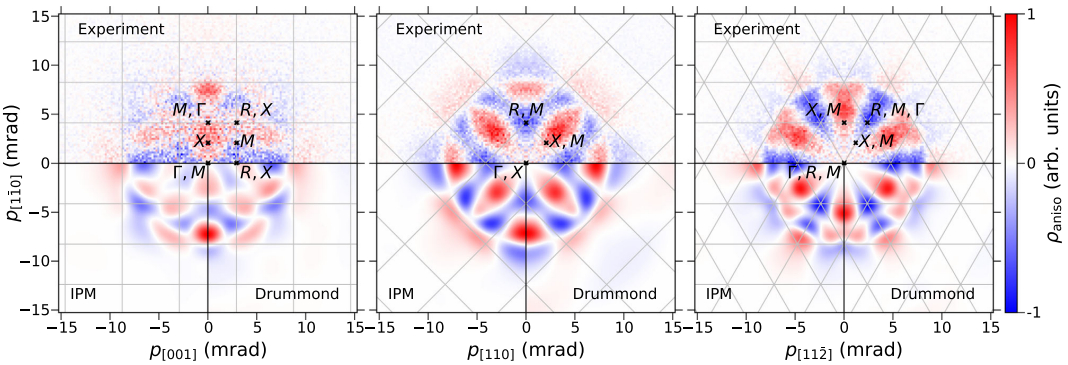

Figure 7.2 Radial anisotropy of measured and symmetrized LaB_6 ACAR spectra (top) and theoretical spectra calculated in the IPM (bottom left) and with the Drummond enhancement (bottom right). The spectra from first-principle calculations are convolved with a Gaussian accounting for the experimental resolution of 0.60 mrad. The borders of the projected first BZ (gray lines) in a repeated zone scheme are shown in all plots. From left to right, (110), (001), and (111) high-symmetry projections.

data are symmetrized according to the crystal symmetry, the theoretical data are convolved with an isotropic Gaussian with an effective resolution of $\sigma_{\mathrm{exp}} = 0.60$ mrad calculated as the quadratic mean of the experimental resolutions given in section 4.1.3.

Overall, a very good agreement between theory and experiment was obtained. The theoretical calculations were able to reproduce the dominant features of the experimental data, which is especially fulfilled for the four-fold and sixfold symmetric projections. Some minor differences can be seen in the (110) projection. Particularly, the weight distribution in the region between -5 to 5 mrad on both axes shows a significant departure between the theory and experiment. However, the high-intensity positive signal along $[1\bar{1}0]$ direction at about 8 mrad is well reproduced. The better agreement between the theory and the experiment for the (001) and (111) projections can be attributed to the higher point symmetry of these directions. In all experimental projections, the anisotropy profiles are slightly stretched out within the plane. Even if the differences between the IPM and Drummond model are marginal, similar behavior is also observed when the Drummond enhancement is included in the computation. However, the radial expansion of the profile is not sufficient to match the observed *stretching* in the experimental measurement.

Figure 7.3 shows the LCW back-folded data, experiments as well as theory, and is organized according to the structure of figure 7.2. The top part of each plot shows the k-space experimental 2D-ACAR spectrum, whereas the bottom

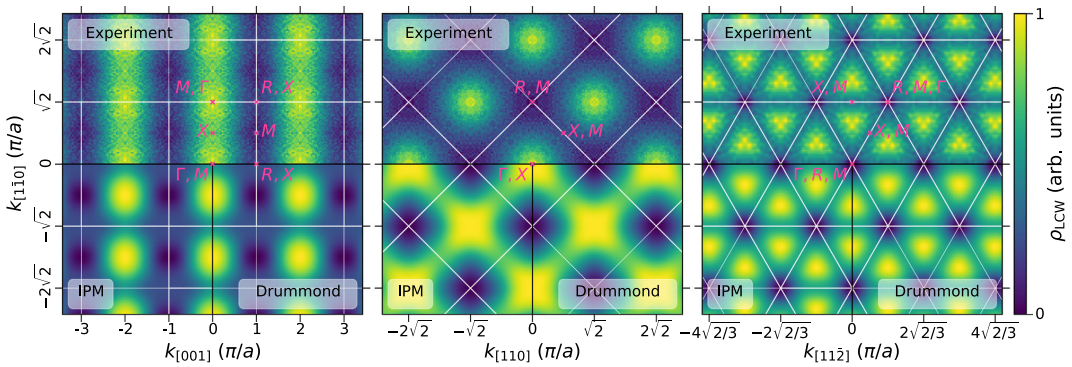

Figure 7.3 LaB_6 LCW back-folded k-space density of the ACAR measurements (top) and the theoretical calculations in the IPM (bottom left) and the Drummond model (bottom right). The spectra from first-principle calculations are convolved with a Gaussian accounting for the experimental resolution of 0.60 mrad. The borders of the projected first BZ (white lines) in a repeated zone scheme are shown in all plots. From left to right, (110), (001), and (111) high-symmetry projections.

part is split between the calculated results using IPM (left) and Drummond enhancement (right), convolved with the experimental resolution function.

The measured and calculated LCW back-folded spectra show an overall good agreement. The (001) and (111) projections show the expected features of the FS topology (see figure 7.4). In the (111) projection, the sixfold rose structure around the Γ-point becomes apparent. As expected from the calculated FS, there is no density at the Γ- and R-point in the BZ. Note that one can not see the hole space around the Γ-point in the (001) projection, as it is covered by the "ellipsoids" along the [001] direction. While the theoretical calculations explicitly reproduce the "ellipsoid" structure in (110) projection, the experimental (110) projection shows stripes along $[1\bar{1}0]$ direction. The latter can be also attributed to the observed substantial discrepancies between the theory and experiment in the radial anisotropy (see figure 7.2).

7.2.2 Fermi Surface Modeling

The FS of LaB_6 is shown in figure 7.4 in the simple cubic BZ where the high-symmetry points are $\Gamma \equiv [0,0,0]$, $X \equiv [1/2,0,0]$, $M \equiv [1/2,1/2,0]$, and $R \equiv [1/2,1/2,1/2]$. The FS of LaB_6 consists of a set of equivalent "ellipsoids" centered at the X-points and connected by necks which intersect along $\Sigma\,(\Gamma - M)$ direction. In the panels (b) and (c) in figure 7.4, we show a cross section in the $\Gamma - X - M$-plane ($k_{[100]} = 0$ plane). The DFT (LDA) FS calculation for SmB_6 with a downward shift of the Fermi energy is presented in the

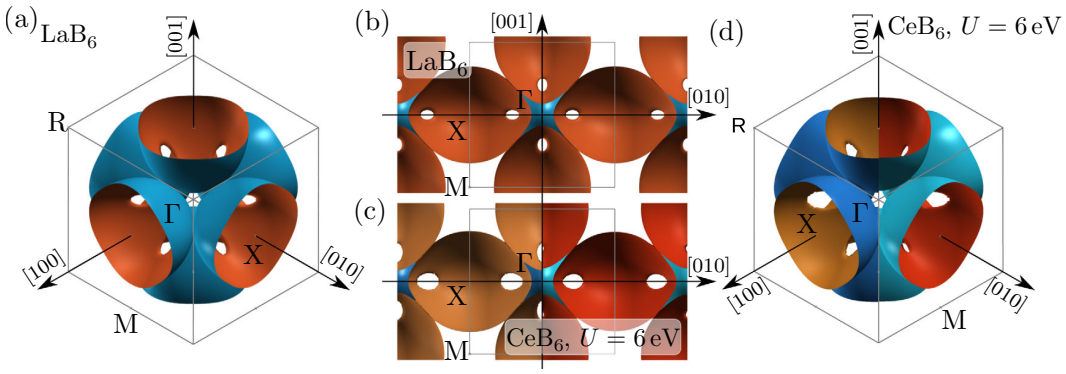

Figure 7.4 FS in the first BZ from first-principle LDA calculations for LaB_6 (a) and LDA+U calculation with $U = 6\,\text{eV}$ for CeB_6 (d). $\Gamma - X - M$ cross section ([010]-[001] cut) of FS for LaB_6 (b) and CeB_6 (c), respectively. On plots (c) and (d), the FS sheets of CeB_6 for two different spin projections are depicted in the left and the right half of the plots, in blue/orange and deep sky blue/red colors, respectively. The borders of the first BZ (gray lines) and high-symmetry points (Γ, X, M, and R) are shown on all plots as well.

study by Tan et al. [THZ+15] and has a FS similar to that of LaB_6, as shown in figure 7.4. The angular variations of the dHvA frequencies and the disappearance of oscillations in some angular regions have been recently discussed for both SmB_6 and LaB_6 [THZ+15]. These quantum oscillation frequencies identify the so-called $\alpha, \gamma, \varepsilon$ branches associated with FS regions visible in the $\Gamma - X - M$ plane, see figure 7.4. The α-branches were associated with the ellipsoids centered at the X-point. As one can see, the nearest-neighbour ellipsoid FS pieces touch along the $\Gamma - M$ line and connect through the small distorted circular shape neck, building up a multiple connected FS. Both the γ and ε-orbits are hole-like orbits and are centered around M-point and Γ-point, respectively. According to the dHvA frequencies the angular region for the hole-like γ- and ε-orbits is significantly larger in SmB_6 than in LaB_6 which may be the cause of different physical properties of these two compounds. From our calculations we can compare linear dimensions of the FS features to both previous computations and the present experimental data. The corresponding values are 0.848, 0.668, and 0.624 for the $X - \Gamma$, $X - M$, and $X - R$ directions, respectively, as a fraction of the BZ size. Our results agree with the previous results reported in the literature [BMKS+01].

In a next step, the FS linear dimension are determined from the experimental data [BMKS+01, LWC16]. Taking into account a finite experimental resolution, the electron-momentum density is modeled with prolate ellipsoids

with equatorial radius R_{eq} and polar radius R_{pl}, centered at the X points in reciprocal space and pointing toward the neighbouring Γ points:

$$F\left(\boldsymbol{k}; R_{\mathrm{eq}}, R_{\mathrm{pl}}\right) = \sum_{\boldsymbol{G}} \sum_{\boldsymbol{b_i}} \Theta\left(1 - \frac{|(\boldsymbol{k}-\boldsymbol{G})\times\boldsymbol{b}_i|^2}{R_{\mathrm{eq}}^2|\boldsymbol{b}_i^2|} - \frac{|(\boldsymbol{k}-\boldsymbol{G}-\boldsymbol{b}_i/2)\cdot\boldsymbol{b}_i|^2}{R_{\mathrm{pl}}^2|\boldsymbol{b}_i^2|}\right). \tag{7.2}$$

Here, $\Theta(\cdot)$ is the Heaviside step function and summation is over reciprocal lattice vectors $\boldsymbol{G}$ and reciprocal primitive vectors $\boldsymbol{b}_i \in \boldsymbol{b}_{[100]}, \boldsymbol{b}_{[010]}, \boldsymbol{b}_{[001]}$. Adding a flat background TPMD due to fully occupied bands described by a third parameter F_{back}, projecting along the given direction and convolving with the anisotropic Gaussian kernel that models the experimental resolution, the resulting simulated projections are fitted to the correspondingly normalized LCW back-folded data for all measured projection directions by varying the three free parameters. From that $2R_{\mathrm{eq}} = 0.662 \pm 0.002$ and $2R_{\mathrm{pl}} = 0.952 \pm 0.002$ in units of the reciprocal lattice constant are obtained, where the reported uncertainties are statistical precision due to counting noise. The equatorial diameter R_{eq} agrees well with the calculated $X - M$ length of 0.668, whereas the length along the $X - \Gamma$ direction is about 12 % larger than the theoretically predicted value. This difference is attributed to positron wave-function and/or electron-positron correlation effects, as both are neglected in the LCW theorem [LCW73]. The determination of the equatorial diameter seems to be much less influenced by this effects as it is directly accessible in particular in the (001) projection, where the contrast between the filled ellipsoids and the background density is large. From figure 7.4 (a) it should be clear that there is no projection direction that would afford an unobstructed view on the polar termination of the ellipsoids. Thus, a larger band weight of the conduction and/or core bands toward Γ would necessarily result in an overestimated R_{pl}.

As the $X - M - R$ cross section of the FS shows fourfold deviations from circular symmetry, the model was extended to an ellipsoid cross section corresponding to a "squircle" to detect such deviations from a circle. However, this modification worsened the agreement between model and experimental data. One explanation would be, that either a better experimental resolution would be required to detect those deviations or contradicting the theoretical prediction the deviation from a circular cross section is smaller than predicted.

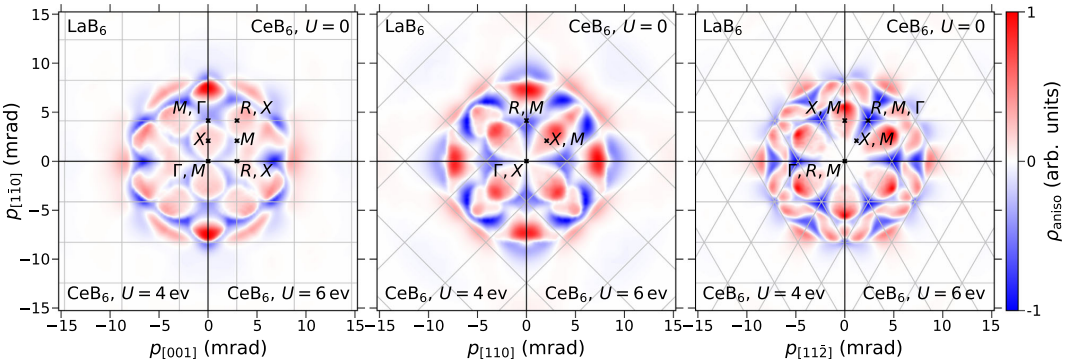

Figure 7.5 Unconvolved radial anisotropy of the calculated ACAR spectra for LaB_6 (upper left) and CeB_6 for $U = 0$ (upper right), $U = 4\,\text{eV}$ (bottom left), and $U = 6\,\text{eV}$ (bottom right). Results correspond to LDA (LaB_6 and CeB_6 $U = 0$) and LDA+U (the rest) calculations with the Drummond parametrization of the electron-positron enhancement factor. The borders of the projected first BZ (gray lines) in the repeated zone scheme are shown in all plots. From left to right, (110), (001), and (111) high-symmetry projections.

7.2.3 CeB_6: Theory

This section on the theoretical calculations on CeB_6 is included in this work for the sake of completeness of our study on the rare-earth hexaborides. However, it should be clearly stated here that the main work on this section was performed by our collaborators from the theory side and corresponds basically to section 3.2 of the joint publication [KLB+21].

The DFT band structure of CeB_6 produces the manifold of Ce-4f orbitals in the close vicinity of the Fermi level. According to the experimental study of Neupane et al. [NAB+15], they have to be located at around 2 eV in the conduction band. Therefore, for the FLL limit, a reasonable parameter for the effective Coulomb interaction would be $U = 4\,\text{eV}$. The band structure and the density of states (not shown) in the ferromagnetic states are characterized by dispersive 5d- and flat 4f-bands along the $M - X - M$ and $X - \Gamma - X$ directions. The flat bands are purely built from Ce-4f states. The dispersive 5d band around the X-point is situated at 2 eV below E_F and touches the B-2p states at the Γ point. The position of these bands agrees fairly well with experiments [NAB+15, KHK+16].

Figure 7.5, presents the results for the calculated radial anisotropy of the 2D-ACAR spectra of LaB_6 compared with CeB_6. While the electronic calculations for LaB_6 were done using DFT only, for CeB_6, LDA+U was used. The value of U was varied between 0 and 6 eV. Here, the results for the

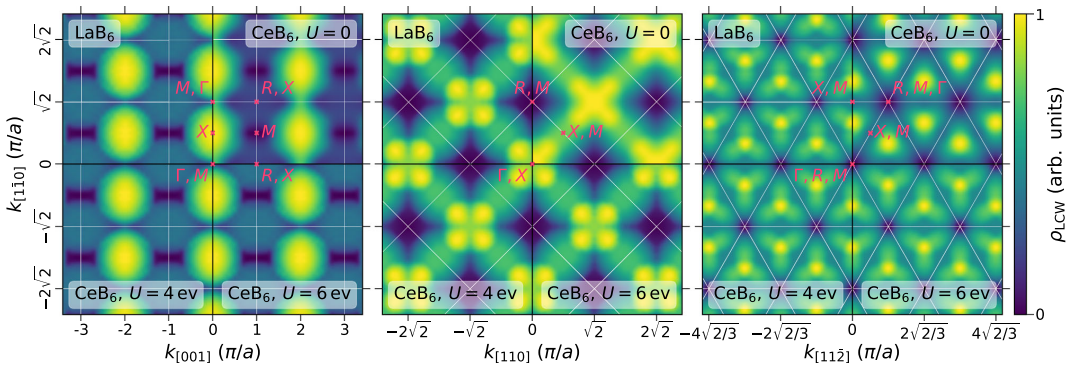

Figure 7.6 Unconvolved LCW back-folded k-space density of the calculated ACAR spectra for LaB_6 (upper left) and CeB_6 for $U = 0$ (upper right), $U = 4\,\text{eV}$ (bottom left), and $U = 6\,\text{eV}$ (bottom right). Results correspond to LDA (LaB_6 and CeB_6, $U = 0$) and LDA+U (the rest) calculations with the Drummond parametrization of the electron-positron enhancement factor. The borders of the projected first BZ (white lines) in the repeated zone scheme are shown in all plots. From left to right: (110), (001), and (111) high-symmetry projections.

extreme U values as well as an intermediate value of $U = 4\,\text{eV}$ are shown. The corresponding LCW back-folded $\boldsymbol{k}$-space densities are presented in figure 7.6. One can clearly see the similarity between LaB_6 and CeB_6, $U = 4\,\text{eV}$ and 6 eV spectra. This can be attributed to the on-site Coulomb repulsion (Hubbard U), which pushes unoccupied $4f$ manifold above the Fermi level and localizes the remaining filled $4f$-orbitals. The localization of a single electron in the $4f$-orbital causes the fully ferromagnetic ground state with the magnetic moment of about $1\,\mu_\text{B}$.

The shown spectra agree with the 2D-ACAR measurements presented in the study by Biasini et al. [BFD+97] for both structures (LaB_6 and CeB_6). In particular, the LaB_6 spectra are similar to CeB_6 for $U = 4\,\text{eV}$ and 6 eV in all shown high-symmetry projections. This can be explained by the localization of the $4f$-orbital position on the energy scale being pushed further below the E_F with increasing values of the Hubbard U parameter.

On the central panel of the LCW back-folded *unconvolved* data in figure 7.6 ((001) projection), the FS "ellipsoids" in [100] and [010] directions can be identified. The rounded-square cross sections of the same ellipsoids along the [001] direction also becomes apparent. This demonstrates that the high-resolution 2D-ACAR spectra can be used to deduce bulk FS features of the RB_6 family of compounds, which also includes $4f$-valence electron bands. However, the availability of high quality single crystals of the RB_6 family is a limiting factor.

7.3 Summary and Outlook

The study of the electronic structure of light rare-earth hexaborides was motivated by the unusual features found in this family of compounds. The definition of SmB_6 as a interaction-driven topological insulator [DSGC10, DXGC16], for example, is largely accepted.

The accuracy of any specific electronic structure model can in principle be assessed by comparing computed 2D-ACAR spectra with the corresponding measurements. Thus, in the present study, 2D-ACAR measurements on single-crystalline LaB_6 along three high-symmetry directions were performed. The experimental spectra in both p- and k-space were compared with LDA calculations and showed good agreement. In particular the quantitative results extracted from the experiment agree excellently with the corresponding theoretical values of the FS along $X - M$ and $X - R$ directions. In the $X - \Gamma$ direction, however, a larger value as theoretically predicted was determined, which is attributed to positron wave function and/or enhancement effects and to the fact that this direction is experimentally not directly accessible.

For another member of the rare-earth hexaboride class, the CeB_6 compound with $4f$-states in the valence band, in absence of the recent experimental measurements, the LDA+U method has been applied with different values of the Hubbard parameter U. The two compounds, LaB_6 and CeB_6, exhibit a metallic ground state, involving predominantly conduction electrons with low residual resistivity, and are characterized according to the DFT (LDA) calculations by a multiple-connected FS of distorted ellipsoids. Band structure calculations for these metallic compounds showed that these types of "ellipsoids" are universal FS features for these materials. In addition, the same types of calculations revealed similar features for SmB_6, when the Fermi level is shifted by hand from the computed position, which is in the gap, either up in the conduction bands or down in the valence bands [THZ+15].

The experimental and theoretical results show that the "ellipsoid" cross sections (α-orbit) and neck sizes increase and hence, γ and ε hole orbits of LaB_6 andCeB_6 are significantly reduced in size in comparison to SmB_6. This supports the findings from dHvA measurements that both, LaB_6 and CeB_6, are topological trivial but correlated materials. Therefore, as a complementary approach to the present LDA(+U) treatment of LaB_6 and CeB_6, DMFT, in which the role of the crystal electric field becomes apparent, as it is able to take

into account the full local correlation effects and its extensions also including intersite correlations, could be considered.

Finally it can be concluded, that the study of the RB_6 with respect to their electronic structure remains a highly interesting topic. Therefore, 2D-ACAR measurements on other compounds of the RB_6 family would be extremely beneficial, to benchmark theoretical findings against measured data. However, those measurements are strongly limited by the availability of high quality single crystals, as their growth in the millimeter range ($\varnothing > 5\,\mathrm{mm}$) is a very demanding process.

Chapter 8

Conclusion and Outlook

This work was focused on two experimental techniques namely 2D-ACAR and Compton scattering, which both measure the bulk electronic structure of materials in momentum space. Pd was measured by both techniques and a novel reconstruction algorithm was implemented in order to enable a profound comparison of the experimental results. Furthermore, the electronic structure of the rear earth hexaboride LaB_6 was measured by positron annihilation and compared to theoretical calculations. Towards the end of this project the sample holder of the 2D-ACAR experiment at TUM was upgraded in order to simplify the alignment of the experiment and to reach temperatures as low as 10 K.

Upgrade of the 2D-ACAR setup

The sample holder, which enables measurements below room temperature was replaced by an upgraded version. This new version significantly minimizes the effort for the alignment of the setup. Furthermore, it was shown by finite element method (FEM) simulations that temperatures in the range of 10 to 15 K should be reachable. Additionally, the angular positioning of the samples was simplified by allowing the rotation of the sample by a programmable interface.

Novel reconstruction algorithm

In order to compare results from Compton and 2D-ACAR measurements a novel reconstruction algorithm was implemented. The so-called direct inversion method (DIM) uses direct inversion of linear matrices and a general case of Thikonov like regularization functionals in order to reconstruct higher dimensional densities without iteration. This kind of functionals additionally enables

the reconstruction of only the anisotropic signals as both, positive and negative densities are allowed. This was shown to be highly beneficial in Compton scattering were contributions from core states (which are mostly isotropic) persist up to high momenta.

ACAR and Compton on Pd

In total ten Compton profiles and five 2D-ACAR projections have been measured for Pd and were compared to first-principle EMD and TPMD calculations. The comparison of 2D-ACAR and Compton scattering clearly revealed specific strengths and drawbacks of the two techniques. The data treatment in ACAR is straight forward in contrast to a comparably demanding multi step process in Compton scattering. On the other hand the theoretical calculation of Compton profiles is well established, while the exact influence of the positron probing effects on the EMD are still not completely understood. Still nowadays the existing enhancement models are not fully capable to theoretically predict the TPMD. However, the comparison of experimental results from both techniques and the corresponding theoretical calculations support the underestimation of the so called dHvA α-orbit by first principle calculations.

Rare Earth Hexaborides

Three high symmetry projections of LaB_6 were measured and compared to theoretical calculations. This comparison as well as theoretical LDA+U calculations on CeB_6 with varying electronic correlation strength, suggest that both LaB_6 and CeB_6, are topologically trivial but correlated metals. Therefore, it can be stated that future studies with DMFT, which takes into account the full local correlations starting from itinerant (valence) $4f$-states, will provide a suitable description of the electronic structure of the rare-earth hexaborides. Furthermore, the FS of LaB_6 was modeled from the measured data. The agreement to the theoretical prediction was excellent along the $X - M$ and $X - R$ directions. Along the $X - \Gamma$ direction the theoretical prediction underestimated the experimentally found length of the FS ellipsoid by around 12 %.

Future Work

Both experimental techniques, 2D-ACAR and Compton scattering have shown their great potential for the investigation of the electronic structure. The main

drawback of Compton scattering lies in the demanding data analysis process. For example, the saturation correction could highly benefit from changes in the standard experimental procedures. An option might be the determination of the saturation effect from measurements with varying beam intensities instead of measurements with different camera exposure times.

The main goal for the future development of the 2D-ACAR setup is the increase of the experimental resolution. This could be achieved by either increasing the detector-sample distance, improving the position resolution of the detectors or the reduction of the beam spot size. This would enable further in-detail investigation of the FS of materials like the rare-earth hexaborides. However, the availability of large high quality single crystals always remains a challenge.

Another important step to extend the usability of 2D-ACAR to the investigation of layered systems or the evolution of the electronic structure from surface to bulk will be the transfer to the experimental east hall and the connection to the high positron source NEPOMUC. This will open completely new applications for positron annihilation physics like the investigation of the electronic structure in thin films.

Appendix

Preparation of the LaB_6 single crystal

The following information on the preparation of the LaB_6 single crystal was provided by Natalya Shitsevalova from the National Academy of Sciences of Ukraine.

The LaB_6 single crystal was grown by a crucible-free inductive floating zone technique with a "Crystal-111A" special unit at the Institute for Problems of Materials Science, National Academy of Sciences of Ukraine (Kyiv). The source LaB_6 sintered rod for melting was prepared from the powder synthesized by a borothermal reduction of the lanthanum oxide at 1900 K in vacuum according to the routine solid-state reaction:

$$La_2O_3 + 15\,B \longrightarrow 2\,LaB_6 + 3\,BO\uparrow$$

A small excess of boron (3 wt%) was introduced into the initial charge to compensate for possible boron losses due to its high vapor pressure at the synthesis temperature. The basic substance content in the initial La_2O_3 oxide was 99.997 wt% and the content in the amorphous natural boron was higher than 99.5 wt%. The highly volatile impurities presented in boron were deleted during the synthesis procedure and, after that, in the zone melting process. In the grown crystal the amount of impurities does not exceed 1×10^{-2} wt% (except for rare earth) according to the optical spectral analysis. Rare earth impurities are determined by the purity of the initial lanthanum oxide, the total content of accompanying rare earth impurities did not exceed 2×10^{-3} wt%.

Zone melting is carried out in a closed chamber under the pressure of high-purity argon (volume fraction of argon is not less than 99.993 %). Preliminary the chamber is pumped out to 0.1333 Pa, then it is filled with argon up to 0.2 MPa and pumped out again, after which it is filled with argon to 0.1 MPa, and the melting process begins. The crystal was grown with one pass, the seed was fixed in the lower shaft and the feed rod in the upper shaft, and the

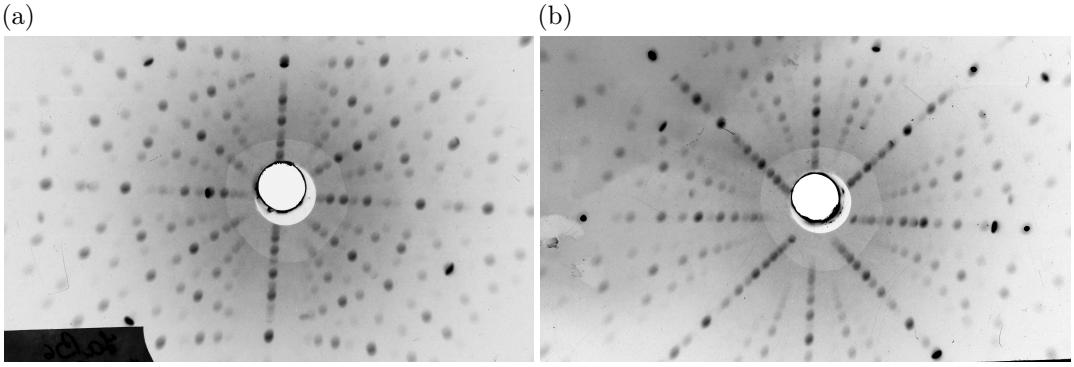

Figure A1 (a) LaB_6 Laue pattern of the [100] direction. The deviation from [100] is approximately 2°. (b) LaB_6 Laue pattern of the [110] direction. The deviation from [110] is about 1.5°.

linear velocities were 0.55 and 0.45 mm min^{-1} for the growing crystal and the feeding rod respectively. During the growth of the crystal, both the feed rod and the growing crystal rotated in opposite directions at rates of 8 and 2 rpm, respectively, which favored to a more uniform temperature distribution in the melt zone and equalization of the crystallization front, reducing thermal and mechanical stresses in the crystal. LaB_6 single crystal was grown with diameter of about 6 mm and 50 mm in length. The oriented experimental sample with dimensions 2 x 5 x 10 mm^3 was cut with an electric spark machine; its lateral surfaces are polished with diamond powder. Laue patterns from their two surfaces are presented in figure A1. The absence of the reflexes splitting, i.e. the mosaic structure, indicates the high quality of the single crystal. The lattice constant from the crushed single crystal is equal to (4.156 ± 0.031) Å. The hydrostatic density is (4.708 ± 0.002) g cm^{-3}, which is less than the theoretical density 4.7118 g cm^{-3}. The formula composition of the crystal is $LaB_{5.985}$ or $La_{0.999}B_6$ in dependence on supposition of incompleteness of the boron or lanthanum sublattice respectively.

Abbreviations

(C)DBS	(Coincident) Doppler Broadening Spectroscopy
1D	One Dimensional
2D	Two Dimensional
3D	Three Dimensional
DBS	Doppler Broadening Spectroscopy
1D-ACAR	One-Dimensional Angular Correlation of Electron Positron Annihilation Radiation
2D-ACAR	Two-Dimensional Angular Correlation of Electron Positron Annihilation Radiation
ACAR	Angular Correlation of Electron Positron Annihilation Radiation
AMF	Around Mean-Field
ARPES	Angle Resolved Photoemission Spectroscopy
ART	Algebraic Reconstruction Technique
bcc	Body-Centered Cubic
BZ	Brillouin Zone
CCD	Charge-Coupled Device
CDBS	Coincident Doppler Broadening Spectroscopy
CM	Cormack's Method
CT	Computed Tomography
DFT	Density Functional Theory
dHvA	de-Haas-van-Alphen
DIM	Direct Inversion Method
DMFT	Dynamical Mean Field Theory

DOS	Density of States
DT	Direct Fourier Transformation
EMD	Electron Momentum Density
FBP	Filtered Back-Projection
fcc	Face-Centered Cubic
FEM	Finite Element Method
FLL	Fully Localized Limit
FS	Fermi Surface
FT	Fourier Transformation
GGA	General Gradient Approximation
HKS	Hohenberg-Kohn-Sham
IPM	Independent Particle Model
LCW	Lock-Crisp-West
LDA	Local Density Approximation
MSF	Momentum Sampling Function
NEPOMUC	Neutron Induced Positron Source Munich
o-Ps	Ortho-Positronium
p-Ps	Para-Positronium
PALS	Positron Annihilation Lifetime Spectroscopy
PAS	Positron Annihilation Spectroscopy
PLEPS	Pulsed Low-Energy Positron System
PMT	Photo Multiplier Tube
PSD	Position Sensitive detector
Ps	Positronium
SIC-LSDA	Self-Interaction-Corrected Local-Spin-Density Approximation
TPMD	Two-Photon Momentum Density
TUM	Technische Universität München

Own Publications

[KBD+21] Ketels, J., D. Billington, S. B. Dugdale, M. Leitner, and C. P. Hugenschmidt (2021): *Momentum density spectroscopy of Pd: Comparison of 2D-ACAR and Compton scattering using a 1D-to-2D reconstruction method*, Phys Rev B 104, 075160.

[KLB+21] Ketels, J., M. Leitner, P. Böni, C. Hugenschmidt, M. Sekania, A. D. N. James, J. A. E. Bonart, N. Unglert, and L. Chioncel (2021): *Fermi surface modeling of light-rare-earth hexaborides using positron annihilation spectroscopy*, physica status solidi (b) 259, 2100151.

Bibliography

[AAL97] Anisimov, V. I., F. Aryasetiawan, and A. I. Lichtenstein (1997): *First-principles calculations of the electronic structure and spectra of strongly correlated systems: The LDA +U method*, Journal of Physics: Condensed Matter 9(4), 767.

[AG98] Aryasetiawan, F. and O. Gunnarsson (1998): *The GW method*, Reports on Progress in Physics 61(3), 237.

[AM13] Ashcroft, N. W. and D. N. Mermin (2013): *Festkörperphysik*, Oldenbourg Verlag, 4th edn.

[And33] Anderson, C. D. (1933): *The positive electron*, Phys Rev 43, 491.

[Ang58] Anger, H. O. (1958): *Scintillation camera*, Review of Scientific Instruments 29(1), 27.

[BAD+97] Biasini, M., M. Alam, S. Dugdale, H. Fretwell, Y. Kubo, H. Harima, and N. Sato (1997): *Positron annihilation study of the electronic structure of LaB_6*, Applied Surface Science 116, 335, proceedings of the Seventh International Workshop on Slow-Positron Beam Techniques for Solids and Surfaces.

[BanN86] Boroński, E. and R. M. Nieminen (1986): *Electron-positron density-functional theory*, Phys Rev B 34, 3820.

[Bas15] Basunia, M. S. (2015): *Nuclear data sheets for A = 22*, Nuclear Data Sheets 127, 69.

[BEM+15] Billington, D., D. Ernsting, T. E. Millichamp, C. Lester, S. B. Dugdale, D. Kersh, J. A. Duffy, S. R. Giblin, J. W. Taylor, P. Manuel, D. D. Khalyavin, and H. Takatsu (2015): *Magnetic frustration, short-range correlations and the role of the*

paramagnetic Fermi surface of $PdCrO_2$, Scientific Reports 5, 12428.

[Ber62] Berko, S. (1962): *Band structure and positron annihilation in metals: Be and Mg*, Phys Rev 128, 2166.

[BF95] Bell, F. and J. Felsteiner (1995): *On the correction for multiple scattering of linearly polarized X-rays in Compton profile measurements*, Nuclear Instruments and Methods in Physics Research Section B: Beam Interactions with Materials and Atoms 101(4), 379 .

[BFD+97] Biasini, M., H. M. Fretwell, S. B. Dugdale, M. A. Alam, Y. Kubo, H. Harima, and N. Sato (1997): *Positron annihilation study of the electronic structure of LaB_6 and CeB_6*, Phys Rev B 56, 10192.

[BHM77] Berko, S., M. Haghgooie, and J. Mader (1977): *Momentum density measurements with a new multicounter two-dimensional angular correlation of annihilation radiation apparatus*, Physics Letters A 63(3), 335.

[BIS16] Brancewicz, M., M. Itou, and Y. Sakurai (2016): *A Monte Carlo study of high-energy photon transport in matter: Application for multiple scattering investigation in Compton spectroscopy*, Journal of Synchrotron Radiation 23(1), 244.

[BKMP72] Brown, C. R., J. P. Kalejs, F. D. Manchester, and J. M. Perz (1972): *Magnetoacoustic evidence for the existence of the L-centered pocket of Fermi surface in palladium*, Phys Rev B 6, 4458.

[Blo29] Bloch, F. (1929): *Über die Quantenmechanik der Elektronen in Kristallgittern*, Zeitschrift für Physik 52(7), 555.

[BM42] Beringer, R. and C. G. Montgomery (1942): *The angular distribution of positron annihilation radiation*, Phys Rev 61, 222.

[BM71] Berko, S. and A. P. Mills (1971): *Spin distribution studies in ferromagnetic metals by polarized positron annihilation experiments*, J Phys Colloques 32(C1), C1.

[BM75] Berko, S. and J. Mader (1975): *Momentum density measurements by positron annihilation in metals and alloys; recent experiments with a multicounter two-dimensional angular correlation apparatus*, Applied physics 5(4), 287.

[BMKS+01] Biasini, M., M. Monge, G. Kontrym-Sznajd, M. Gemmi, and N. Sato (2001): *Three-dimensional reconstruction of the Fermi surface of LaB_6*, in *Positron Annihilation - ICPA-12, Materials Science Forum*, vol. 363, Trans Tech Publications Ltd, pages 582–584.

[BMM75] Biggs, F., L. Mendelsohn, and J. Mann (1975): *Hartree-fock compton profiles for the elements*, Atomic Data and Nuclear Data Tables 16(3), 201 .

[BP58] Berko, S. and J. S. Plaskett (1958): *Correlation of annihilation radiation in oriented single metal crystals*, Phys Rev 112, 1877.

[BP77] Brandt, W. and R. Paulin (1977): *Positron implantation-profile effects in solids*, Phys Rev B 15, 2511.

[BPA+13] Brancewicz, M., M. Pylak, A. Andrejczuk, E. Żukowski, L. Dobrzyński, Y. Sakurai, M. Itou, and H. Sormann (2013): *Compton profile study and electron momentum density reconstruction in hexagonal Mg*, Journal of the Physical Society of Japan 82(7), 074702.

[BPK+74] Bergersen, B., E. Pajanne, P. Kubica, M. Stott, and C. Hodges (1974): *Positron diffusion in metals*, Solid State Communications 15(8), 1377.

[BPTN95] Barbiellini, B., M. J. Puska, T. Torsti, and R. M. Nieminen (1995): *Gradient correction for positron states in solids*, Phys Rev B 51, 7341.

[BW70] Berko, S. and M. Weger (1970): *Investigation of the Fermi surface of V_3Si by means of positron annihilation*, Phys Rev Lett 24, 55.

[CAI+04] Chen, C.-H., T. Aizawa, N. Iyi, A. Sato, and S. Otani (2004): *Structural refinement and thermal expansion of hexaborides*, Journal of Alloys and Compounds 366(1), L6.

[CDC+15] Chang, T.-R., T. Das, P.-J. Chen, M. Neupane, S.-Y. Xu, M. Z. Hasan, H. Lin, H.-T. Jeng, and A. Bansil (2015): *Two distinct topological phases in the mixed-valence compound YbB_6 and its differences from SmB_6*, Phys Rev B 91, 155151.

[CDK70] Crowther, R. A., D. J. DeRosier, and A. Klug (1970): *The reconstruction of a three-dimensional structure from projections and its application to electron microscopy*, Proceedings of the Royal Society of London A Mathematical and Physical Sciences 317(1530), 319.

[CdzS94] Czyżyk, M. T. and G. A. Sawatzky (1994): *Local-density functional and on-site correlations: The electronic structure of La_2CuO_4 and $LaCuO_3$*, Phys Rev B 49, 14211.

[CEB70] Cushner, S., J. C. Erskine, and S. Berko (1970): *Anisotropic positron annihilation with the high-momentum components of the conduction band in copper*, Phys Rev B 1, 2852.

[Cee15] Ceeh, H. (2015): *The new 2D-ACAR spectrometer for spin-resolved measurements of the electronic structure in correlated systems*, Dissertation, Technische Universität München, München.

[CFGT68] Chouteau, G., R. Fourneaux, K. Gobrecht, and R. Tournier (1968): *Specific heat and susceptibility enhancement in dilute Pd: Ni alloys*, Phys Rev Lett 20, 193.

[CFT63] Colombino, P., B. Fiscella, and L. Trossi (1963): *Point slits versus linear slits in the angular correlation of positron annihilation radiation*, Il Nuovo Cimento (1955-1965) 27(3), 589.

[CLC+82] Chou, M. Y., P. K. Lam, M. L. Cohen, G. Loupias, J. Chomilier, and J. Petiau (1982): *Compton profile of beryllium*, Phys Rev Lett 49, 1452.

[CLF85] Chomilier, J., G. Loupias, and J. Felsteiner (1985): *Correction for multiple scattering in Compton profile experiments: Application for synchrotron source photons*, Nuclear Instruments and Methods in Physics Research Section A: Accelerators, Spectrometers, Detectors and Associated Equipment 235(3), 603 .

[CLW65] Cooper, M., J. A. Leake, and R. J. Weiss (1965): *The Compton profile of lithium*, The Philosophical Magazine: A Journal of Theoretical Experimental and Applied Physics 12(118), 797.

[CMS+04] Cooper, M. J., P. E. Mijnarends, N. Shiotani, N. Sakai, and A. Bansil (2004): *X-ray Compton scattering*, no. 5 in Oxford Series on Synchrotron Radiation, Oxford University Press Inc.

[Com23] Compton, A. H. (1923): *A quantum theory of the scattering of X-rays by light elements*, Phys Rev 21, 483.

[Coo79] Cooper, M. J. (1979): *Gamma-ray source properties and Compton scattering*, Nuclear Instruments and Methods 166(1), 21.

[Coo85] Cooper, M. J. (1985): *Compton scattering and electron momentum determination*, Reports on Progress in Physics 48(4), 415.

[Cor63] Cormack, A. M. (1963): *Representation of a function by its line integrals, with some radiological applications*, Journal of Applied Physics 34(9), 2722.

[Cor64] Cormack, A. M. (1964): *Representation of a function by its line integrals, with some radiological applications. ii*, Journal of Applied Physics 35(10), 2908.

[CW73] Cracknell, A. and K. Wong (1973): *Fermi surface. Its concept, determination, and use in the physics of metals*, Clarendon Press, Oxford.

[CWB+16] Ceeh, H., J. A. Weber, P. Böni, M. Leitner, D. Benea, L. Chioncel, H. Ebert, J. Minár, D. Vollhardt, and C. Hugenschmidt (2016): *Local electron-electron interaction strength in ferromagnetic nickel determined by spin-polarized positron annihilation*, Scientific Reports 6, 20898.

[CWL+13] Ceeh, H., J. A. Weber, M. Leitner, P. Böni, and C. Hugenschmidt (2013): *The source-sample stage of the new two-dimensional angular correlation of annihilation radiation spectrometer at Technische Universität München*, Review of Scientific Instruments 84(4), 043905.

[Dam04] Damascelli, A. (2004): *Probing the electronic structure of complex systems by ARPES*, Physica Scripta 2004(T109), 61.

[DAV+11] Dashora, A., B. L. Ahuja, A. Vinesh, N. Lakshmi, M. Itou, and Y. Sakurai (2011): *Temperature and field dependent magnetic Compton scattering study of Heusler alloy Co_2MnSi*, Journal of Applied Physics 110(1), 013920.

[DCC+81] Dye, D. H., S. A. Campbell, G. W. Crabtree, J. B. Ketterson, N. B. Sandesara, and J. J. Vuillemin (1981): *Fermi surface and many-body enhancement in Pd*, Phys Rev B 23, 462.

[DCKP50] DeBenedetti, S., C. E. Cowan, W. R. Konneker, and H. Primakoff (1950): *On the angular distribution of two-photon annihilation radiation*, Phys Rev 77, 205.

[DDG+98] Dixon, M. A. G., J. A. Duffy, S. Gardelis, J. E. McCarthy, M. J. Cooper, S. B. Dugdale, T. Jarlborg, and D. N. Timms (1998): *Spin density in ferromagnetic nickel: A magnetic Compton scattering study*, Journal of Physics: Condensed Matter 10(12), 2759.

[DDM+00] Duffy, J. A., S. B. Dugdale, J. E. McCarthy, M. A. Alam, M. J. Cooper, S. B. Palmer, and T. Jarlborg (2000): *Induced spin polarization in ferromagnetic $Gd_{62.4}Y_{37.6}$*, Phys Rev B 61, 14331.

[DE66] Doniach, S. and S. Engelsberg (1966): *Low-temperature properties of nearly ferromagnetic Fermi liquids*, Phys Rev Lett 17, 750.

[DEK+20] Dickmann, M., W. Egger, G. Kögel, C. Hugenschmidt, and S. Vohburger (2020): *Upgrade of the NEPOMUC remoderator*, Acta physica Polonica/A 137, 149.

[DFA+97] Dugdale, S. B., H. M. Fretwell, M. A. Alam, G. Kontrym-Sznajd, R. N. West, and S. Badrzadeh (1997): *Direct observation and calipering of the "webbing" Fermi surface of yttrium*, Phys Rev Lett 79, 941.

[DFH+98] Dugdale, S. B., H. M. Fretwell, D. C. R. Hedley, M. A. Alam, T. Jarlborg, G. Santi, R. M. Singru, V. Sundararajan, and M. J. Cooper (1998): *Fermiology of Cr and Mo*, Journal of Physics: Condensed Matter 10(46), 10367.

[DFO+97] Degiorgi, L., E. Felder, H. R. Ott, J. L. Sarrao, and Z. Fisk (1997): *Low-temperature anomalies and ferromagnetism of EuB_6*, Phys Rev Lett 79, 5134.

[dGMEB83] de Groot, R. A., F. M. Mueller, P. G. v. Engen, and K. H. J. Buschow (1983): *New class of materials: Half-metallic ferromagnets*, Phys Rev Lett 50, 2024.

[Dir25] Dirac, P. A. M. (1925): *The effect of Compton scattering by free electrons in a stellar atmosphere*, Monthly Notices of the Royal Astronomical Society 85, 825.

[Dir28] Dirac, P. A. M. (1928): *The quantum theory of the electron*, Proceedings of the Royal Society of London Series A 117(778), 610.

[Dir31] Dirac, P. A. M. (1931): *Quantised singularities in the electromagnetic field*, Proceedings of the Royal Society of London Series A 133(821), 60.

[DIS+01] Deb, A., M. Itou, Y. Sakurai, N. Hiraoka, and N. Sakai (2001): *Magnetic Compton scattering study of the Co_2FeGa Heusler alloy: Experiment and theory*, Phys Rev B 63, 064409.

[DL14] Dugdale, S. B. and J. Laverock (2014): *Recovering the Fermi surface with 2D-ACAR spectroscopy in samples with defects*, Journal of Physics: Conference Series 505, 012046.

[DLRNP11] Drummond, N. D., P. López Ríos, R. J. Needs, and C. J. Pickard (2011): *Quantum Monte Carlo study of a positron in an electron gas*, Phys Rev Lett 107, 207402.

[DLRPN10] Drummond, N. D., P. López Ríos, C. J. Pickard, and R. J. Needs (2010): *First-principles method for impurities in quantum fluids: Positron in an electron gas*, Phys Rev B 82, 035107.

[DLW49] Dumond, J. W. M., D. A. Lind, and B. B. Watson (1949): *Precision measurement of the wave-length and spectral profile of the annihilation radiation from Cu^{64} with the two-meter focusing curved crystal spectrometer*, Phys Rev 75, 1226.

[DRK68] De Rosier, D. J. and A. Klug (1968): *Reconstruction of three dimensional structures from electron micrographs*, Nature 217(5124), 130.

[Dru00a] Drude, P. (1900): *Zur Elektronentheorie der Metalle*, Annalen der Physik 306(3), 566.

[Dru00b] Drude, P. (1900): *Zur Elektronentheorie der Metalle; II. Teil. Galvanomagnetische und thermomagnetische Effecte*, Annalen der Physik 308(11), 369.

[DS67a] Donaghy, J. J. and A. T. Stewart (1967): *"Enhancement factor" for positrons in sodium*, Phys Rev 164, 396.

[DS67b] Donaghy, J. J. and A. T. Stewart (1967): *Fermi surface of lithium by positron annihilation*, Phys Rev 164, 391.

[DS06] Dryzek, J. and D. Singleton (2006): *Implantation profile and linear absorption coefficients for positrons injected in solids from radioactive sources ^{22}Na and $^{68}Ge/^{64}Ge$*, Nuclear Instruments and Methods in Physics Research Section B: Beam Interactions with Materials and Atoms 252(2), 197.

[DSGC10] Dzero, M., K. Sun, V. Galitski, and P. Coleman (2010): *Topological Kondo insulators*, Phys Rev Lett 104, 106408.

[DSN+] Dewhurst, J. K., S. Sharma, L. Nordström, F. Cricchio, O. Granas, and E. K. U. Gross, *The Elk code*, http://elk.sourceforge.net/.

[Dug96] Dugdale, S. B. (1996): *A new approach to positron annihilation Fermiology: The electronic structure of chromium, yttrium and gadolinium.*, Ph.D. thesis, University of Bristol.

[Dug14] Dugdale, S. B. (2014): *Probing the Fermi surface by positron annihilation and Compton scattering*, Low Temperature Physics 40(4), 328.

[DuM29] DuMond, J. W. M. (1929): *Experimental and theoretical studies of the breadth and structure of the Compton shifted line*, Ph.D. thesis, California Institute of Technology.

[DXGC16] Dzero, M., J. Xia, V. Galitski, and P. Coleman (2016): *Topological Kondo insulators*, Annual Review of Condensed Matter Physics 7(1), 249.

[EBH+14] Ernsting, D., D. Billington, T. D. Haynes, T. E. Millichamp, J. W. Taylor, J. A. Duffy, S. R. Giblin, J. K. Dewhurst, and S. B. Dugdale (2014): *Calculating electron momentum densities and Compton profiles using the linear tetrahedron method*, Journal of Physics: Condensed Matter 26(49), 495501.

[Eis70] Eisenberger, P. (1970): *Electron momentum density of He and H_2; Compton X-ray scattering*, Phys Rev A 2, 1678.

[Eis72] Eisenberger, P. (1972): *Compton-profile measurements of N_2, O_2, and Ne using silver and molybdenum X-rays*, Phys Rev A 5, 628.

[EM66] Erskine, J. C. and J. D. McGervey (1966): *Electron momentum distribution in silicon and germanium by positron annihilation*, Phys Rev 151, 615.

[Erd53] Erdélyi, A. (ed.) (1953): *Bateman manuscript project - Higher Transcendental Functions*, McGraw-Hill Book Company, Inc.

[Fer34] Fermi, E. (1934): *Versuch einer theorie der β-strahlen. i*, Zeitschrift für Physik 88(3), 161.

[FHBS98] Fajardo, P., V. Honkimäki, T. Buslaps, and P. Suortti (1998): *Experimental validation of multiple scattering calculations with high energy x-ray photons*, Nuclear Instruments and Methods in Physics Research Section B: Beam Interactions with Materials and Atoms 134(3–4), 337 .

[FPC74] Felsteiner, J., P. Pattison, and M. Cooper (1974): *Effect of multiple scattering on experimental compton profiles: a monte carlo calculation*, Philosophical Magazine 30(3), 537.

[FPP+10] Fornalski, K. W., G. Parzych, M. Pylak, D. Satuła, and L. Dobrzyński (2010): *Application of Bayesian Reasoning and the Maximum Entropy Method to Some Reconstruction Problems*, Acta Physica Polonica A 117(6), 892.

[FS66] Fujiwara, K. and O. Sueoka (1966): *A precise measurement of the angular correlation of annihilation radiation in copper single crystals*, Journal of the Physical Society of Japan 21(10), 1947.

[FSBB79] Farmer, W., F. Sinclair, S. Berko, and G. Beardsley (1979): *Studies of the fermi surface of v3si by 2d acar measurements*, Solid State Communications 31(7), 481.

[GA95] Ghosh, V. J. and G. C. Aers (1995): *Positron stopping in elemental systems: Monte carlo calculations and scaling properties*, Phys Rev B 51, 45.

[GBH70] Gordon, R., R. Bender, and G. T. Herman (1970): *Algebraic reconstruction techniques (art) for three-dimensional electron microscopy and x-ray photography*, Journal of Theoretical Biology 29(3), 471 .

[GD78] Gull, S. F. and G. J. Daniell (1978): *Image reconstruction from incomplete and noisy data*, Nature 272(5655), 686.

[GMWP91] Genoud, P., A. A. Manuel, E. Walker, and M. Peter (1991): *Spin-polarized 2d ACAR in nickel across the curie temperature*, Journal of Physics: Condensed Matter 3(23), 4201.

[HC95] Hautojärvi, P. and C. Corbel (1995): *Positron spectroscopy of defects in metals and semiconductors*, in A. Dupasquier, A. M. j. (ed.), *Positron spectroscopy of solids*, Proceedings of the International School of Physics "Enrico Fermi", IOS press, pages 491–532.

[HCG+13] Hugenschmidt, C., H. Ceeh, T. Gigl, F. Lippert, C. Piochacz, P. Pikart, M. Reiner, J. Weber, and S. Zimnik (2013): *The upgrade of the neutron induced positron source NEPOMUC*, Journal of Physics: Conference Series 443, 012079.

[HCK+95] Hasegawa, M., T. Chiba, A. Kawasuso, T. Akahane, M. Suezawa, S. Yamaguchi, and K. Sumino (1995): *Positron-annihilation 2d-acar study of divacancy and vacancy-oxygen pairs in si*, in *Defects in Semiconductors 18*, *Materials Science Forum*, vol. 196, Trans Tech Publications Ltd, pages 1481–1490.

[Hed65] Hedin, L. (1965): *New method for calculating the one-particle green's function with application to the electron-gas problem*, Phys Rev 139, A796.

[HIO+01] Hiraoka, N., M. Itou, T. Ohata, M. Mizumaki, Y. Sakurai, and N. Sakai (2001): *A new X-ray spectrometer for high-resolution Compton profile measurements at SPring-8*, Journal of Synchrotron Radiation 8(1), 26.

[HJ20] Hung, S.-H. and H.-T. Jeng (2020): *Topological phase and strong correlation in rare-earth hexaborides xb6 (x = la, ce, pr, nd, pm, sm, eu)*, Materials 13(19).

[HK64] Hohenberg, P. and W. Kohn (1964): *Inhomogeneous electron gas*, Phys Rev 136, B864.

[HKR+04] Hugenschmidt, C., G. Kögel, R. Repper, K. Schreckenbach, P. Sperr, B. Straßer, and W. Triftshäuser (2004): *The neutron induced positron source at munich – nepomuc*, Nuclear

Instruments and Methods in Physics Research Section B: Beam Interactions with Materials and Atoms 221, 160, proceedings of the XII International Workshop on Positron and Positronium Physics.

[HL76] Herman, G. T. and A. Lent (1976): *Iterative reconstruction algorithms*, Computers in Biology and Medicine 6(4), 273, advances in Picture Reconstruction—Theory and Applications.

[HLJD21] Harris-Lee, E. I., A. D. N. James, and S. B. Dugdale (2021): *Sensitivity of the fermi surface to the treatment of exchange and correlation*, Phys Rev B 103, 235144.

[HM86] Hanssen, K. E. H. M. and P. E. Mijnarends (1986): *Positron-annihilation study of the half-metallic ferromagnet nimnsb: Theory*, Phys Rev B 34, 5009.

[HMRB90] Hanssen, K. E. H. M., P. E. Mijnarends, L. P. L. M. Rabou, and K. H. J. Buschow (1990): *Positron-annihilation study of the half-metallic ferromagnet nimnsb: Experiment*, Phys Rev B 42, 1533.

[Hol88] Holm, P. (1988): *Relativistic compton cross section for general central-field hartree-fock wave functions*, Phys Rev A 37, 3706.

[HRW+81] Hsiang, T. Y., J. W. Reister, H. Weinstock, G. W. Crabtree, and J. J. Vuillemin (1981): *Magnetic field dependence of the electronic specific heat of palladium*, Phys Rev Lett 47, 523.

[Hug16] Hugenschmidt, C. (2016): *Positrons in surface physics*, Surface Science Reports 71(4), 547.

[HWB68] Hohenemser, C., J. Weingart, and S. Berko (1968): *Polarized positron annihilation in ferromagnetic gadolinium*, Physics Letters A 28(1), 41.

[HWL+12] Haynes, T. D., R. J. Watts, J. Laverock, Z. Major, M. A. Alam, J. W. Taylor, J. A. Duffy, and S. B. Dugdale (2012): *Positron annihilation study of the fermi surface of ni2mnga*, New Journal of Physics 14(3), 035020.

[Jau25] Jauncey, G. E. M. (1925): *Quantum theory of the unmodified spectrum line in the compton effect*, Phys Rev 25, 314.

[JC84] Joss, W. and G. W. Crabtree (1984): *Anisotropy of the many-body enhancements on the fermi surface of pd*, Phys Rev B 30, 5646.

[JG89] Jones, R. O. and O. Gunnarsson (1989): *The density functional formalism, its applications and prospects*, Rev Mod Phys 61, 689.

[JHCV84] Joss, W., L. N. Hall, G. W. Crabtree, and J. J. Vuillemin (1984): *Absence of magnetic field dependence of the cyclotron effective masses of electrons on the fermi surface of pd*, Phys Rev B 30, 5637.

[JMP83] Jarlborg, T., A. A. Manuel, and M. Peter (1983): *Experimental and theoretical determination of the fermi surface of* v_3si, Phys Rev B 27, 4210.

[Jon15] Jones, R. O. (2015): *Density functional theory: Its origins, rise to prominence, and future*, Rev Mod Phys 87, 897.

[JR76] Jauch, J. and F. Rohrlich (1976): *The Theory of Photons and Electrons*, Springer.

[JS87] Jarlborg, T. and A. K. Singh (1987): *Local-density approach for calculation of electron-positron enhancement in transition metals*, Phys Rev B 36, 4660.

[JvRC+87] Joss, W., J. M. van Ruitenbeek, G. W. Crabtree, J. L. Tholence, A. P. J. van Deursen, and Z. Fisk (1987): *Observation of the magnetic field dependence of the cyclotron mass in the kondo lattice* ceb_6, Phys Rev Lett 59, 1609.

[JW90] Jensen, K. O. and A. Weiss (1990): *Theoretical study of the application of positron-induced auger-electron spectroscopy*, Phys Rev B 41, 3928.

[JW93] Jensen, K. O. and A. B. Walker (1993): *Monte carlo simulation of the transport of fast electrons and positrons in solids*, Surface Science 292(1), 83.

[Kah63] Kahana, S. (1963): *Positron annihilation in metals*, Phys Rev 129, 1622.

[KHK+16] Koitzsch, A., N. Heming, M. Knupfer, B. Büchner, P. Y. Portnichenko, A. V. Dukhnenko, N. Y. Shitsevalova, V. B. Filipov, L. L. Lev, V. N. Strocov, J. Ollivier, and D. S. Inosov (2016): *Nesting-driven multipolar order in ceb6 from photoemission tomography*, Nature communications 7, 10876.

[Kit96] Kittel, C. (1996): *Introduction to Solid State Physics*, John Wiley & Sons, Inc., 7th edn.

[KKN+91] Kubota, T., H. Kondo, H. Nakashima, Y. Murakami, and S. Tanigawa (1991): *Study on momentum density and fermi surface in paramagnetic cr and w by positron annihilation*, physica status solidi (b) 168(1), 179.

[KKN+92] Kondo, H., T. Kubota, H. Nakashima, T. Kawano, and S. Tanigawa (1992): *Spin-dependent three-dimensional electron momentum density studies in ferromagnetic co by means of full-scale use of a two-dimensional angular correlation of polarized positron annihilation radiation*, Journal of Physics: Condensed Matter 4(19), 4595.

[KKN+93] Kondo, H., T. Kubota, H. Nakashima, Y. Murakami, and S. Tanigawa (1993): *Study on the three-dimensional electron momentum density and the fermi surface in cu by positron annihilation*, physica status solidi (b) 177(2), 345.

[KNS+06] Koizumi, A., T. Nagao, N. Sakai, K. Hirota, and Y. Murakami (2006): *Coexistence of polaronic and band states in a bilayer manganite from two-dimensional reconstruction of magnetic compton profiles*, Phys Rev B 74, 012408.

[KO79] Krause, M. O. and J. H. Oliver (1979): *Natural widths of atomic K and L levels, Kα x-ray lines and several KLL Auger lines*, Journal of Physical and Chemical Reference Data 8(2), 329.

[Koh99] Kohn, W. (1999): *Nobel lecture: Electronic structure of matter—wave functions and density functionals*, Rev Mod Phys 71, 1253.

[Kok99] Kokalj, A. (1999): *XCrySDen—a new program for displaying crystalline structures and electron densities*, J Mol Graphics Mod 17(3), 176.

[Kon64] Kondo, J. (1964): *Resistance minimum in dilute magnetic alloys*, Progress of Theoretical Physics 32(1), 37.

[KR65] Konopinski, E. J. and M. E. Rose (1965): *The Theory of Nuclear β-DECAY*, in Siegbahn, K. (ed.), *Alpha-, Beta- and Gamma-ray Spectroscopy*, vol. 1, page 1327.

[KRBBvdW01] Krause-Rehberg, R., L. Büttner, F. Börner, and N. van der Walt (2001), *A ^{22}na source capsule for use in uhv.*

[Kru99] Kruseman, A. (1999): *Two-dimensional ACAR and low background DBAR studies on materials with defects*, Ph.D. thesis, Delft University of Technology.

[KS65] Kohn, W. and L. J. Sham (1965): *Self-consistent equations including exchange and correlation effects*, Phys Rev 140, A1133.

[KS90] Kontrym-Sznajd, G. (1990): *Three-dimensional image reconstruction with application in positron annihilation*, physica status solidi (a) 117(1), 227.

[KS09] Kontrym-Sznajd, G. (2009): *Fermiology via the electron momentum distribution (review article)*, Low Temperature Physics 35(8), 599.

[KSH+06] Kotliar, G., S. Y. Savrasov, K. Haule, V. S. Oudovenko, O. Parcollet, and C. A. Marianetti (2006): *Electronic structure calculations with dynamical mean-field theory*, Rev Mod Phys 78, 865.

[KSSC05] Kontrym-Sznajd, G. and M. Samsel-CzekaŁa (2005): *Different ways of dealing with compton scattering and positron annihilation experimental data*, Applied Physics A 80(8), 1693.

[KSSCP+02] Kontrym-Sznajd, G., M. Samsel-Czekała, A. Pietraszko, H. Sormann, S. Manninen, S. Huotari, K. Hämäläinen, J. Laukkanen, R. N. West, and W. Schülke (2002): *Electron momentum density in yttrium*, Phys Rev B 66, 155110.

[KV83] Kohn, W. and P. Vashishta (1983): *General density functional theory*, in Lundqvist, S. and N. H. March (eds.), *Theory of the Inhomogeneous Electron Gas*, Springer US, Boston, MA, pages 79–147.

[KV04] Kotliar, G. and D. Vollhardt (2004): *Strongly correlated materials: Insights from dynamical mean-field theory*, Physics Today 57(3), 53.

[LC00] Laricchia, G. and M. Charlton (2000): *Atomic and molecular phyics with positrons and positronium*, in Coleman, P. (ed.), *Positron Beams and Their Applications*, World Scientific Publishing Co. Pte. Ltd, pages 41–95.

[LCW73] Lock, D. G., V. H. C. Crisp, and R. N. West (1973): *Positron annihilation and fermi surface studies: a new approach*, Journal of Physics F: Metal Physics 3(3), 561.

[LCW12] Leitner, M., H. Ceeh, and J.-A. Weber (2012): *Eliminating spatial distortions in anger-type gamma cameras*, New Journal of Physics 14(12), 123014.

[LHAD10] Laverock, J., T. D. Haynes, M. A. Alam, and S. B. Dugdale (2010): *Experimental determination of the state-dependent enhancement of the electron-positron momentum density in solids*, Phys Rev B 82, 125127.

[LLGP79] Lässer, R., B. Lengeler, K. A. Gschneidner, and P. Palmer (1979): *Compton profiles of lutetium and lutetium dihydride*, Phys Rev B 20, 1390.

[LMS04] Larson, P., I. I. Mazin, and D. J. Singh (2004): *Magnetism, critical fluctuations, and susceptibility renormalization in pd*, Phys Rev B 69, 064429.

[LWC16] Leitner, M., J. A. Weber, and H. Ceeh (2016): *Fermi surface determination from momentum density projections*, New Journal of Physics 18(6), 063033.

[LY56] Lee, T. D. and C. N. Yang (1956): *Question of parity conservation in weak interactions*, Phys Rev 104, 254.

[Mac63] Mackintosh, A. R. (1963): *The Fermi Surface of Metals*, Scientific American 209(1), 110.

[Maj00] Major, J. (2000): *Spin-polarized positron beams in condensed-matter studies*, in Coleman, P. (ed.), *Positron Beams and Their Applications*, World Scientific Publishing Co. Pte. Ltd., pages 259–306.

[Mak61a] Makhov, A. (1961): *The penetration of electrons into solids. 1. the intensity of an electron beam, transverse paths of electrons*, Soviet Physics-Solid State 2(9), 1934.

[Mak61b] Makhov, A. (1961): *The penetration of electrons into solids. 2. the distribution of electrons in depth*, SOVIET PHYSICS-SOLID STATE 2(9), 1942.

[Mak61c] Makhov, A. (1961): *The penetration of electrons into solids. 3. the absorption of the energy of an electron beam*, Soviet Physics-Solid State 2(9), 1945.

[Man82] Manuel, A. A. (1982): *Construction of the fermi surface from positron-annihilation measurements*, Phys Rev Lett 49, 1525.

[MB71] Miiller, A. P. and B. N. Brockhouse (1971): *Crystal dynamics and electronic specific heats of palladium and copper*, Canadian Journal of Physics 49(6), 704.

[MDW+04] Major, Z., S. B. Dugdale, R. J. Watts, G. Santi, M. A. Alam, S. M. Hayden, J. A. Duffy, J. W. Taylor, T. Jarlborg, E. Bruno, D. Benea, and H. Ebert (2004): *Direct observation of the multisheet fermi surface in the strongly correlated transition metal compound* $zrzn_2$, Phys Rev Lett 92, 107003.

[MFDF70] Mueller, F. M., A. J. Freeman, J. O. Dimmock, and A. M. Furdyna (1970): *Electronic structure of palladium*, Phys Rev B 1, 4617.

[MFPJ78] Manuel, A., Ø. Fischer, M. Peter, and A. Jeavons (1978): *An application of proportional chambers to the measurement of the electronic properties of solids by positron annihilation*, Nuclear Instruments and Methods 156(1), 67.

[MH71] Mijnarends, P. E. and M. H. H. Höfelt (1971): *Positron annihilation in magnetized iron*, J Phys Colloques 32(C1), C1.

[MI11] Momma, K. and F. Izumi (2011): *VESTA3 for three-dimensional visualization of crystal, volumetric and morphology data*, Journal of Applied Crystallography 44(6), 1272.

[Mij67] Mijnarends, P. E. (1967): *Determination of anisotropic momentum distributions in positron annihilation*, Phys Rev 160, 512.

[Mij69] Mijnarends, P. E. (1969): *Determination of the fermi surface of copper by positron annihilation*, Phys Rev 178, 622.

[Moh34] Mohorovičić, S. (1934): *Möglichkeit neuer elemente und ihre bedeutung für die astrophysik*, Astronomische Nachrichten 253(4), 93.

[MOO+12] Mizusaki, S., T. Ohnishi, T. C. Ozawa, Y. Noro, M. Itou, Y. Sakurai, and Y. Nagata (2012): *Spin-polarized itinerant electrons in co-based heusler compounds investigated by magnetic compton scattering*, Journal of Applied Physics 111(6), 063915.

[MS79] Mijnarends, P. E. and R. M. Singru (1979): *Point-geometry angular correlation curves for cu: A study of enhancement in positron annihilation*, Phys Rev B 19, 6038.

[MSEG97] Major, J., A. Seeger, J. Ehmann, and T. Gessmann (1997): *Positronium in condensed matter studied with spin-polarized positrons*, in Jungmann, K. P., J. Kowalski, I. Reinhard, and

F. Träger (eds.), *Atomic Physics Methods in Modern Research*, Springer Berlin Heidelberg, Berlin, Heidelberg, pages 381–421.

[NAB+15] Neupane, M., N. Alidoust, I. Belopolski, G. Bian, S.-Y. Xu, D.-J. Kim, P. P. Shibayev, D. S. Sanchez, H. Zheng, T.-R. Chang, H.-T. Jeng, P. S. Riseborough, H. Lin, A. Bansil, T. Durakiewicz, Z. Fisk, and M. Z. Hasan (2015): *Fermi surface topology and hot spot distribution in the kondo lattice system* $\mathbf{ceb_6}$, Phys Rev B 92, 104420.

[NCT+01] Nagai, Y., T. Chiba, Z. Tang, T. Akahane, T. Kanai, M. Hasegawa, M. Takenaka, and E. Kuramoto (2001): *Fermi surface of nanocrystalline embedded particles in materials: bcc cu in fe*, Phys Rev Lett 87, 176402.

[Nie00] Nieminen, R. M. (2000): *The fate of slow positrons in condensed matter*, in Coleman, P. (ed.), *Positron Beams And Their Applications*, World Scientific Publishing Co. Pte. Ltd., pages 97–128.

[NKKT92] Nakashima, H., T. Kubota, H. Kondo, and S. Tanigawa (1992): *Study on momentum density of electrons and fermi surface in magnesium by positron annihilation*, physica status solidi (b) 170(2), 491.

[NNK+00] Nagai, Y., Y. Nagashima, J. Kim, Y. Itoh, and T. Hyodo (2000): *Measurement of positron spin polarization by using the doppler broadening method*, Nuclear Instruments and Methods in Physics Research Section B: Beam Interactions with Materials and Atoms 171(1), 199, low Energy Positron and Positronium Physics.

[OADM+16] Östlin, A., W. H. Appelt, I. Di Marco, W. Sun, M. Radonjić, M. Sekania, L. Vitos, O. Tjernberg, and L. Chioncel (2016): *Electronic structure of palladium in the presence of many-body effects*, Phys Rev B 93, 155152.

[Ons52] Onsager, L. (1952): *Interpretation of the de haas-van alphen effect*, The London, Edinburgh, and Dublin Philosophical Magazine and Journal of Science 43(344), 1006.

[Osw21] Oswald, C. (2021): *Temperature dependent 2D-ACAR spectroscopy of $Pr_2NiO_{4.25}$ and FEM modelling of temperature in a 2D-ACAR setup*, Bachelor thesis, Technische Universität München.

[PBE96] Perdew, J. P., K. Burke, and M. Ernzerhof (1996): *Generalized gradient approximation made simple*, Phys Rev Lett 77, 3865.

[PBL09] Park, J., S. C. Byun, and B. U. Lee (2009): *Lens distortion correction using ideal image coordinates*, IEEE Transactions on Consumer Electronics 55(3), 987.

[PDKS11] Pylak, M., L. Dobrzyński, and G. Kontrym-Sznajd (2011): *Reconstruction of momentum density distribution from 2d acar data via maximum entropy and cormack methods*, in *Progress in Positron Annihilation*, *Materials Science Forum*, vol. 666, Trans Tech Publications Ltd, pages 151–154.

[PH57] Page, L. A. and M. Heinberg (1957): *Measurement of the longitudinal polarization of positrons emitted by sodium-22*, Phys Rev 106, 1220.

[PKE+08] Piochacz, C., G. Kögel, W. Egger, C. Hugenschmidt, J. Mayer, K. Schreckenbach, P. Sperr, M. Stadlbauer, and G. Dollinger (2008): *A positron remoderator for the high intensity positron source nepomuc*, Applied Surface Science 255(1), 98, proceedings of the Eleventh International Workshop on Slow Positron Beam Techniques for Solids and Surfaces.

[PKSD11] Pylak, M., G. Kontrym-Sznajd, and L. Dobrzyński (2011): *Electron-positron momentum density distribution of gd from 2d acar data via maximum entropy and cormack's methods*, Applied Physics A 104(2), 587.

[PMCL03] Petukhov, A. G., I. I. Mazin, L. Chioncel, and A. I. Lichtenstein (2003): *Correlated metals and the* LDA + u *method*, Phys Rev B 67, 153106.

[PN94] Puska, M. J. and R. M. Nieminen (1994): *Theory of positrons in solids and on solid surfaces*, Rev Mod Phys 66, 841.

[PW92] Perdew, J. P. and Y. Wang (1992): *Accurate and simple analytic representation of the electron-gas correlation energy*, Phys Rev B 45, 13244.

[PZ81] Perdew, J. P. and A. Zunger (1981): *Self-interaction correction to density-functional approximations for many-electron systems*, Phys Rev B 23, 5048.

[Rad17] Radon, J. (1917): *Über die Bestimmung von Funktionen durch ihre Integralwerte längs gewisser Mannigfaltigkeiten*, Berichte über die Verhandlungen der Königlich Sächsischen Gesellschaft der Wissenschaften zu Leipzig 69, 262.

[RB05] Rusz, J. and M. Biasini (2005): *Nature of f-electrons in* $\mathrm{Cein_3}$*: Theoretical analysis of positron annihilation data*, Phys Rev B 71, 233103.

[RE72] Reed, W. A. and P. Eisenberger (1972): *Gamma-ray compton profiles of diamond, silicon, and germanium*, Phys Rev B 6, 4596.

[Ris00] Riseborough, P. S. (2000): *Heavy fermion semiconductors*, Advances in Physics 49(3), 257.

[RJ12] Rourke, P. and S. Julian (2012): *Numerical extraction of de haas–van alphen frequencies from calculated band energies*, Computer Physics Communications 183(2), 324.

[RL71] Ramachandran, G. N. and A. V. Lakshminarayanan (1971): *Three-dimensional reconstruction from radiographs and electron micrographs: Application of convolutions instead of fourier transforms*, Proceedings of the National Academy of Sciences 68(9), 2236.

[RLG+93] Ritley, K. A., K. G. Lynn, V. J. Ghosh, D. O. Welch, and M. McKeown (1993): *Low-energy contributions to positron implantation*, Journal of Applied Physics 74(5), 3479.

[RML+20] Robarts, H. C., T. E. Millichamp, D. A. Lagos, J. Laverock, D. Billington, J. A. Duffy, D. O'Neill, S. R. Giblin, J. W. Taylor,

G. Kontrym-Sznajd, M. Samsel-Czekała, H. Bei, S. Mu, G. D. Samolyuk, G. M. Stocks, and S. B. Dugdale (2020): *Extreme fermi surface smearing in a maximally disordered concentrated solid solution*, Phys Rev Lett 124, 046402.

[Rua45] Ruark, A. E. (1945): *Positronium*, Phys Rev 68, 278.

[Rub08] Rubaszek, A. (2008): *The effect of the positron distribution and electron–positron correlations on the electron–positron momentum density for SiC*, Journal of Physics: Condensed Matter 20(33), 335226.

[Sak98] Sakurai, Y. (1998): *High-Energy Inelastic-Scattering Beamline for Electron Momentum Density Study*, Journal of Synchrotron Radiation 5(3), 208.

[SE68] Stroud, D. and H. Ehrenreich (1968): *Assumption-independent single-particle wave functions for positrons in solids: Applications to angular distributions in al and si*, Phys Rev 171, 399.

[Sho84] Short, M. (1984): *Gamma-camera systems*, Nuclear Instruments and Methods in Physics Research 221(1), 142, proceedings of the International Workshop on X- and γ-Ray Imaging Techniques.

[SI04] Sakurai, Y. and M. Itou (2004): *A cauchois-type x-ray spectrometer for momentum density studies on heavy-element materials*, Journal of Physics and Chemistry of Solids 65(12), 2061 , sagamore XIV: Charge, Spin and Momentum Densities.

[SIB+11] Sakurai, Y., M. Itou, B. Barbiellini, P. E. Mijnarends, R. S. Markiewicz, S. Kaprzyk, J.-M. Gillet, S. Wakimoto, M. Fujita, S. Basak, Y. J. Wang, W. Al-Sawai, H. Lin, A. Bansil, and K. Yamada (2011): *Imaging doped holes in a cuprate superconductor with high-resolution compton scattering*, Science 332(6030), 698.

[SK91] Sterne, P. A. and J. H. Kaiser (1991): *First-principles calculation of positron lifetimes in solids*, Phys Rev B 43, 13892.

[SL74] Shepp, L. A. and B. F. Logan (1974): *The fourier reconstruction of a head section*, IEEE Transactions on Nuclear Science 21(3), 21.

[SL88] Schultz, P. J. and K. G. Lynn (1988): *Interaction of positron beams with surfaces, thin films, and interfaces*, Reviews of Modern Physics 60(3), 701.

[SLB+88] Smedskjaer, L., J. Liu, R. Benedek, D. Legnini, D. Lam, M. Stahulak, H. Claus, and A. Bansil (1988): *The fermi surface in yba2cu3o7-x by 2d acar*, Physica C: Superconductivity 156(2), 269 .

[SM74] Singru, R. M. and P. E. Mijnarends (1974): *Calculation of the momentum density in ferromagnetic nickel*, Phys Rev B 9, 2372.

[SMW88] Singh, A. K., A. A. Manuel, and E. Walker (1988): *Differences in the fermi surface topology of paramagnetic and antiferromagnetic cr studied by positron annihilation*, Europhysics Letters (EPL) 6(1), 67.

[Som28] Sommerfeld, A. (1928): *Zur elektronentheorie der metalle auf grund der fermischen statistik*, Zeitschrift für Physik 47(1), 1.

[SOT+89] Suzuki, R., M. Osawa, S. Tanigawa, M. Matsumoto, and N. Shiotani (1989): *Positron study of electron momentum density and fermi surface in titanium and zirconium*, Journal of the Physical Society of Japan 58(9), 3251.

[TAG+09] Thompson, A., D. Attwood, E. Gullikson, M. Howells, K. J. Kim, J. Kirz, J. Kortright, I. Lindau, Y. Liu, P. Pianetta, A. Robinson, J. Scofield, J. Underwood, G. Williams, and H. Winick (2009): *X-ray data booklet*, Center for X-Ray Optics and Advanced Light Source, Lawrence Berkeley National Laboratory University of California Berkeley, CA 94720.

[TE74] Tanner, A. C. and I. R. Epstein (1974): *Compton profile and electron momentum distribution of water*, The Journal of Chemical Physics 61(10), 4251.

[Tho97] Thomson, J. J. (1897): *XL. Cathode rays*, The London, Edinburgh, and Dublin Philosophical Magazine and Journal of Science 44(269), 293.

[THZ+15] Tan, B. S., Y.-T. Hsu, B. Zeng, M. C. Hatnean, N. Harrison, Z. Zhu, M. Hartstein, M. Kiourlappou, A. Srivastava, M. D. Johannes, T. P. Murphy, J.-H. Park, L. Balicas, G. G. Lonzarich, G. Balakrishnan, and S. E. Sebastian (2015): *Unconventional fermi surface in an insulating state*, Science 349(6245), 287.

[Tik63] Tikhonov, A. N. (1963): *Solution of incorrectly formulated problems and the regularization method*, Soviet Math Dokl 4, 1035.

[TŌ02] Tanaka, K. and Y. Ōnuki (2002): *Observation of* $4f$ *electron transfer from Ce to* B_6 *in the Kondo crystal* CeB_6 *and its mechanism by multi-temperature X-ray diffraction*, Acta Crystallographica Section B 58(3 Part 2), 423.

[TSS+01] Tanaka, Y., Y. Sakurai, A. T. Stewart, N. Shiotani, P. E. Mijnarends, S. Kaprzyk, and A. Bansil (2001): *Reconstructed three-dimensional electron momentum density in lithium: A compton scattering study*, Phys Rev B 63, 045120.

[VHG99] Vuillemin, J. J., N. Harrison, and R. G. Goodrich (1999): *High-field de haas–van alphen measurements in pd*, Phys Rev B 59, 12177.

[VN83] Valkealahti, S. and R. M. Nieminen (1983): *Monte-carlo calculations of kev electron and positron slowing down in solids*, Applied Physics A 32(2), 95.

[VN84] Valkealahti, S. and R. M. Nieminen (1984): *Monte carlo calculations of kev electron and positron slowing down in solids. ii*, Applied Physics A 35(1), 51.

[VP65] Vuillemin, J. J. and M. G. Priestley (1965): *De haas-van alphen effect and fermi surface in palladium*, Phys Rev Lett 14, 307.

[VPDVH+04] Van Petegem, S., C. Dauwe, T. Van Hoecke, J. De Baerdemaeker, and D. Segers (2004): *Diffusion length of positrons*

and positronium investigated using a positron beam with longitudinal geometry, Phys Rev B 70, 115410.

[WBA+17] Weber, J. A., D. Benea, W. H. Appelt, H. Ceeh, W. Kreuzpaintner, M. Leitner, D. Vollhardt, C. Hugenschmidt, and L. Chioncel (2017): *Electronic correlations in vanadium revealed by electron-positron annihilation measurements*, Phys Rev B 95, 075119.

[WBB+15] Weber, J. A., A. Bauer, P. Böni, H. Ceeh, S. B. Dugdale, D. Ernsting, W. Kreuzpaintner, M. Leitner, C. Pfleiderer, and C. Hugenschmidt (2015): *Spin-resolved fermi surface of the localized ferromagnetic heusler compound* cu_2MnAl *measured with spin-polarized positron annihilation*, Phys Rev Lett 115, 206404.

[Web17] Weber, J. A. (2017): *Spin-Polarized Positron Annihilation Spectroscopy*, Dissertation, Technische Universität München, München.

[WM68] Williams, R. W. and A. R. Mackintosh (1968): *Electronic structure of rare-earth metals. ii. positron annihilation*, Phys Rev 168, 679.

[WMW81] West, R. N., J. Mayers, and P. A. Walters (1981): *A high-efficiency two-dimensional angular correlation spectrometer for positron studies*, Journal of Physics E: Scientific Instruments 14(4), 478.

[WR52] Wolfenstein, L. and D. G. Ravenhall (1952): *Some consequences of invariance under charge conjugation*, Phys Rev 88, 279.

[WSK+94] Willutzki, P., J. Stormer, G. Kogel, P. Sperr, D. T. Britton, R. Steindl, and W. Triftshauser (1994): *An improved pulsed low-energy positron system*, Measurement Science and Technology 5(5), 548.

[Yan50] Yang, C. N. (1950): *Selection rules for the dematerialization of a particle into two photons*, Phys Rev 77, 242.

[Zer34] Zernike, F. (1934): *Beugungstheorie des schneidenverfahrens und seiner verbesserten form, der phasenkontrastmethode*, Physica 1(7), 689.

Acknowledgments

Finishing a work like this without the support of many people would not be possible. This is the place to say "Thank you!" to everybody who contributed to the journey of this project.

Als erstes möchte ich mich bei Herrn Prof. Dr. Christoph Hugenschmidt bedanken. Christoph, vielen Dank für das Anvertrauen dieses Projekts, deine große Begeisterung für die Experimentalphysik und deine jederzeit offene Tür. Es war mir eine große Freude, in deiner Gruppe zu promovieren.

Prof. Dr. Brandt und Prof. Dr. Kaiser, vielen Dank, dass Sie sich für die Prüfungskommision zur Verfügung stellen.

I would like to thank Prof. Dr. Stephen Dugdale and Dr. David Billington for the collaboration within the Pd project. You both helped me to find my path in the field of Compton scattering. David, thank you for all the great time at SPring-8.

Prof. Dr. Peter Böni, Prof. Dr. Liviu Chioncel und Dr. Mikheil Sekania möchte ich für die Zusammenarbeit im Rahmen des LaB_6 und des Transregios TRR60 danken. Vielen Dank auch für die vielen Einblicke in die theoretische Modellierung, die ihr mir bei vielen Transregio-Zusammenkünften gegeben habt.

Ganz besonders möchte ich allen danken die ein Büro mit mir geteilt haben: Dr. Michael Leitner, Dr. Hubert Ceeh, Dr. Pascal Neibecker, Dr. Josef Weber, Dr. Ulrike Zweck und Sebastian Vohburger. Michael, ohne deine ständige Unterstützung in allen Themen der Mathematik und Programmierung und die unzähligen Diskussionen über die Physik wäre diese Arbeit nicht im Ansatz möglich gewesen. Josef und Hubert, ihr habt mir nicht nur das ACAR-Spektrometer überlassen, sondern seid auch nach eure Zeit in der NEPOMUC Gruppe immer für Fragen rund ums Experiment zur Verfügung gestanden. Pascal, ohne dich wäre ich vielleicht nie in Berührung mit der NEPOMUC Gruppe gekommen. Danke, dass du mich damals als Werkstudenten angeworben hast. Uli, vielen Dank für das gemeinsame Durchstehen, Schimpfen, Lachen,

Diskutieren in den letzten Jahren. Sebastian, auf dich ist einfach Verlass. Besten Dank für die stete Unterstützung bei allen technischen Umbauten, Aufbauten oder sonstigen Fragestellungen rund ums Experiment.

Außerdem möchte ich allen anderen Mitgliedern der NEPOMUC Gruppe danken. Vassily Burwitz, Leon Chryssos, Dr. Marcel Dickmann, Matthias Dodenhöft, Dr. Thomas Gigl, Dr. Francesco Guatieri, Lucian Mathes, Dr. Markus Singer, Dr. Samantha Zimnik, ich konnte mit euch nicht nur über die kleinen und großen wissenschaftlichen Probleme diskutieren, sondern auch bei der einen oder der anderen Laborbesprechung, Wanderung oder Grillabend lustige, spannende oder ernste Gespräche außerhalb der Wissenschaft führen. Danke für die super Arbeitsatmosphäre. Nicht vergessen möchte ich meine beiden Bacheloranden Martin Großhauser und Christoph Oswald.

Außerdem möchte ich mich beim Kristalllabor und den Werkstätten des FRMII und Physikdepartments für die stets unkomplizierten Unterstützung bedanken.

Ohne die lebenslange Unterstützung meiner Familie, insbesondere meiner Eltern, wäre dieser Weg nicht möglich gewesen. Alleine das Ermöglichen eines Physikstudiums nach einem abgeschlossenen Mechatronikstudiums ist alles andere als selbstverständlich. Auch wenn ihr euch oft gewundert habt, was ich da an der Uni so treibe, habe ich immer euer tiefes Vertrauen und Unterstützung gespürt. Von Herzen, Danke!

Ganz besonders danken möchte ich meiner Frau Marthe. Danke für deine Unterstützung, Geduld und Liebe. Danke für Alles.